Multi-Epoch VLBI Observations of TANAMI Jets

Masterarbeit

Jonas Trüstedt

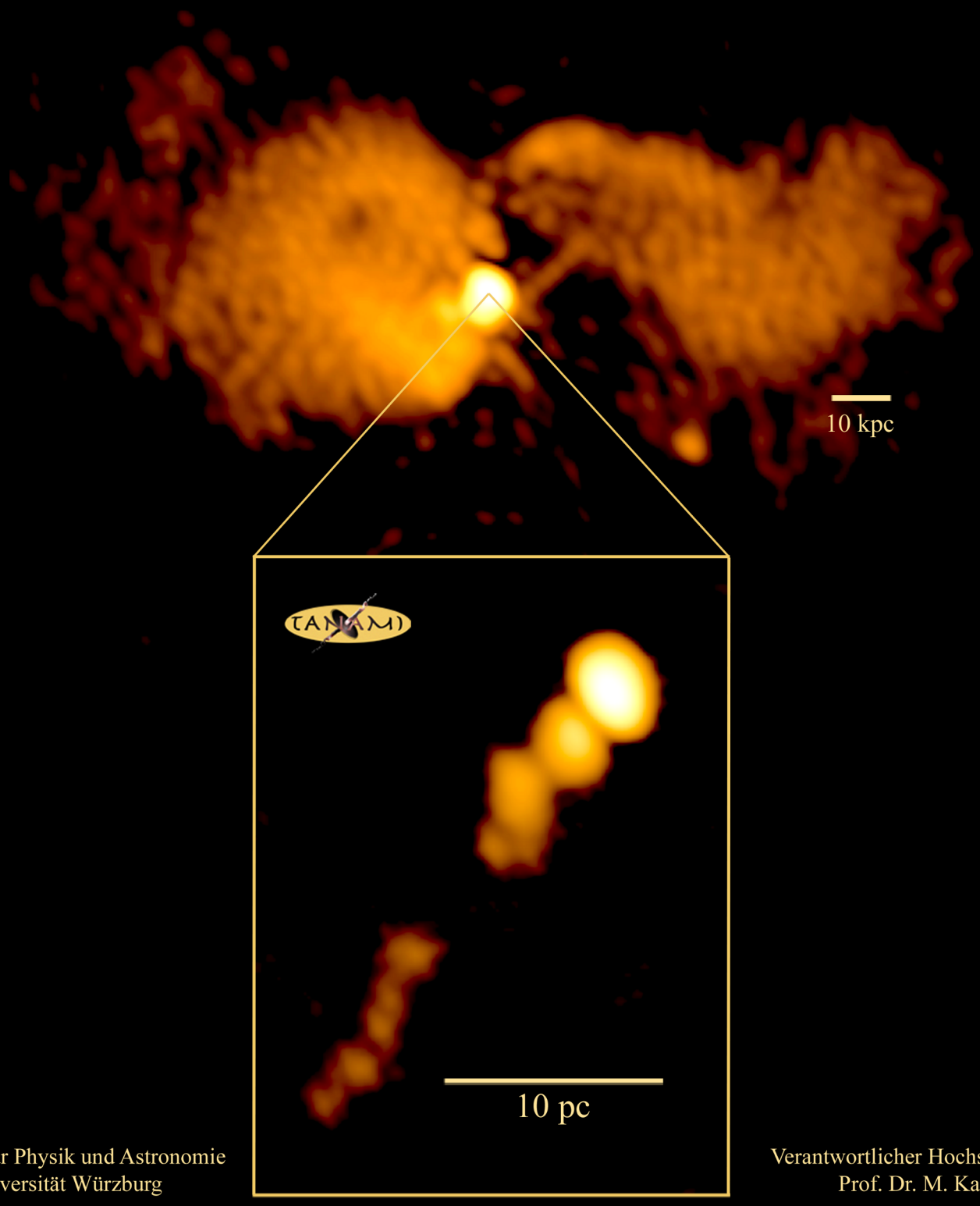

Fakultät für Physik und Astronomie
Universität Würzburg

Verantwortlicher Hochschullehrer:
Prof. Dr. M. Kadler

The title page shows a composite of the brightness distribution of PKS 0625-35, observed at kpc-scales with the VLA (archival data of the observation at 4.86 GHz in June 23 1985, provided by T. Cheung) and the zoom-in of the pc-scale central region image observed by TANAMI at 8.4 GHz in November 27 2008 presented in this master thesis

Multi-Epoch VLBI Observations of TANAMI Jets

Masterarbeit am Lehrstuhl für Astronomie
von
Jonas Elias Trüstedt

Fakultät für Physik und Astronomie
Julius-Maximilians-Universität Würzburg

Würzburg, den 28. März 2013

Verantwortlicher Hochschullehrer: Prof. Dr. M. Kadler

Zusammenfassung

Das TANAMI-Projekt beobachtet von der Südhalbkugel aus regelmäßig aktive Galaxienkerne (AGN), welche mithilfe von Radioteleskopen, die über *Very Long Baseline Interferometry* (VLBI) Technik miteinander verbunden werden, untersucht werden können. Die VLBI-Technik ermöglicht es dabei hochauflösende Bilder der Helligkeitsverteilung der Strahlung im Radiowellenbereich herzustellen. In dieser Masterarbeit werden die Ergebnisse von acht Quellen über mehrere Beobachtungsepochen vorgestellt.
Aktive Galaxienkerne besitzen Jets, die senkrecht zu ihrer Galaxienscheibe verlaufen. Jets bestehen aus Plasmaströmen geladener Teilchen, welche Synchrotronstrahlung emittieren und scheinbare Überlichtgeschwindigkeit erreichen können. Diese Jets sind im ganzen elektromagnetischen Spektrum sichtbar und können mit Hilfe von VLBI auf Parsec-Skala oder genauer aufgelöst werden.
Alle hier untersuchten Objekte wurden in den Jahren 2007 bis 2011 im X-Band (8.4 GHz) sechsmal und im K-Band (22.3 GHz) zwei- bis dreimal beobachtet. Durch die Karten der Helligkeitsverteilung und die Fits mit kreisförmigen Gaußschen Modellkomponenten konnten erstmals im Rahmen des TANAMI Projektes konsistente Modelle gebildet werden, welche die Analyse der zeitlichen Entwicklung der Flussdichten, der Helligkeitstemperaturen und der Leuchtkräfte ermöglichen.
Für sechs der Jets konnte erstmals auch die Kinematik untersucht werden. Dabei wurden für zwei Quellen Komponenten gefunden, die scheinbare Geschwindigkeiten größer als die Lichtgeschwindigkeit besitzen.
Durch Beobachtungen bei zwei Frequenzen war es möglich, den Spektralindex der Quellen zu untersuchen und eine Karte mit der Spektralindexverteilung zu erstellen. Dadurch konnte der Spektralindex des Kerns mit zwei unterschiedlichen Methoden bestimmt werden, wobei beide Vorgehensweisen konsistente Ergebnisse liefern.

Abstract

The TANAMI project monitors a sample of active galactic nuclei (AGN) with radio telescopes in the Southern Hemisphere using the Very Long Baseline Interferometry (VLBI) technique. These VLBI observations provide high resolution images of the brightness distribution of radio emission. This thesis presents the results of the multi-epoch observations of acht sources of the TANAMI project.
Active galactic nuclei have jets perpendicular to their host galaxy, which can be seen over the whole electromagnetic spectrum. These jets can be studied on parsec- or even subparsec-scale in the radio wavelength regime using VLBI. The jets are streams of charged particles emitting Synchrotron radiation and often show apparent superluminal velocities of their jet components.
Each source studied in this work has been observed over six epochs in the X-band (8.4 GHz) and two or three in the K-band (22.3 GHz) in the time range between 2007 and 2011. The brightness distribution maps and the fitting of circular Gaussian model components build consistent models for each object and allowed to analyse the temporal evolution of the flux densities, the brightness temperature and the luminosities for the first time in the TANAMI project.
Six jets also made kinematic studies possible for the first time. Two sources have components of excellent quality with apparent superluminal velocities.
With the dual-frequency observations it was possible to study the spectral index of the sources. For each dual-frequency observation a spectral index map was built and the spectral index of the core was measured with two different methods, giving consistent results.

Contents

Acknowledgements

This research has made use of the NASA/IPAC Extragalactic Database (NED) which is operated by the Jet Propulsion Laboratory, California Institute of Technology, under contract with the National Aeronautics and Space Administration.
This research has made use of NASA's Astrophysics Data System.
This research has made use of the data from the ATCA project C1730 (PI: *P. Edwards*) from the CSIRO Astronomy and Space Science.

1. Introduction

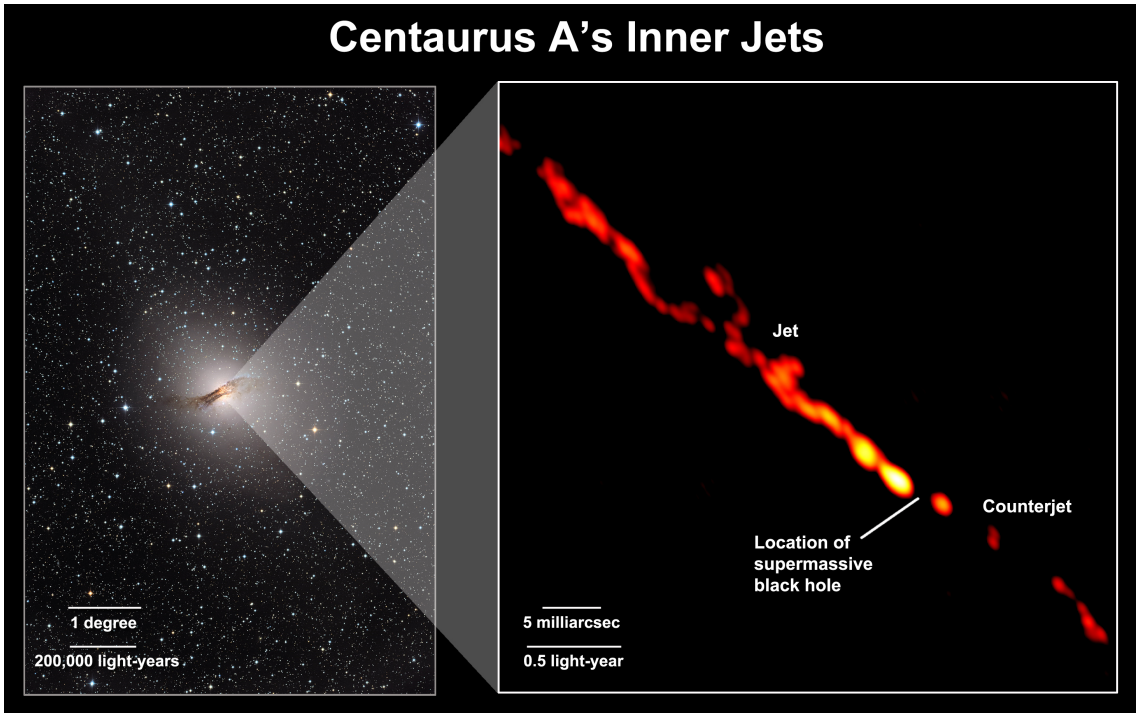

Figure 1.1.: NGC 5128 also known as Centaurus A in the optical wavelengths (on the left) with the high resolution image in the radio band of the sub-parsec scale jet near the black hole (on the right) by TANAMI/Mueller et al. (2011).

The Universe is a field of research with many different topics. From theoretical concepts of the origin to the understanding of new observations and predictions regarding the evolution of certain features, it offers a spectrum of possible studies. This thesis is about the observations of certain galaxies with an Active Galactic Nucleus (AGN). These objects are visible in the whole electro-magnetic spectrum from the radio wavelengths up to the γ-ray regime. Therefore different instruments are required to study these objects in their features in different wavelength bands. The data used in this work are from observations of the TANAMI project using a network of radio telescopes in the Southern Hemisphere.
One famous AGN of the TANAMI sample is Centaurus A, because the images achieved one of the best resolutions of the sub-parsec-scale jets seen until now in Fig. 1.1 (Mueller

et al. 2011; Mueller 2011). Centaurus A is the closest AGN to Earth and is classified as a Fanaroff-Riley type I galaxy. But there exist also other types of AGN, which can be observed at much higher distances due to their high luminosities. To understand the meaning of the different classifications the next chapter will introduce the different types and features of AGN, followed by the theoretical concepts. After these parts the data analysis of radio images will be explained in order to present the results of this work with other sources of the TANAMI sample.

2. Active Galactic Nuclei - AGN

The following chapter gives an overview of the nature of an *Active Galactic Nucleus* (AGN). The term AGN refers to the central region of an active galaxy. This region has higher luminosities than typical galaxies or its own host galaxy. Therefore some interesting features can be found there. If no additional references are given, the main information was taken from textbooks by Schneider (2008) and Krolik (1999).

2.1. Properties of AGN

The inner region of an active galaxy emits powerful emission across the electromagnetic spectrum and is the origin for the galaxy's state of being active, while emission of ordinary galaxies is dominated by thermal radiation. AGN's luminosities have their origin in the core of the galaxy and are about 10^3 times greater than the radiation of ordinary galaxies.
There are many instruments to observe AGN: for example the *Fermi Gamma-ray Space Telescope* (Atwood et al. 2009) in the γ-rays, *Chandra* (Weisskopf et al. 2002), *Swift* (Burrows et al. 2005) and *XMM-Newton* (Jansen et al. 2001) in the X-rays, *HST* (Williams et al. 1996) in the optical and *VLBI* networks in the radio regime.
AGN are commonly assumed to have a typical structure: a super massive black hole (SMBH) in the center gains energy through accretion of matter from the accretion disk around it. The accretion disk is surrounded by a torus of dust. In some types of AGN exist jets perpendicular to the accretion disk in both directions ending in big lobes (see Fig. 2.1).
The Unification Model (Antonucci 1993; Urry & Padovani 1995) merges the different types of AGN classified after observation properties in one model with dependency on the angle of the line of sight (see Sect. 2.3).

2.1.1. The Central Engine

Concerning the emission of AGN at all wavelengths the origin of this energy is very interesting. The observed properties and generally accepted theories explain the observations with a super massive black hole (SMBH) with mass of 10^6 - 10^9 $M_\odot$ (Peterson 1997). Some arguments for a SMBH will be described shortly:
With the assumption that the observed luminosities remain constant over the lifetime of the source the total produced energy can be estimated from the luminosity and the

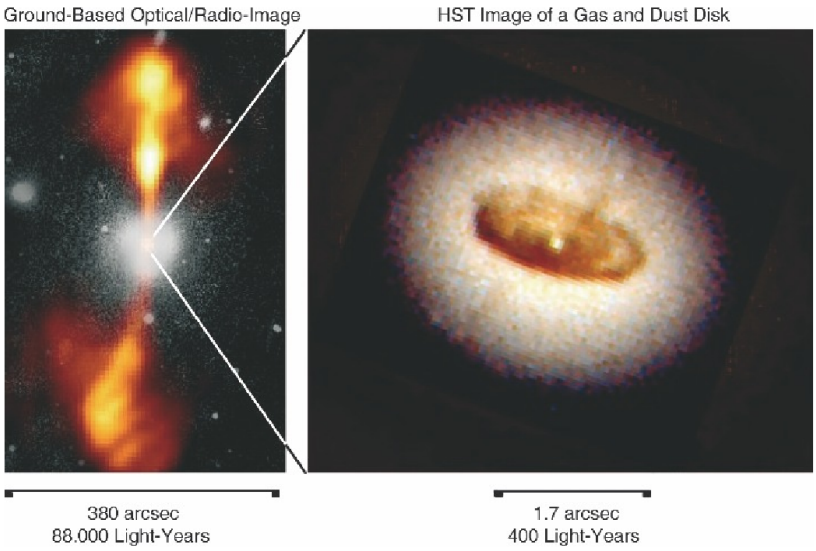

Figure 2.1.: NGC4261 in the left an image of optical wavelengths with an overlay of radio radiation in orange (left) and central region observed in the optical with HST (right) (Schneider 2008)

minimum age to E $\sim 3 \times 10^{61}$ erg. Considering thermonuclear processes and a maximal efficiency the burnt-out matter would have a Schwarzschild-Radius of $r_S \sim 6 \times 10^{14}$ cm, which has the same magnitude of the estimated radius of the whole central source. Therefore gravitational processes have to be the origin of this energy and a central black hole with accretion is a solution (Shakura & Sunyaev 1973).
For an object with mass M, which is in equilibrium with in-falling matter and the radiation pressure, the so called *Eddington-limit* gives an upper limit on its luminosity: $L < L_{Edd} = 1.3 \times 10^{38} \frac{M}{M_\odot}$ erg s^{-1}. With a luminosity of 10^{46} erg s^{-1} for the central source, the limit of the mass is approximately 10^8 $M_\odot$ (Longair 2011).
Another hint for black holes is the apparent superluminal motion of particles in jets, which will be explained in Sect. 3.3.2. The outflow of particles in these jets has high relativistic velocities near the speed of light. To reach such velocities they have to originate from regions with escape velocities of this magnitude. The only known objects, which are compact enough to be a candidate are black holes and neutron stars. But neutron stars cannot reach the required high mass, which can be estimated by the Eddington-limit. Besides, it explains that the jets have to arise and be accelerated very close to the Schwarzschild-Radius of the SMBH.
Having a SMBH in the center is not a feature solely of AGN, they can also be found in other galaxies like our Milky Way known as Sagittarius A* (Sgr A*), which is studied to learn more about SMBHs (Eckart & Genzel 1996; Doeleman 2008).

2.1.2. The regions around the black hole

The SMBH is surrounded by an accretion disk. In the ultraviolet/optical wavelengths a peak can be detected, which is called the *big blue bump* and comes from thermal emission of the accretion disk near the black hole (r $\sim 10^{-3}$ pc). The more distant regions from the black hole and the accretion disk are the *broad line region* (BLR), the *torus of dust* and the *narrow line region* (NLR). The BLR and NLR are gas clouds surrounding the black hole and bound by gravity. The cold dust comprising torus around the central region (r $\sim$ 1 - 10 pc) absorbs the light and blocks the view into the central region depending on the line of sight.

The Broad Line Region

The BLR are very dense clouds with high temperatures. The variability of the widths in the observed broad lines leads to the assumption that this region is in close proximity to the accretion disk (r $\sim$ 0.01 - 0.1 pc). It is the origin of the detected broad lines probably resulting of Doppler broadening caused by turbulent motion of the clouds. These broad lines reach widths corresponding to velocities of about $v \sim 10^3$ - 10^4 km s^{-1} (Osterbrock & Mathews 1986; Sulentic et al. 2000). If this is caused by thermal broadening the clouds would have temperatures of T $\sim 10^{10}$ K, where the atoms would be ionized completely and no emission lines would be observable. So the broadening has to be influenced by the velocities of these clouds and consist of a gas with very high density ($n_e > 10^9$ cm^{-3}) (Sulentic et al. 2000).

The Narrow Line Region

In the NLR forbidden lines are observed as well. The narrow lines have widths of a few hundreds km s^{-1} (Osterbrock & Mathews 1986). The forbidden lines are an indicator, that this region is less dense ($n_e \sim 10^3$ cm^{-3}) and colder compared to the BLR and thus the NLR is more distant from the black hole (r $\sim$ 100 - 1000 pc) (Sulentic et al. 2000).

2.1.3. The Jets

Perpendicular to the accretion disk collimated, highly relativistic outflow of particles called *jets* in both directions can be found (Bridle & Perley 1984). These jets can be observed in radio-loud AGN (Kellermann et al. 1989) and in most cases only one direction is visible. Because of *relativistic beaming* one jet gets boosted in luminosity while the other is weakened. Therefore the boosted is commonly named *jet* while the weakened one is called *counterjet*. These jets can be observed in the radio, optical and x-ray band. In the radio band they can reach scales up to $\sim$ Mpc. Modern instruments can resolve the jets on sub-pc scales. These outflows interact with the intergalactic medium on kpc to Mpc scales and produce lobes on either side, which are observable in the radio band.

Observed velocities of jet features on sub-pc scales can reach superluminal motion (up $\sim 50c$) which will be discussed in Sect. 3.3.2.

2.2. Types of AGN

Historically different types of AGN were introduced to classify the observed properties in different wavebands (Lawrence 1987). These classification are mainly based on features detected by optical measurements. Another characteristic feature is the radio emission. They are *radio-loud* and *radio-quiet* AGN (Peacock et al. 1986). Radio-quiet AGN show only weak radio emission. Other features are mainly provided by optical measurements.

Seyfert galaxies

Carl Seyfert (1943) found several galaxies with an extraordinarily bright point-like nucleus in the optical wavelengths. Later the Seyfert galaxies were divided into two types (Khachikyan & Weedman 1971): Type 1 and Type 2. While *Seyfert 1* galaxies have both broad and narrow forbidden emission lines, *Seyfert 2* galaxies only have narrow forbidden lines. These lines can reach a Doppler broadening equivalent to velocities up to 10^4 km s^{-1} for the broad lines and several hundreds km s^{-1} for the forbidden narrow lines, which is significantly larger than the characteristic velocities found in normal galaxies like rotational velocities. After studies of many Seyfert galaxies intermediate types were found like *Seyfert 1.5* or *Seyfert 1.8*. Usually Seyfert galaxies show only weak radio emission and are therefore considered as radio-quiet, but also a few radio-loud Seyfert 1 galaxies with weak broad line features had been found and named *radio-loud narrow line Seyfert 1* (Komossa et al. 2006).

Quasars

Quasar stands for *quasi-stellar radio source*. They have spectral characteristics similar to Seyfert galaxies, but higher bolometric brightness values and with weaker absorption and narrow lines. These objects were found in radio surveys and could be identified with observed optical point-like sources. But there are also sources with radio weak emission (Kellermann et al. 1989). Those radio-quiet ones were named *quasi-stellar objects* (QSO), while historically the name quasar is used for radio-loud ones. Therefore a distinction between QSOs and Seyferts is difficult, but mainly if the host galaxy cannot be identified as a spiral galaxy, it is a QSO. Today the distinction between QSO and quasar with the different radio emission is not very much in use. There are about ~ 10 times more radio-quiet QSOs than radio-loud ones (Kellermann et al. 1989).

LINERs

Low-Ionization Nuclear Emission Regions (LINER) are radio-weak AGN with low variability. Their optical spectrum looks like Seyfert type 2 but their emission lines of low-ionization states are greater than the ones of Seyfert 2 (Heckman 1980).

Radio galaxies

Radio galaxies are the radio-loud counterpart of Seyfert galaxies. They show strong radio emission from the nucleus. In the optical wavelengths they are divided into two sub-classes like the Seyferts: *broad line radio galaxies* (BLRG) and *narrow line radio galaxies* (NLRG). The optical luminosity and the extended radio emission from the nucleus are the characteristic features to differentiate them from quasars.
While the optical spectral properties distinguish between BLRG and NLRG, the extended radio morphology was defined into two classes by Fanaroff & Riley (1974): *Fanaroff-Riley Type 1* (FR1) galaxies and *Fanaroff-Riley Type 2* (FR2) galaxies. In FR1 galaxies the bright core is dominating and two jets can be observed from either side of the core. With increasing distance the luminosity of the jets decreases. In contrast to FR1 the FR2 galaxies show dominating lobes, a weak jet and a less dominating core. Also only one side of the two jets is visible and the luminosity of this jet increases with the distance from the core. These extended radio emissions reach scales from kpc up to Mpc.

Blazars

Blazars are compact unresolved radio-loud objects with varying intensities in the emission. They show strong polarized emission in the optical wavelengths and only weak emission lines. This class is divided into sub-classes. One class are the *BL Lac objects* with almost no emission lines. It was named after BL-Lacaertae, which was a strong radio emitter, compact and with a variable emission (Hoffmeister 1929). Another subclass are *optically, violently variable* objects (OVV). OVV objects have broad emission lines, high variability and are weaker in the radio than BL Lacs but stronger in the optical. The third sub-class are the *flat-spectrum radio quasars* (FSRQ), which show broad emission lines and are more luminous than the BL Lacs.

Table 2.1.: Summary of unification scheme

	Type 1 (broad lines)	**Type 2** (narrow lines)
radio-quiet	Seyfert 1 radio-quiet quasar	Seyfert 2 radio-quiet quasar
radio-loud	BLRG, Blazar (BL Lac, OVV, FSRQ) radio-loud quasar	NLRG (FR1 + FR2) radio-loud quasar, LINER
	increasing angle at the line of sight $\longrightarrow$	

2.3. Unification Model

As shown in Sect. 2.2 many of the different AGN types have common properties (Lawrence 1987). Based on the observations and features a unification model has been developed by Antonucci (1993) and Miller (1994). In this model a typical AGN contains a SMBH in its center, surrounded by the accretion disk, a fast rotating broad line region, a torus of cold dust and a narrow line region. The radio-loud types have also a collimated jet perpendicular to the accretion disk.
The main part of the unification model is the dependency of the viewing angle to the galaxy. With a line of sight about perpendicular to the jet axis the dust torus hides the BLR of the galaxy, so the broad emission lines are missing in the spectra. The angle to the line of sight explains the apparent superluminal motion of the jets, which will be discussed in Sect. 3.3.2. This can explain the difference between FR1 and FR2 galaxies. Looking into the collimated jet causes the point-like images of blazars, while an angle between torus and jet permits the possibility to observe the emission line of BLR and NLR.
The other classification criterion is the luminosity. Some types have similar properties and inclination angles but differ in the luminosity. For example the main difference between a Seyfert 1 and a radio-quiet quasar is the luminosity but the angle of the line of sight can be the same.
Tab. 2.1 and Fig. 2.2 show how the unification model works for the different angles and the distinction between radio-quiet and radio-loud galaxies, which are sub-divided by their properties like the luminosity.

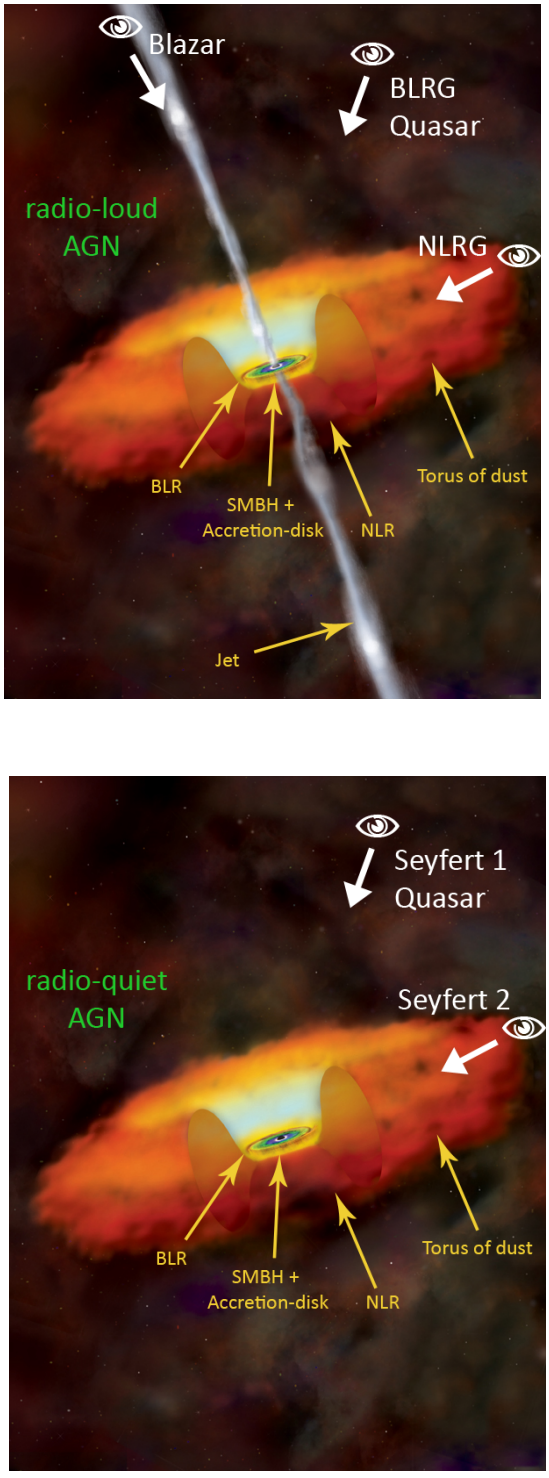

Figure 2.2.: Summary of the unification model. The first image (top) shows the model with different angles of the line of sight for radio-loud AGN, while the second one (bottom) shows the same for radio-quiet AGN. Credit: NASA/CXC/M.Weiss

3. Theoretical Background

In order to understand AGN and especially the radio observations of jets, it is important to describe the underlying physical concepts. This chapter will give an overview of the theory based on textbooks by Rybicki & Lightman (1979),Longair (2011) for the radiation processes, Marscher (2009), Krolik (1999) for the jet-physics and Burke & Graham-Smith (2010), Thompson et al. (2001) for the interferometry part. More detailed derivations can be found in these books.

3.1. Bremsstrahlung

Accelerated charged particles emit radiation which can be described by classical electrodynamics of moving charges. *Larmor's formula* (3.1.2) gives the emitted energy over an area $r^2 \mathrm{d}\Omega$ at an angle Θ and at a distance r, where q is a single charge accelerated of $\dot{\vec{v}}$ by an electric field, c the speed of light and ϵ_0 the electric constant:

$$-\frac{\mathrm{d}E}{\mathrm{d}t} = \int_0^\infty \frac{q^2|\dot{\vec{v}}|^2 \sin^2(\Theta)}{4\pi c^3} d\Omega = \int_0^\pi \frac{q^2|\dot{\vec{v}}|^2 \sin^2(\Theta)}{4\pi c^3} 2\pi \sin(\Theta)\mathrm{d}\Theta \tag{3.1.1}$$

$$\Rightarrow -\frac{\mathrm{d}E}{\mathrm{d}t} = \frac{2q^2|\dot{\vec{v}}|^2}{3c^3} = \frac{|\ddot{\vec{p}}|^2}{3c^3} \tag{3.1.2}$$

$\ddot{\vec{p}} = q\dot{\vec{v}}$, where $\vec{p}$ is defined as the electric dipole moment. The emission of the particle is polarized and because of the dependency of $\sin^2(\Theta)$ there is no emission in direction of the acceleration.
Using Fourier transformation of the acceleration and *Parseval's theorem* the emission of energy per unit time t and frequency ω can be derived and gives:

$$\frac{\mathrm{d}E(\omega)}{\mathrm{d}t\,\mathrm{d}\omega} = \frac{4\,q^2|\dot{\vec{v}}(\omega)|^2}{3c^3} \tag{3.1.3}$$

Integration over all particles of this expression gives the spectrum of the particle emission.
For relativistic velocities an adjustment is needed. Because of the Lorentz invariance of the energy rate ($\mathrm{d}E/\mathrm{d}t$) follows with a Lorentz transformation with the acceleration four-vector of the particle for relativistic velocities:

$$\frac{\mathrm{d}E}{\mathrm{d}t} = \frac{2q^2\gamma^4}{3c^3}(|\dot{\vec{v}}_\perp|^2 + \gamma^2|\dot{\vec{v}}_\parallel|^2) \tag{3.1.4}$$

where $\gamma = (1 - v^2/c^2)^{-1/2}$ (known as *Lorentz factor*) and the acceleration $\dot{\vec{v}}$ is divided into the parallel and perpendicular components $\dot{v_\parallel}$ and $\dot{v_\perp}$.
If a charged particle is decelerated in a Coulomb field for example of another particle, the emitted radiation is called *bremsstrahlung* or *free-free emission*. This process can be described classically and corrected with terms derived from quantum mechanics.
This derivation leads to an energy loss over time t, frequency ω and volume V for the non-relativistic bremsstrahlung emitted by a single charged particle:

$$\frac{\mathrm{d}E(\omega)}{\mathrm{d}t\,\mathrm{d}\omega\,\mathrm{d}V} = \frac{16\pi Z^2 q^6 N_i N_e}{3\sqrt{3}c^3 m_e^2 v} g_{ff}(\omega, v) \tag{3.1.5}$$

where N_e is the electron (charge q) density, N_i the ion (charge Z) density, m_e the electron mass and $g_{ff}(\omega, v)$ the *Gaunt factor*. The Gaunt factor is a function of the frequency of the radiation and the energy of the electron (depending on the velocity v respectively the temperature T for a Maxwellian-Boltzmann distribution for an averaged velocity).
Averaging over the thermal distribution of the velocities gives the *thermal bremsstrahlung*. The probability $\mathrm{d}P$ that a particle has a velocity in the velocity range $\mathrm{d}^3\vec{v}$ is

$$\mathrm{d}P \propto e^{-E/kT}\mathrm{d}^3\vec{v} = exp\left(-\frac{m_e v^2}{2kT}\right)\mathrm{d}^3\vec{v} \tag{3.1.6}$$

Integrating over this probability and using $\mathrm{d}\omega = 2\pi\mathrm{d}\nu$ leads to a spectral emissivity of

$$\frac{\mathrm{d}E(\omega)}{\mathrm{d}t\,\mathrm{d}\nu\,\mathrm{d}V} = \frac{2^5\pi Z^2 q^6}{3m_e c^3}\left(\frac{2\pi}{3m_e kT}\right)^{\frac{1}{2}} N_e N_i \bar{g}_{ff}(\nu, T) e^{-h\nu/kT} \tag{3.1.7}$$

where $\bar{g}_{ff}(\nu, T)$ is a velocity averaged Gaunt factor.

The counterpart of free-free emission is the free-free absorption where an unbound electron absorbs a photon moving in a Coulomb field. This can be described by the thermal bremsstrahlung absorption coefficient a_{ff} :

$$a_{ff} = \frac{4q^6 Z^2}{3m_e kc}\left(\frac{2\pi}{3m_e k}\right)^{\frac{1}{2}} T^{-3/2} N_e N_i \bar{g}_{ff}(\nu, T)\nu^{-2} \tag{3.1.8}$$

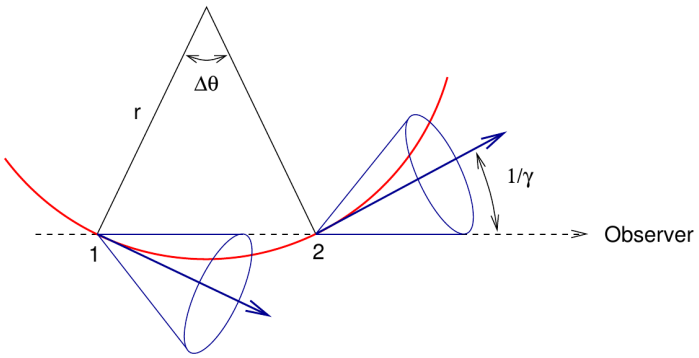

Figure 3.1.: Particle emitting synchrotron radiation in a cone on its helical path through the magnetic field (Rybicki & Lightman 1979)

3.2. Synchrotron Radiation

When charged particles get accelerated by a magnetic field $\vec{B}$ through the Lorentz force they radiate similar to the bremsstrahlung. The radiation of non-relativistic particles is known as *cyclotron radiation*. For relativistic velocities it is called *synchrotron radiation* or *magnetobremsstrahlung*.

The magnetic field $\vec{B}$ creates a helical motion of the charged particle and can be described with:

$$m_e \gamma \dot{\vec{v}} = \frac{q}{c} \vec{v} \times \vec{B} \tag{3.2.1}$$

with γ as the Lorentz factor as in eq. 3.1.4, the relativistic velocity $\vec{v}$, the acceleration $\dot{\vec{v}}$, the mass of the electron m_e and c the speed of light. The helical motion has a frequency known as the gyrofrequency ω_g with $B = |\vec{B}|$ and $v = |\vec{v}|$:

$$\omega_g = \frac{qB}{\gamma m_e c} \tag{3.2.2}$$

Thus the total emitted energy of a single charged particle can be calculated with:

$$-\frac{\mathrm{d}E}{\mathrm{d}t} = \frac{4}{3} \sigma_T c \beta^2 \gamma^2 \frac{B^2}{8\pi} \tag{3.2.3}$$

with the Thomson cross section σ_T and $\beta = v/c$. Using the relation $E = \gamma m_e c^2$ it can be shown, that the energy per time is $\propto m_e^{-2}$ and for this reason the synchrotron radiation of massive particles is low and negligible.

The emission by a single particle has a dipole characteristic (as seen in eq. 3.1.2) in the rest frame of the electron. The Lorentz transformation into the laboratory system changes the emission characteristic of relativistic particles into a cone with an opening angle $\propto \gamma^{-1}$. Depending on the characteristic gyration frequency ω_c the observer sees

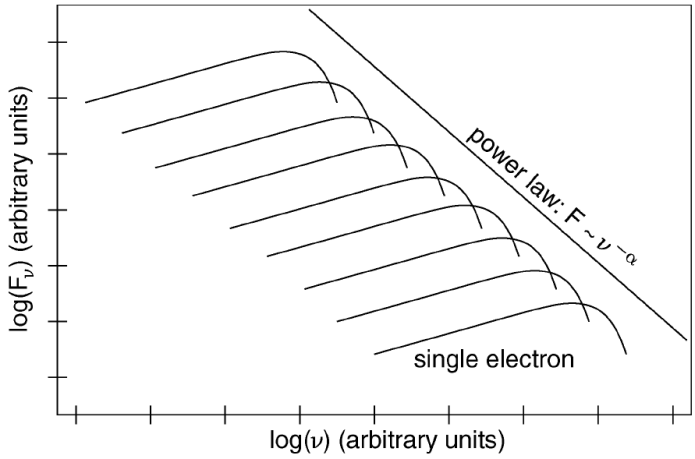

Figure 3.2.: Single particle spectra leading to a powerlaw $P_\nu \propto \nu^\alpha$ (Schneider 2008)

only a short pulse when the emission cone is oriented in his direction. Fourier analysis leads to an observed spectrum varying around ν_c with

$$\nu_c = \frac{\omega_c}{2\pi} = \gamma^2 \frac{qB}{m_e c} \tag{3.2.4}$$

Considering a non-thermal electron distribution $n(\gamma)$, leads to

$$P_\nu = -\frac{\mathrm{d}E}{\mathrm{d}t} = \int_1^\infty P_\nu(\gamma) n(\gamma) d\gamma \tag{3.2.5}$$

$$\Rightarrow n(\gamma)d\gamma = n_0 \gamma^{-p} d\gamma \tag{3.2.6}$$

where p is the *particle distribution index*. Integrating over a distribution of electrons emitting at the corresponding frequency ν_c, shows that

$$P_\nu \propto \nu^{-\frac{p-1}{2}} \tag{3.2.7}$$

$$\text{where } \alpha = \frac{1-p}{2} \tag{3.2.8}$$

with α known as the *spectral index*.
Thus we have an electron distribution described by a power-law leading to a spectrum also consisting of a power-law.

Similar to the bremsstrahlung in Sect. 3.1 in synchrotron radiation the *synchrotron self-absorption* occurs with a self-absorption coefficient a_S

$$a_S \propto \nu^{-\frac{p+4}{2}} \tag{3.2.9}$$

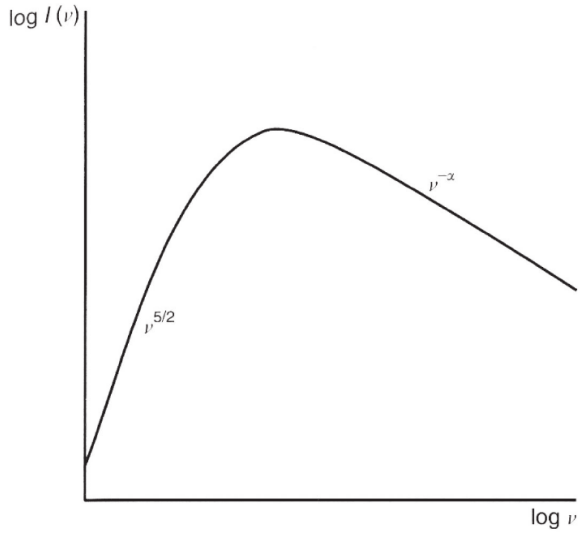

Figure 3.3.: Broken power-law with synchrotron self absorption (Longair 2011)

The optical depth τ_ν can be defined as

$$\tau_\nu = \int_{s_0}^{s} a_S(s')\mathrm{d}s' \tag{3.2.10}$$

where ds is the distance the beam travels corresponding to the loss of intensity. If $\tau_\nu < 1$ the medium is called *optically thin* or *transparent*, while $\tau_\nu > 1$ means the medium is *optically thick* or *opaque*. The frequency near $\tau_\nu = 1$ is called turnover frequency ν_t which leads to a broken power-law of the spectrum:

$$P_\nu \propto \quad \nu^{\frac{5}{2}} \qquad \text{for } \nu < \nu_t \tag{3.2.11}$$

$$P_\nu \propto \quad \nu^{\frac{1-p}{2}} \qquad \text{for } \nu > \nu_t \tag{3.2.12}$$

3.3. Physics of extragalactic Jets

3.3.1. Theories on Formation of Jets

The extragalactic jets observed at many scales with radio telescopes and seen in the optical and X-rays are not fully understood. But many theories have been formed using magnetohydrodynamics (MHD), general relativity (GR) and electrodynamics. Parts of the mechanisms seem to be understood but some processes are not completely uncovered.

There are strong pressure gradients needed to push out matter in a collimated flow at relativistic velocities. Some consider this can be reached with gas dynamics. Marscher (2009) argued that jets with Lorentz factors > 10 and a collimation $< 1°$ cannot be formed through gas dynamics. Considering this, only magnetic forces have enough power to be the driving force launching such jets. Magnetic forces of this required strength can be created by a spinning black hole and/or the accretion disk. Through spinning the magnetic field lines wind up into a helix. The decreasing magnetic pressure in the distance of the black hole creates a strong pressure gradient which can accelerate the matter. Both theories, the magnetic fields and the gas dynamics, lead to a gradual acceleration with an opening angle inverse proportional to the final Lorentz factor. Therefore, it is expected that the highest intensity of observed emission is found at the core and the close regions.
In distance of the black hole the gas dynamic model becomes valid and the jet builds shock waves which can be observed as jet components in the radio band. These components can be quasi-stationary or move with velocities up to apparent superluminal speed. The expanding jets can be disturbed by Kelvin-Helmholtz instabilities which result in turbulences and change the straight jet axis. The shocks can decrease the velocity of the particles or can even accelerate them if the particle can be reflected multiple times at the shock front.

The jet in the radio band consists of different features: the core, the quasi-stationary features and the moving features. The core is a stationary feature closest to the black hole where the jet region changes from optically thick to optically thin ($\tau = 1$). Therefore it moves with changing frequency as seen in Fig. 3.4 (Lobanov 1998; Hada et al. 2011; Kovalev et al. 2008). This core-shift is not observed always.
The quasi-stationary features can be produced by instabilities or shocks for recollimation of the jet. They seem stationary or have subluminal motions. At higher distances away from the core the jet can interact with the intergalactic medium and create the radio lobes. The interaction with the intergalactic medium leads to instabilities in the jet and deceleration of the particles.
The superluminal components are bright and represent regions of higher relativistic electron density and/or magnetic field than the ambient jet. They also could be regions of turbulent plasma with accelerated electrons due to second order Fermi acceleration.

3.3.2. Superluminal motion and relativistic beaming

Superluminal motion

As already mentioned before in some jets the components seem to move with velocities higher than the speed of light. The effect of superluminal motion is caused by the geometrical connection of the jet axis to the line of sight. While one component is stationary in the laboratory frame at time $t = 0$ in the distance d to the observer, a second blob travels a distance of $\beta\Delta t \sin\theta$ projected to the sky with the passed time Δt

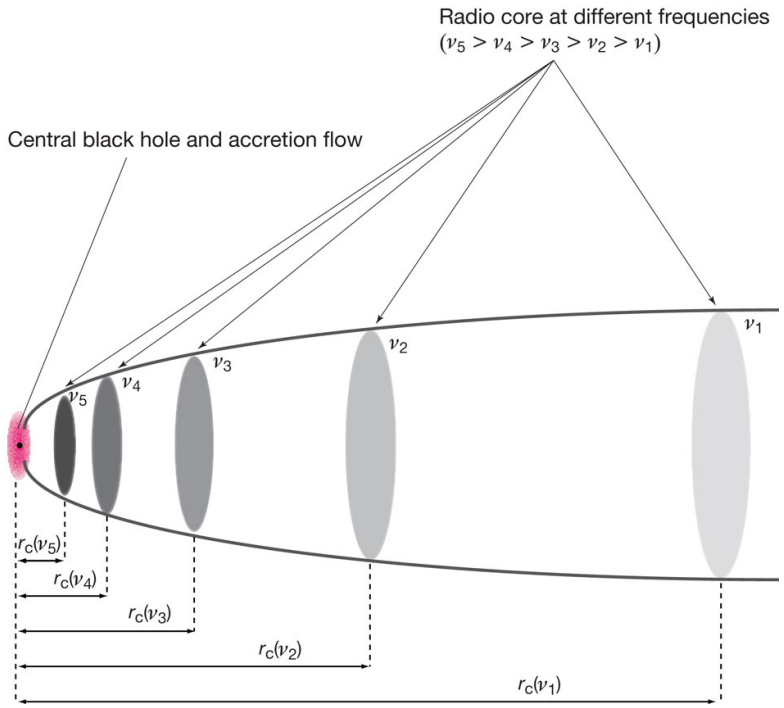

Figure 3.4.: Concept of core shifts in radio jets from Hada et al. (2011), where the radio core is shifted closer to the black hole with increasing frequencies.

and θ as the angle to the line of sight. This leads to an apparent speed of

$$v_{app} = \frac{v\sin\theta}{1 - \beta\cos\theta} \tag{3.3.1}$$

These velocities can reach $v_{app} > c$ for $\beta \approx 1$ and small $\theta = v/c$.

Relativistic beaming

In addition to this projection effect occurs a relativistic effect called *beaming*. Relativistically moving plasma particles undergo a Doppler shift:

$$\nu_{obs} = \frac{\nu_{emission}}{\gamma(1 - \beta\cos\theta)} \tag{3.3.2}$$

with the observed frequency ν_{obs} and the certain frequency $\nu_{emission}$. The Doppler factor D can be calculated:

$$D = \frac{\nu_{obs}}{\nu_{emission}} = \frac{\sqrt{1 - \beta^2}}{1 - \beta\cos\theta} \tag{3.3.3}$$

This shows the strong dependency of the angle to the line of sight. Because of the dependency on the flux S_ν of the frequency according to $S_\nu \propto \nu^{-\alpha}$ the angle has a

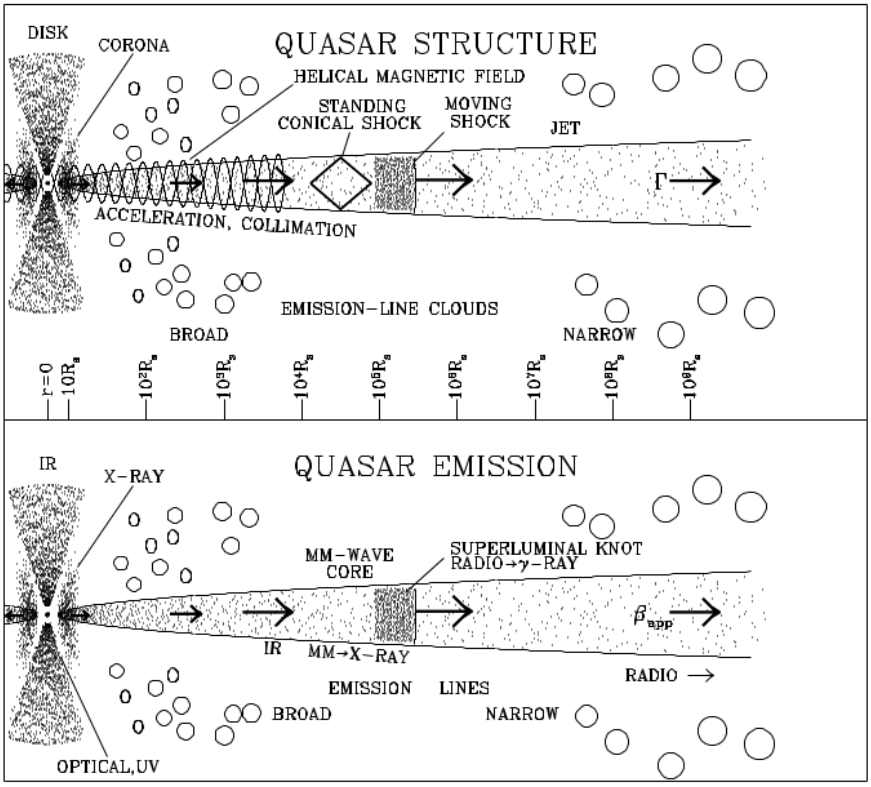

Figure 3.5.: Illustration of physical and emission components of a quasar with a relativistic jet from Marscher (2009). The scale is logarithmic in Schwarzschild radii to cover the wide range of distances.

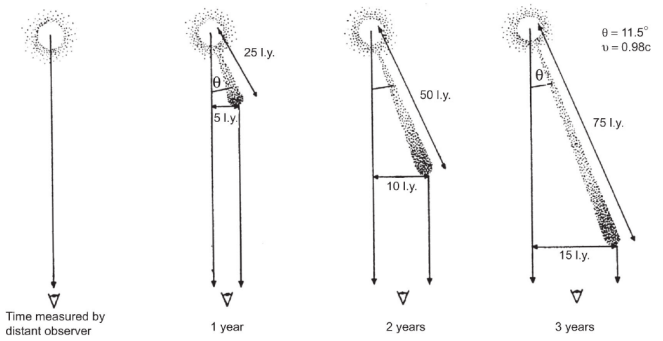

Figure 3.6.: Projection effect leading to apparent velocities faster than the speed of light at an angle $\theta = 11.5°$ to the line of sight. (Longair 2011)

prominent influence on the flux and spectrum. In a galaxy with two jets, the jet closer to the observer gets boosted ($S_{\nu 1}$), while the jet in the direction away from the observer is de-boosted ($S_{\nu 2}$), creating a ratio R:

$$R = \frac{S_{\nu 1}}{S_{\nu 2}} = \left(\frac{1 + \beta \cos\theta}{1 - \beta \cos\theta}\right)^{3+\alpha} \tag{3.3.4}$$

This is also the explanation why most of AGN show only one jet, because the counterjet gets de-boosted too much. With a know spectral index α the flux of the counterjet can be estimated and compared to the noise ratio.

3.4. Interferometry with radio telescopes

3.4.1. Radio telescopes

To achieve high resolution images in the radio band of extragalactic jets a technique known as *Very Long Baseline Interferometry* (VLBI) is used. A radio telescope has a parabolic reflector with a receiving device and a recording system. The incoming radio waves get reflected from the parabolic reflector and focused into the receiver. The angular resolution is defined by the Rayleigh criterion and can be approximated by

$$\sin(\alpha) \approx 1.22 \frac{\lambda}{D} \tag{3.4.1}$$

where α is the angular resolution, λ the observed wavelength and D the diameter of the reflector. Because radio waves have longer wavelengths compared to the optical band, a larger reflector is needed to achieve the same angular resolution.
Because of the nature of electromagnetic waves a reflector can be used for both emitting and receiving, therefore the beam can be seen as the radiation pattern of such an antenna. The FHWM (full width half maximum) of the main lobe defines the angular resolution, while the side lobes can be the origin of higher order maxima. In the simplified case the beam has the form of a sinc-function.
The detected radiation is measured in *Jansky* (Jy), a unit describing the flux density:

$$1\text{Jy} = 10^{-26}\text{J s}^{-1}\ \text{m}^{-2}\ \text{Hz}^{-1} \tag{3.4.2}$$

The received power depends on the flux density $S(\nu)$ and the effective collecting area of the telescope A_{eff}.

$$P = \int_0^\infty \mathrm{d}\nu A_{eff}(\nu) S(\nu) \tag{3.4.3}$$

$$\text{with } S(\nu) = \int \mathrm{d}\Omega B(\nu, \Theta, \Phi) \tag{3.4.4}$$

where $B(\nu, \Theta, \Phi)$ is the brightness distribution of the sky integrated over the solid angle $\mathrm{d}\Omega$. The output quantity is called *antenna temperature* T_A, measured in Kelvin, and corresponds to the power density coming from the antenna at the frequency ν that is needed to generate this temperature in a hypothetical resistor. The output noise power of a black body corresponds to antenna output of the observed object at frequency ν. This quantity is called *brightness temperature* T_b. Using the Rayleigh-Jeans approximation ($h\nu \ll kT$) of the Planck formula the brightness temperature can be calculated with the following equation:

$$T_b = \frac{B(\nu, \Theta, \Phi) c^2}{2k\nu^2} \tag{3.4.5}$$

$$S_\nu = \int \mathrm{d}\Omega B(\nu, \Theta, \Phi) = \frac{2k\nu^2}{c^2} \int \mathrm{d}\Omega T_b \tag{3.4.6}$$

where c is the speed of light and k the Boltzmann-constant.

3.4.2. Two element interferometer

As mentioned before the angular resolution is dependent on the diameter of the telescope. To improve this quantity the interferometry technique can be used. As seen in Fig. 3.7 two radio telescopes can be connected. They point in the same direction but one has a delay τ_g of the signal through the geometry which has to be accounted for by

$$\tau_g = \frac{b}{c} \sin\theta \tag{3.4.7}$$

The correlator integrates and combines the two signals and generates an output of the two amplitudes (voltages) of the time-averaged product known as *cross power product* R_{xy}.

$$R_{xy}(\tau_g) = A(\vec{\mathbf{s}}) S \cos(2\pi\tau_g\nu) = A(\vec{\mathbf{s}}) S \cos\left(\frac{2\pi\nu b \sin\theta}{c}\right) \tag{3.4.8}$$

with the effective area $A(\vec{\mathbf{s}})$ of the telescope depending on the direction $\vec{\mathbf{s}}$ and the source flux S. The correlator introduces another time delay τ_i. A reference position $\vec{s_0}$ close to a source with the position $\mathbf{s}$ with the condition $\tau_g = \tau_i$ is taken. This reference position

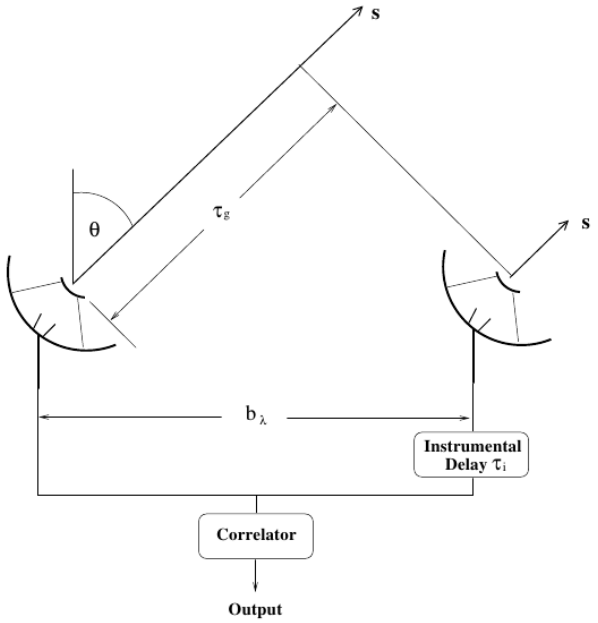

Figure 3.7.: Geometry of a two-element interferometer. The internal delay compensates the geometrical path delay τ_g (after Burke & Graham-Smith (2010))

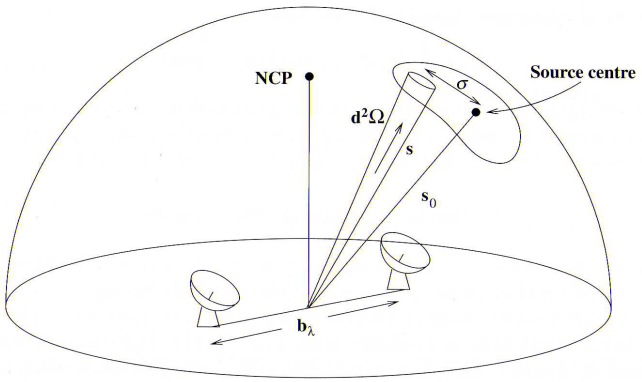

Figure 3.8.: Contribution of a small receiving element in the direction **s** and solid angle dΩ; NCP stands for the North Celestial Pole (Burke & Graham-Smith 2010)

$\vec{s_0}$ is known as *phase-tracking centre*. τ_i compensates the geometrical time delay and then the direction to the source in respect to the phase-tracking centre has the relation:

$$\vec{\mathbf{s}} = \vec{s_0} + \vec{\sigma} \tag{3.4.9}$$

where the displacement $\vec{\sigma}$ is a vector normal to $\vec{s_0}$.
To process the signal Fourier transformation has to be used. The cross power product is the convolution of the array and the source, leading to the visibility function V

$$V = \int A(\sigma) B_\nu(\sigma) \exp(i2\pi\vec{\mathbf{b}}\sigma) \mathrm{d}\Omega \tag{3.4.10}$$

with $B(\sigma)$ as the brightness of the source and $\vec{\mathbf{b}}$ the distance between two telescopes called *baseline*.
Another coordinate system is introduced for the correlator response. The baseline vector can be described by a right-handed rectilinear coordinate system (u, v, w) in units of the observed wavelength. Then s_0 defines the w-direction and is perpendicular to the (u, v)-plane. Then the σ vector is parallel to the (u, v)-plane. Also l, m are used for the directions of the cosines of u, v forming the (u, v)-plane.

$$u = \frac{\nu b \cos\theta}{c} \tag{3.4.11}$$

$$v = \frac{\nu b \sin\theta}{c} \tag{3.4.12}$$

$$\Rightarrow V = \int_{4\pi} A(l,m) B_\nu(l,m) \exp(i2\pi(ul+vm)) \frac{\mathrm{d}l\mathrm{d}m}{\sqrt{1-l^2-m^2}} \tag{3.4.13}$$

In the (u, v)-plane the visibility can be measured, which corresponds to the Fourier transformation of the source brightness distribution convolved with the synthesized beam of the array.
The array can consist of more than two telescopes. More telescopes lead to a better coverage in the (u, v)-plane. The coverage is also dependent on the angle of the source and the observing time (for an example see Fig. 3.12). The arrays use the movement of the earth to change the observer position to the source.

3.4.3. The Very Long Baseline Interferometry (VLBI)

To achieve the best angular resolution very long baselines are needed (see Fig. 3.10). The array can even consist of different telescopes not directly connected. Fig. 3.11 shows an illustration of the concept of VLBI where the data are recorded and combined later.

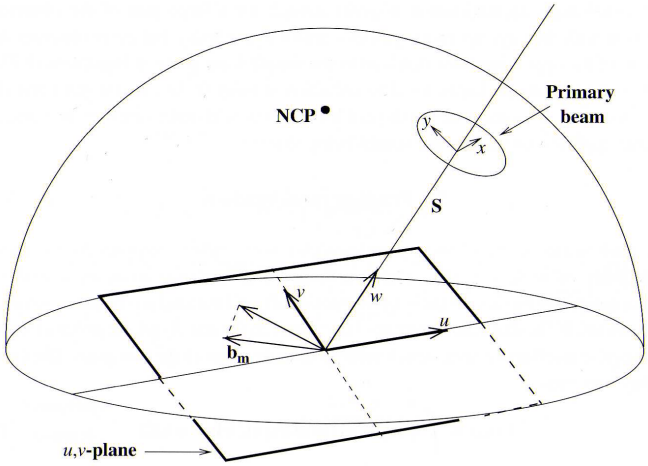

Figure 3.9.: The geometrical relation of the (u, v)-plane to the interferometer. x, y are used for the small-angle approximation of l, m parallel to u, v. (Burke & Graham-Smith 2010)

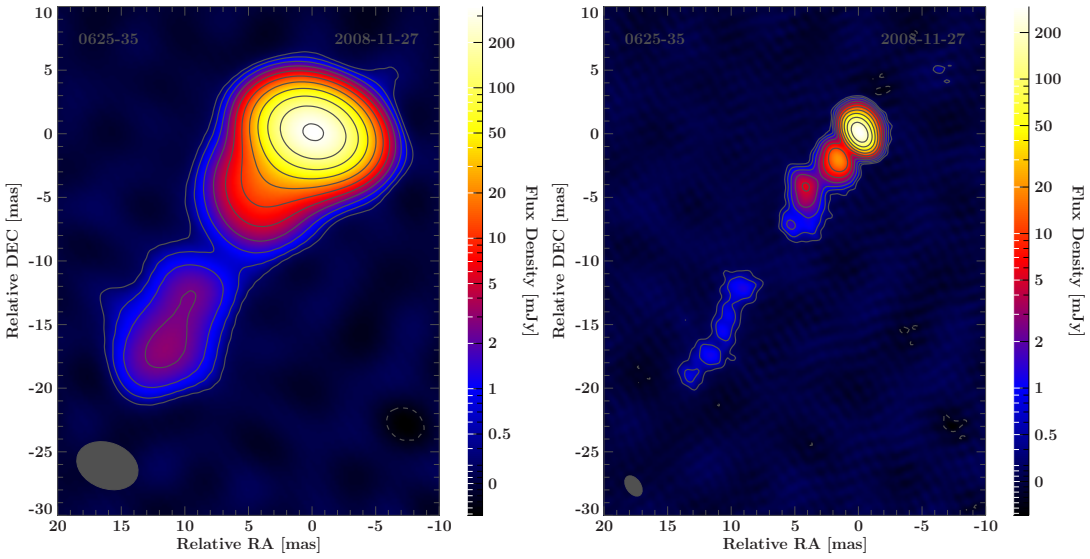

Figure 3.10.: Illustration of the importance of long baselines. On the left: observation of 0625-354 without the data points of the O'Higgins telescope. On the right: same observation with the O'Higgins data points included. In this example the influence of long baselines is clearly visible resulting in much better resolution and small scale structure.

To have the exact time an oscillator with a stable atomic frequency standard is needed at each station. Also the exact location on earth is needed to measure accurate phases at the different baselines.
At very long baselines weather or atmospheric conditions can influence the measurements and create errors. They lead to offsets in the frequency which have to be corrected in the process called *fringe fitting*. For this process Schwab & Cotton (1983) developed a global fringe fitting technique based on *closure phases*. Closure phases work with relations between the visibility values for all combination pairs of a triangle of telescopes, then the sum of all visibility phases is called closure phase. With this technique phase errors are neglected but the absolute position of the source gets lost.

3.4.4. VLBI surveys

Around the world exist various VLBI networks. Some of them where built for this purpose, others are combinations of existing radio telescopes for mutual observation sessions. For example the Very Long Baseline Array (VLBA) is an array of ten identical telescopes spread over North America observing the whole year. One of the most sensitive VLBI networks is the European VLBI Network (EVN) (Paragi et al. 2005). A network called Long Baseline Array (LBA) exists in Australia (Frater et al. 1992). Moreover in Great Britain exists a smaller network called MERLIN, which is the origin of the example for the (u, v)-coverage in Fig. 3.12.
These arrays are used for different surveys. One early survey to observe the milliarcsecond structure of radio sources was Pearson-Readhead-Survey (Pearson & Readhead 1981). This was the first survey from the Caltech-Jodrell bank surveys with three following surveys (Polatidis et al. 1995; Taylor et al. 1994, 1996).
A predecessor of the TANAMI program, the program of the observations in this work, is the SHEVE program where the LBA used additional telescopes to expand their array (Jauncey et al. 1994). Together with the LBA also existed a VLBI network using the satellite HALCA to expand the baseline into space called VSOP (Hirabayashi et al. 2000).
One of the successful current surveys to monitor AGN is the MOJAVE program (Kellermann et al. 1998; Lister & Homan 2005). It monitors about 300 AGN sources of the northern hemisphere in the current sample. The program not only monitors the objects in the radio-band but also aims for multi-wavelength studies of the sample (Arshakian et al. 2012) working together with *Fermi* (Lister et al. 2009b, 2011) and other observatories .

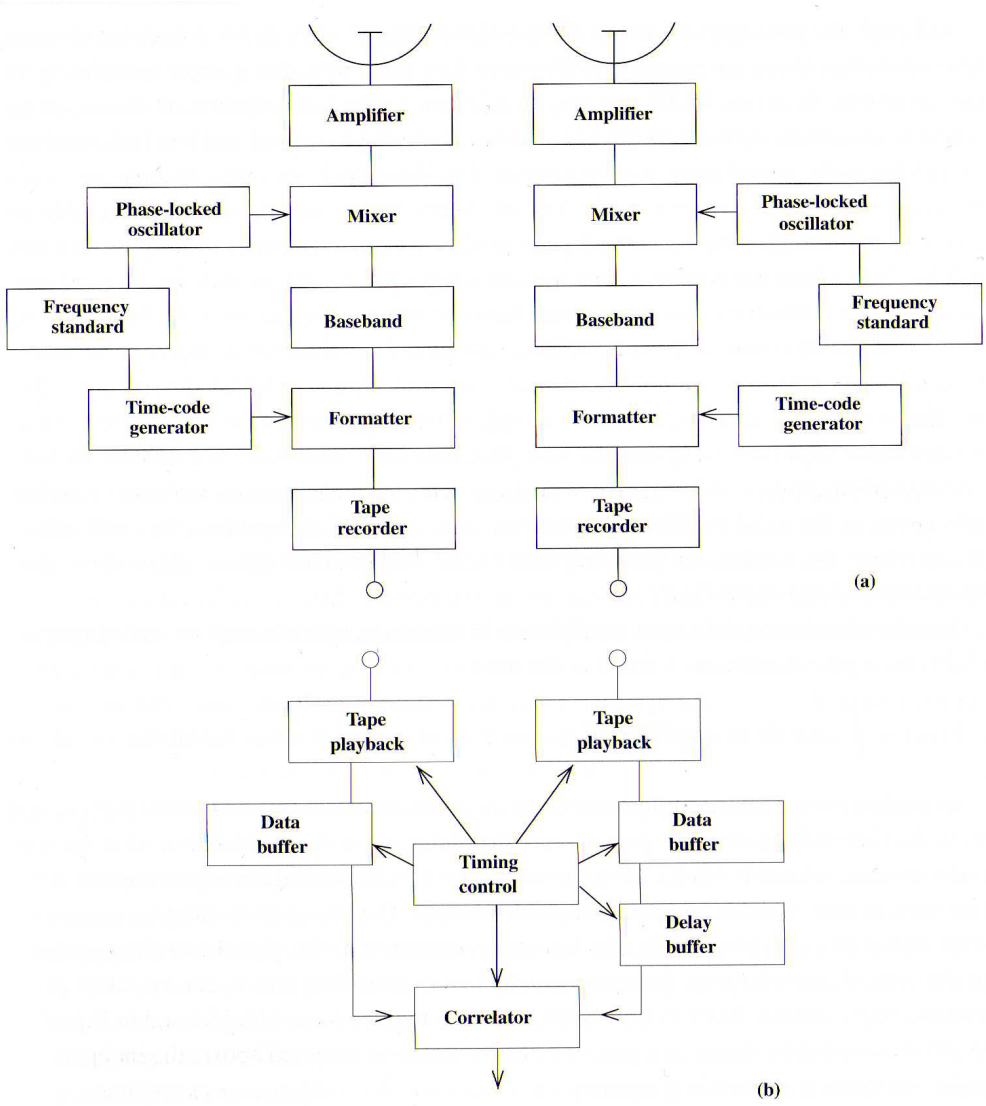

Figure 3.11.: Outline diagram of a VLBI system consisting of (a) two receiver stations and the correlator (b). (Burke & Graham-Smith 2010)

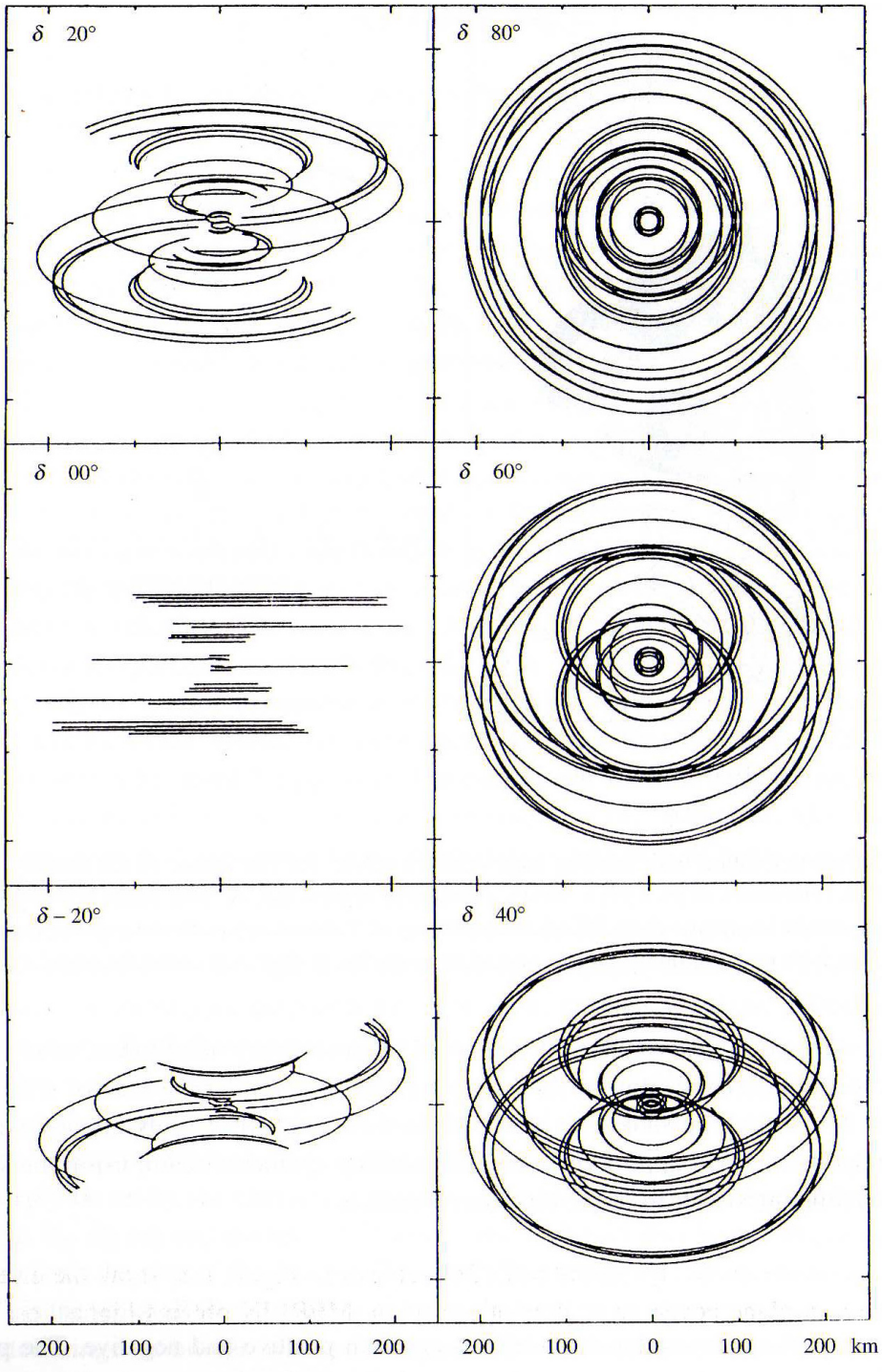

Figure 3.12.: Example of (u, v)-coverage at different angles for the MERLIN interferometer array with an 8-hour tracking (Burke & Graham-Smith 2010)

4. TANAMI & Data Analysis

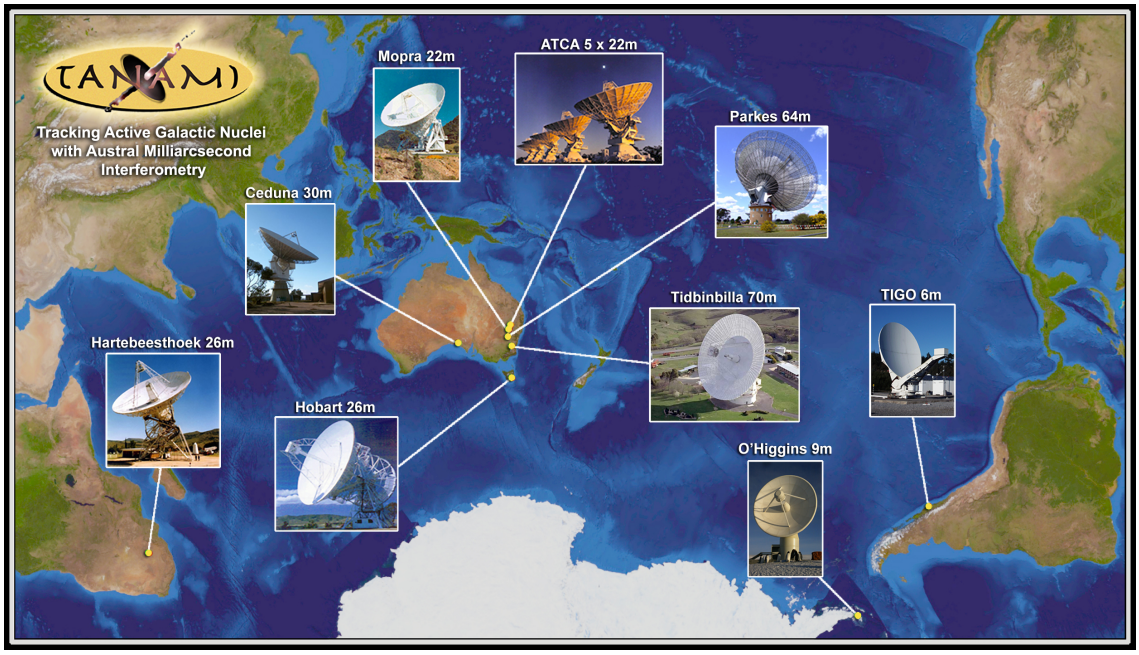

Figure 4.1.: Illustration of the TANAMI array in the Southern Hemisphere. Credit: M. Kadler (Univ. of Würzburg) and J.Wilms (Univ. of Nuremberg-Erlangen)

4.1. The TANAMI Project

TANAMI stands for **T**racking **A**ctive Galactic **N**uclei with **A**ustral **M**illiarcsecond **I**nterferometry. The program images and monitors AGN of the Southern Hemisphere with the LBA (Frater et al. 1992) and additional radio telescopes at frequencies of 8.4 GHz (X-Band) and 22 GHz (K-Band) listed in Tab. 4.1 and Fig. 4.1. Compared to the VLBA in North America consisting of identical telescopes and technical equipment, the LBA and the TANAMI array uses different telescopes which were not initially meant to do radio interferometry. This leads to more special properties like different sizes or sensitivities that have to be considered for the calibration. The antenna at Hartebeesthoek in South Africa has participated in LBA observations before the TANAMI project. By

Table 4.1.: Telescopes being part of the TANAMI array

Telescope name	Diameter (meters)	Location	Frequency bands*
Parkes[1]	64	Parkes, New South Wales, Australia	X, K
ATCA[1]	5 x 22	Narrabri, New South Wales, Australia	X, K
Mopra[1]	22	Coonabarabran, New South Wales, Australia	X, K
Hobart[1]	26	Mt. Pleasant, Tasmania, Australia	X, K
Ceduna[1]	30	Ceduna, South Australia, Australia	X, K
DSS43[2]	70	Tidbinbilla, ACT, Australia	X, K
DSS45[2]	34	Tidbinbilla, ACT, Australia	X, K
Hartebeesthoek[3]	26	Hartebeesthoek, South Africa	X, K
O'Higgins[4]	9	O'Higgins, Antarctica	X
TIGO[4]	6	Concepción, Chile	X

* X-Band: 8.4 GHz, K-Band: 22.3 GHz
[1] Operated by the Australia Telecope National Facility (ATNF) and part of the Long Baseline Array (LBA)
[2] Part of NASA's Deep Space Network
[3] Operated by the National Research Facility of South Africa's National Research Foundation; not available between Sept. 2008 and Sept. 2010
[4] Operated by *Bundesamt für Kartographie und Geodäsie (BKG)*

adding the two telescopes TIGO and O'Higgins, the TANAMI program could significantly improve the (u, v)-coverage through the long baselines (also see Fig. 4.3 + 3.10). However the (u, v)-coverage misses some baselines in between, but this is hard to achieve because of the oceans at the corresponding distances. Additionally, the (u, v)-coverage is varying over time because not all telescopes are available in every epoch, for example Hartebeesthoek could not participate from Sept. 2008 until Sept. 2010 due to a major failure.

The monitoring complements the AGN data in the southern sky to the monitoring programs of the north like MOJAVE (Lister et al. 2009a). A part of the TANAMI sample was selected from a subsample of known and candidate γ-ray sources based on the data from *CGRO*/EGRET (Hartman et al. 1992) and based on a radio flux-density limit. This contained 43 blazars located south of -30° declination. In addition all known extragalactic radio sources south of -30° declination from the catalogue of Stickel et al. (1994) with a flux density above a limit of $S_{5GHz} > 2$ Jy and a flat radio spectrum (α

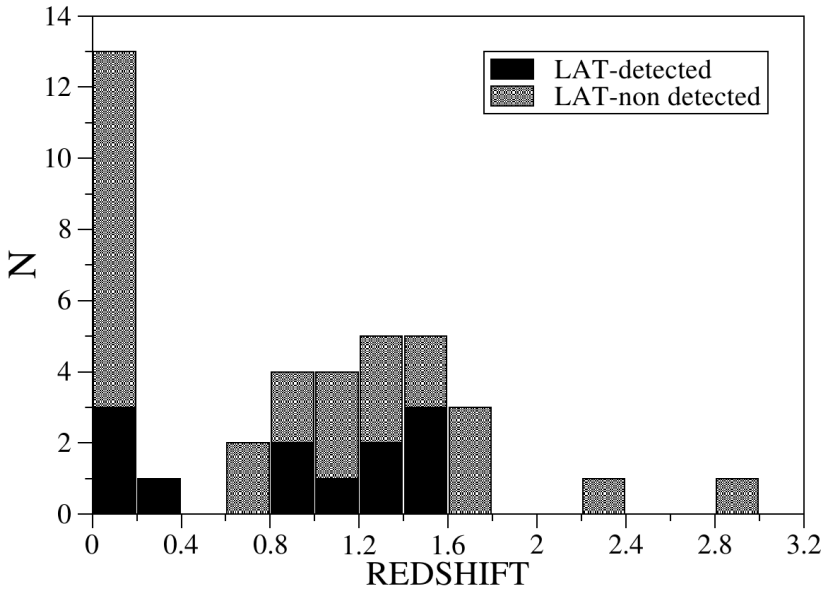

Figure 4.2.: Distribution of redshifts of the initial TANAMI sample with the detections of the *Fermi*/LAT in the γ-rays. (Ojha et al. 2010)

$>$ -0.5, $S \propto \nu^{+\alpha}$) have been added to the sample. This initial sample was expanded continuously with newly detected bright γ-ray sources detected by *Fermi*/LAT (Abdo et al. 2010b). The distribution of redshifts of the original sample is shown in Fig. 4.2.

TANAMI not only monitors the AGN in the radio band but it also studies the AGN in other wavelengths (Krauss 2013). The sample selection shows the connection to the high energy regime with *Fermi*, but often there are also correlated observations with *Swift* (UV/optical and X-rays) and *INTEGRAL* (X-rays) together with radio flux density measurements through the GHz band with the Australian Compact Array (ATCA), Ceduna, Hobart and Effelsberg to extend the radio monitoring. The Ceduna-Hobart-Interferometer with a baseline of 1700 km also provides follow-up observations of flaring sources recorded with *Fermi*/LAT (Blanchard et al. 2012).

The data are recorded on LBADRs (Long Baseline Array Disk Recorders). The correlation is accomplished with the DiFX software correlator (Deller et al. 2007) at Curtin University in Perth, Western Australia. With *AIPS* (National Radio Astronomy Observatory's Astronomical Image Processing System software) the correlated data get an inspection, initial editing and are being fringe fitted. For the amplitude calibration known flux values of prior observed sources are used.

First epoch analysis results are published by Ojha et al. (2010). Boeck et al. (2009) analysed the γ-ray properties of selected TANAMI sources. Besides the sample studies, there are the great sub-parsec scale observations and studies of Centaurus A with TANAMI from Mueller et al. (2011).

4.2. Data Reduction and Processing

To study the brightness distribution of the observed sources the visibility data have to be calibrated. After the *a-priori* calibration, the imaging process creates a map of the brightness distribution. For further studies regarding the core luminosities, brightness temperature or kinematic the the visibility data have to be modelled with Gaussian model components. With images at different frequencies, spectral index maps can be made showing the distribution of the spectral index in the areas appearing in both images.

4.2.1. Calibration

For the calibration the data from the correlator are loaded into *AIPS* (Astronomical Image Processing System) for inspection and selecting the data (Fomalont 1981; Greisen 1998). After flagging bad data, the *a-priori* calibration is processed following the steps from Diamond (1995).
In the first step of the *a-priori* calibration the amplitudes are corrected for instrumental and atmospheric opacity effects. Through the flux calibrators, the noise, the system sensitivities and temperatures, the difference parameters of the raw data output and the true input data of the source can be estimated and corrected through transfer functions. With this transfer function, the observed visibilities can be reconstructed and the next step can be performed.
The second step is the phase calibration. Like mentioned in Sect. 3.4.2 the delay for the phase tracking centre has to be accounted. In this step, the visibility phases have to be corrected for those extended structures and source position. The visibility phases have to be nearly constant so that they can be integrated coherently. Therefore, different corrections for every IF channel are made for the single band instrumental phase and the correction of the delay. This step does not correct all phase errors but only the visibility for instrumental effects. Atmospheric and geometric errors can still remain and can be corrected after this step through the fringe fitting, where the multiband residual phase and delay are accounted for.
After the calibration the corrected data are written into tables in FITS format (Flexible Image Transport System) developed by Wells et al. (1981). These files can be read and edited for imaging. However *AIPS* still keeps also the raw data and stores the corrections in separate files, so that the calibration can be undone or altered if needed.
For the TANAMI project these data calibration steps are performed by Dr. Roopesh Ojha at NASA's Goddard Space Flight Center.

4.2.2. Imaging

The imaging process transforms the calibrated data into images of brightness distribution. For this, a program called DIFMAP (Shepherd et al. 1994; Shepherd 1997; Taylor

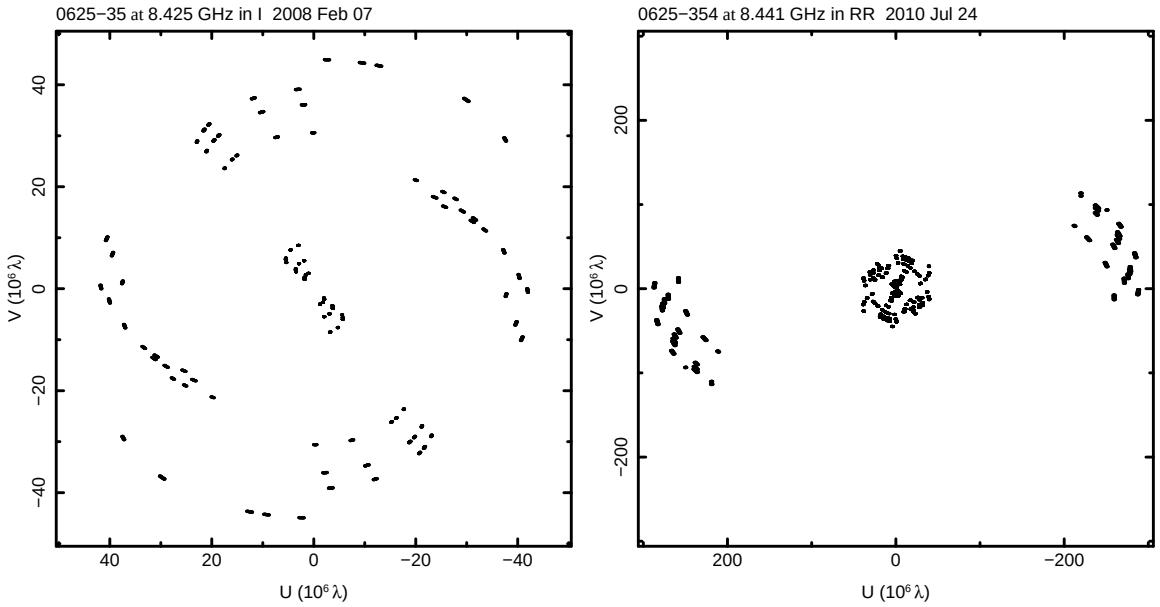

Figure 4.3.: Variations in the (u, v)-coverage between different epochs. The missing long baselines in the epoch on the left results in a bigger beam and a worse resolution in the image compared with the epoch on the right. For the influence of the long baselines also see Fig. 3.10

et al. 1999) is used. The process can be divided into four steps which lead in an iterative process to a final CLEAN-image:

1. The first step is used to define the map and pixel size of the image, the weighting scheme is selected and the data are averaged with a reasonable interval and the corresponding errors are calculated.

2. In the second step, a model consisting of δ-functions is developed with the CLEAN algorithm and the *phase self-calibration*.

3. When a model is developed, an amplitude and phase self-calibration is performed. After this, the data are edited to remove spikes of the residuals followed by starting again at the second step. The second and third step are repeated in decreasing solution intervals until the final image can be created.

4. In the last step a final CLEAN-image is produced.

The initial step of imaging is mainly to choose the settings. The averaging of the data accelerates the calculations and provides a statistical error for the data bins. The error bars of the data after the calibration are very high and due to statistics the error is reduced with binning the data points in certain intervals. The integration time of the bins should be selected within the coherence length of the data. For the TANAMI data

sets, an integration time of 32 s was selected.
The different weighting schemes also influence the imaging process. *Natural weighting* weights the visibilities after their distribution in the (u, v)-plane. This leads to images with higher sensitivity because the shorter baselines with more data points have more weight and the long baselines with less visibilities have less weight. This also increases also the fidelity in the images, since the data are only interpreted according to the particular array parameters. But it also leads to a loss of details of small scale structures because the long baselines have lower weight. The *uniform weighting* leads to better resolution. At *uniform weighting* all data points are weighted inversely to the number of visibilities within a bin, where a bin consists of two pixels in the (u, v)-plane, leading to better resolutions but also increasing the influence of outliers and decreasing the sensitivity since the short baselines with more data points are downweighted in comparison to the few data points of long baselines. For the images in this work the *natural weighting* was selected.
To improve sensitivity for diffuse, extended emission, the imaging can be performed using a Gaussian taper. The taper can be used to down-weight the longer baselines >100 Mλ to only 10% of the usual weight.
The size of the map should be chosen to include all extended emission in the image. Also the size of one pixel has to be chosen, it should have a value so that about five pixel are covered by the minor axis of the synthesized beam. While the mapsize differs for the sources in this work, the cell size for the pixels was set to 0.175 mas in every image.
After these initial settings the data should be examined for bad data points and outliers. This can be done with the RADPLOT function of DIFMAP. This function shows all visibilities as a function of (u, v)-radius. For the TANAMI observation the data quality varies over the epochs. For example, Fig. 4.3 shows the different (u, v)-coverages of two epochs of the same source. The missing long baselines in the epoch on the left reveals, that there will be an image with larger beam, hence no detailed small scale structure will be seen in this image (see Fig. 3.10).
The second step initiates the essential stage of the imaging process. The modelling with δ-functions is based on *difference mapping* with the CLEAN algorithm by Högbom (1974). To find the true intensity distribution in the "dirty" image, the CLEAN algorithm creates δ-peak model components assigning them fractions of the peak flux density. The "dirty" image is the convolution of the brightness distribution with the "dirty" beam of the array, where the "dirty" beam is the synthesized beam created through the reception pattern of the array of telescopes. The CLEAN algorithm builds the model of the source out of δ-point sources. After adding a point source, the model component is subtracted in the dirty map and a new map, called *residual map*, is created. The *residual map* is the "dirty" image with subtracted δ-model components. In this map, again model components are added and their brightness is subtracted in the residual map. The region of the "dirty" map where the CLEAN algorithm should be applied can be chosen with rectangular CLEAN *windows*. The CLEAN algorithm is only applied in the borders of those windows. They should be placed around the brightest areas in the "dirty" image. To

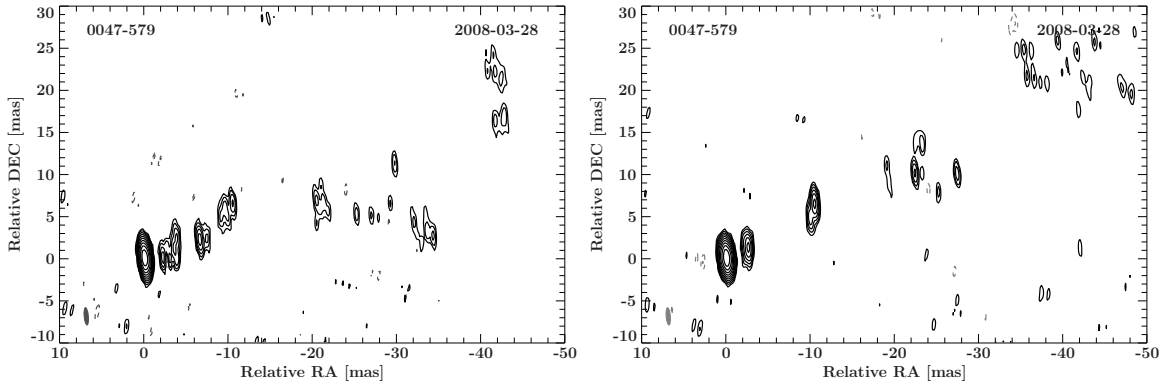

Figure 4.4.: Comparison between a single-epoch CLEAN-Image (left) of an epoch for 0047-579 and the result of *multi-epoch imaging* (right) due to comparison with images and similarity of other epochs.

correct the image for changes concerning the closure phases after each CLEAN-iteration a phase self-calibration step should be used. In some cases the CLEAN algorithm also applies components with negative flux values. This can happen if flux near the borders of the window is used but no component can be placed there subtracting the flux, even if they are physically wrong.

When a satisfying model is obtained with the CLEAN algorithm, an amplitude and phase self-calibration is made, correcting the visibilities to better fit the model. This self-calibration is made in decreasing intervals of the closure relationships (see Sect. 3.4.3). The first interval represents the time interval to the full length of the observation. The consecutive intervals decrease to the time intervals of 180 min, 60 min, 20 min, 5 min, 1 min and finally 0 min, where 0 min corresponds to a fitting of each data point. Between every self-calibration step, the outliers are removed from the RADPLOT showing the residuals of the data points to the model and the CLEAN algorithm is performed within the CLEAN windows.

Because of the changes in the visibilities after every amplitude and phase self-calibration, the data should be continuously saved to have the possibility to undo certain steps or editing. After the CLEANing process of the last amplitude and phase self-calibration, all CLEAN windows are deleted and a high-number iteration of the CLEAN algorithm followed by a phase self-calibration and a repeated high-number iteration of the CLEAN algorithm with a very small gain is applied to the whole image. This leads to the final CLEAN-image. After obtaining the final CLEAN-image, the raw data can be loaded with the model of the final CLEAN-image. Then the RADPLOT can show how the model fits the uncalibrated data or if the model developed deviates too much from the visibilities. Even if the model fits the visibilities well, some features of the model can be wrong because of the gaps in the (u, v)-coverage where no visibilities are available to compare to the model. In this work multiple epochs of the same source where available. Through iterative restarting with the imaging process with different CLEAN windows a model was

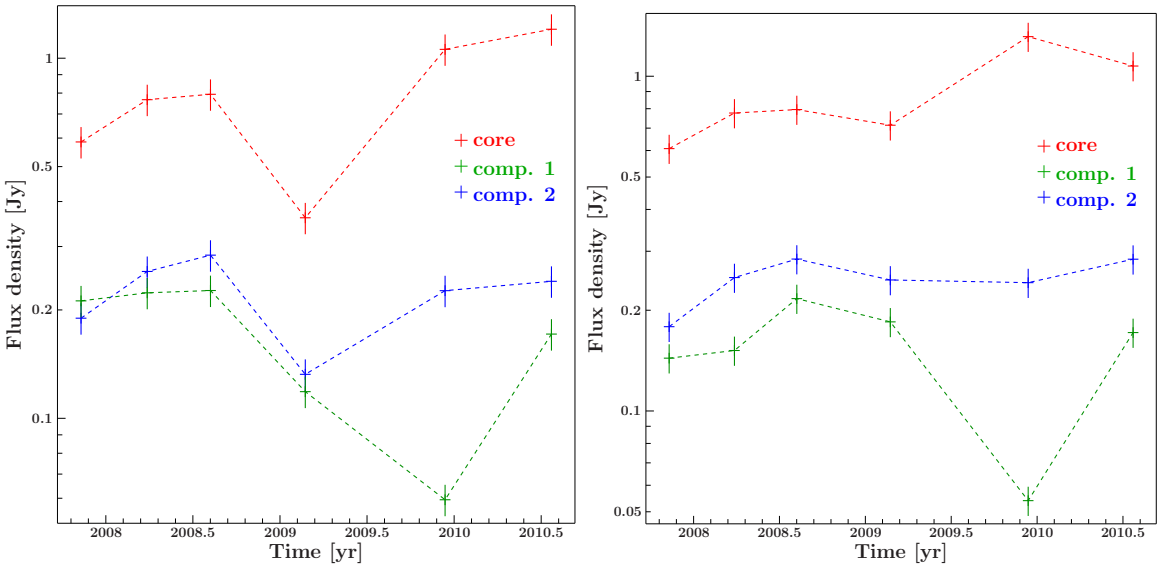

Figure 4.5.: Identification of a calibration problem in the fourth epoch of 2326-477 resulting in too low flux values.

developed which is consistent over the different epochs to remove wrong features, which have resulted from noise or other side-effects. This can lead to images like seen in Fig. 4.4, where the CLEAN image of a single epoch is seen on the left. On the right the image of the iterative re-imaging process (*multi-epoch imaging*) is presented searching for similarities in the other epochs to develop a consistent model, which is only possible having multiple epochs.

4.2.3. Model-fitting

A *model-fitting* of the visibility data with a small number of Gaussian components can also be performed with DIFMAP (Pearson 1995). This can be done with the calibrated data or with the data of the final CLEAN-image. For this work the data of the final CLEAN-image was used because it had a consistent model of δ-peaks and bad data points were removed.
Gaussian components with circular or elliptical shape are used instead of the δ-functions of the CLEAN-algorithm. In this work, only circular components were used. Each component has different parameters: Flux density (Jy), radial distance from the phase centre (mas), position angle (degree) and the radius of the component (mas).
After placing the components in the residual map, the MODELFIT algorithm fits the component parameters after the Levenberg-Marquardt least square fit (Levenberg 1944; Bevington & Robinson 2003). The quality of the fit is represented through the reduced χ^2, aiming for a low value near 1, if possible. Similar to the imaging process, a phase self-calibration can be performed to adjust the phases for a better fit (respecting the

phase-closure relationship; see Sect. 3.4.3), increasing the stability of the fit.
The parameters of the model-fitting process are used for kinematic studies or the calculation of core luminosities and the brightness temperature. With the multi-epoch data in this work, comparisons could be made between the epochs and the evolution of these values. Fig. 4.5 shows two plots of the evolution of the flux density of the components and the core of 2326-477, discussed in detail later. The left image shows a spike of low flux density in Feb. 2009 in all components, which was not expected. The examination of other sources in the same epoch showed the same feature and hence revealed an error in the calibration of this epoch affecting all data sets of this epoch. After a new calibration the data show more reasonable flux density values like presented in the plot on the right side of Fig. 4.5. However the error in the calibration only affected the flux density values. The structure of the source did not change after the re-calibration.

4.2.4. Spectral Index Maps

Based on the assumption of a powerlaw distribution for the synchrotron spectrum in the radio wavelength regime it is possible to calculate the spectral slope (for details see Sect. 3.2) respectively the spectral index α between two frequencies ν and their corresponding flux S. For TANAMI observations these are the frequencies of the K-band (22.3 GHz) and X-band (8.4 GHz).

$$\alpha = \frac{\log(S_{K-band}) - \log(S_{X-band})}{\log(\nu_{K-band}) - \log(\nu_{X-band})} \tag{4.2.1}$$

With this formula the spectral index can be obtained by using the model-fitting components flux density. However in this case the size of the components is not taken into account.
To create spectral index maps like in Fig. 4.6, the spectral index for every pixel is calculated, where the emission is higher than three times the rms noise level. But other influences have to be considered first. The images for the spectral index maps usually have different beams and resolutions and the other problem is the loss of the absolute position through the phase calibration (see Sect. 3.4.3). To be able to compare the images of the frequencies they have to be convolved with the same beam, which is chosen based on the parameters of the largest beam of both maps. Then the image of one frequency can be aligned with the image of the other frequency and the spectral index can be calculated. The left spectral index map in Fig. 4.6 shows a spectral index map obtained in this way. In this case no effort has been made for the correction in the position and both maps were aligned based on the centre of both maps. The core can deviate from this centre, which leads to gradients of the spectral index in the core region (see left image of 4.6).
In order to account for this, a core shift was calculated. In both images Gaussian circular components were fitted to the image like in the model-fitting with the exception

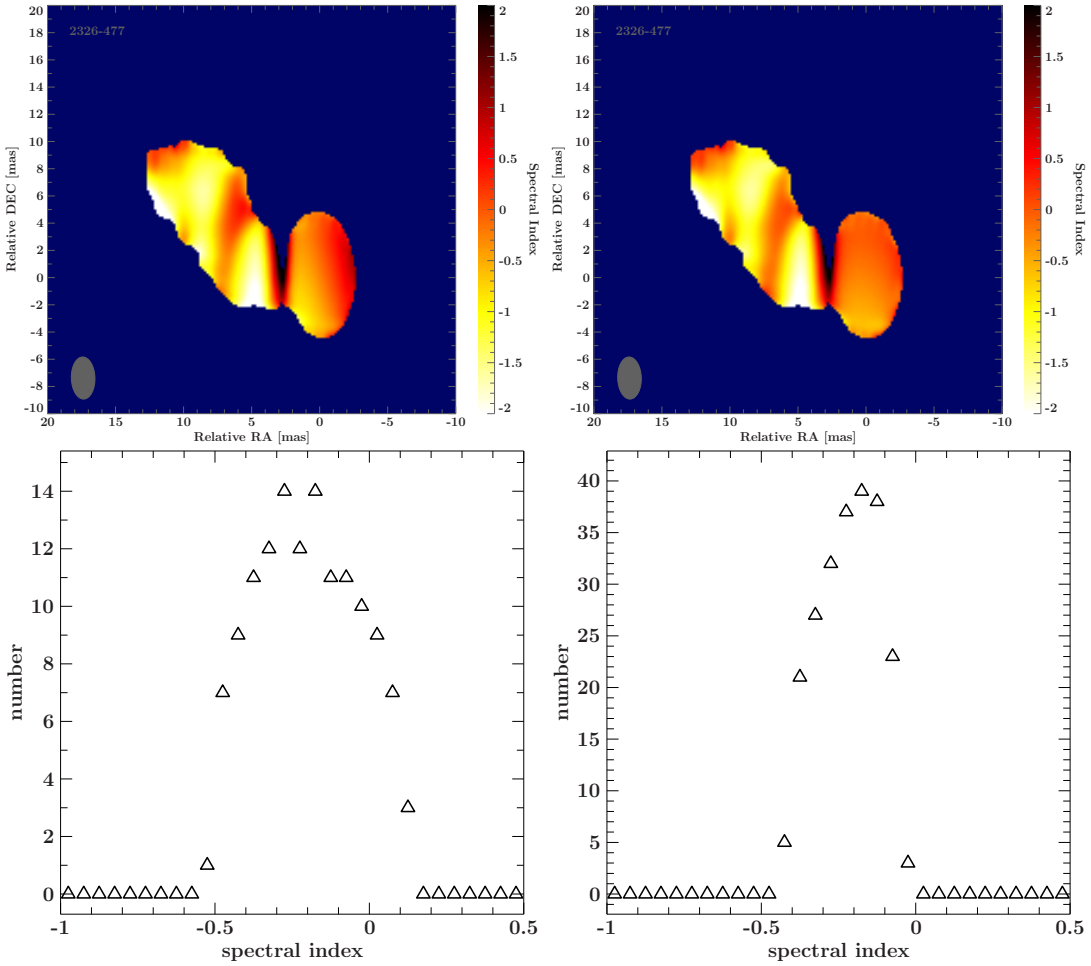

Figure 4.6.: Comparison of spectral index maps (top) without (left) and with (right) shifting the cores. The histograms at the bottom show the distribution of the spectral index in the core region. Without shift the images of different frequencies are aligned with the phase center of both images. With shift the core components are aligned, resulting in a more homogeneous distribution of the spectral index in the core region.

that no self-calibration was used to prevent that the core position is changed through the corrections of the self-calibration. With the positions of both core components the shift is determined and the images are shifted, so that both cores are aligned. Even if these shifts have low values, the influence can be seen in the example in Fig. 4.6 where the right spectral index map shows the shifted version. It is obvious that the core has a more homogeneous distribution of spectral indices than without shifting the maps.
To determine an average spectral index of a core region the spectral index of each pixel was counted within the area corresponding to the common beam adding the size of the larger component of the model-fits and can be presented as a histogram like in Fig. 4.6. The distribution is also represented in the shape of the peak. Broader peaks show a wider range of spectral indices which is a hint that the spectral index is not uniformly distributed. This can be seen also in the example of Fig. 4.6, where the shifted version shows a peak with lower FHWM. In both cases the spectral indices were binned into bins of 0.05-steps in the spectral index.

5. TANAMI observations and results

5.1. The Sample

The sample was selected with the aim to have multiple epochs of the source for imaging, model-fitting and possible kinematic studies. Therefore, all TANAMI sources with at least five calibrated observations before July 2010 were selected. This subsample contains 8 sources of the initial TANAMI sources (see 4.1). An overview over the sample including the coordinates can be found in Tab. 5.1. In this work all object names used apply to the IAU (International Astronomical Union) B1950 source designation. First an overview of each source with previous observations and their structure in comparison with the images of this work is presented. Then the results of the multi-epoch studies and the spectral index maps will be explained.

0047-579

0047-579 is a high redshift quasar ($z = 1.787$), which has been associated with a gamma-loud γ-ray source in the 1FGL catalogue (Abdo et al. 2010a). It has been observed with VLBI before: at 2.3 GHz by Preston et al. (1989) as part of the SHEVE program and at 8.4 GHz by Ojha et al. (2005). While the 2.3 GHz image shows elongated structure in both directions from the core at a position angle of 111°, the 8.4 GHz image shows a second component at a distance of about 20 mas in the west from the core. This direction of the jet is confirmed by first epoch TANAMI images (Ojha et al. 2010). The six images presented in this thesis, starting with an epoch in Nov. 2007 to Jul. 2010 show two prominent components, one near the core and one at a distance of about 10 mas to the west, which are also found in the two K-band epochs (see Fig. 5.1 and Fig. 5.2). More distant emission is found about 20 to 40 mas to the west, but too low surface brightness and too diffuse to consistently model it with a Gaussian component. Hence, no accurate position of this diffuse feature could be determined. However, the tapered images A.1 allows a better imaging of the extended emission.

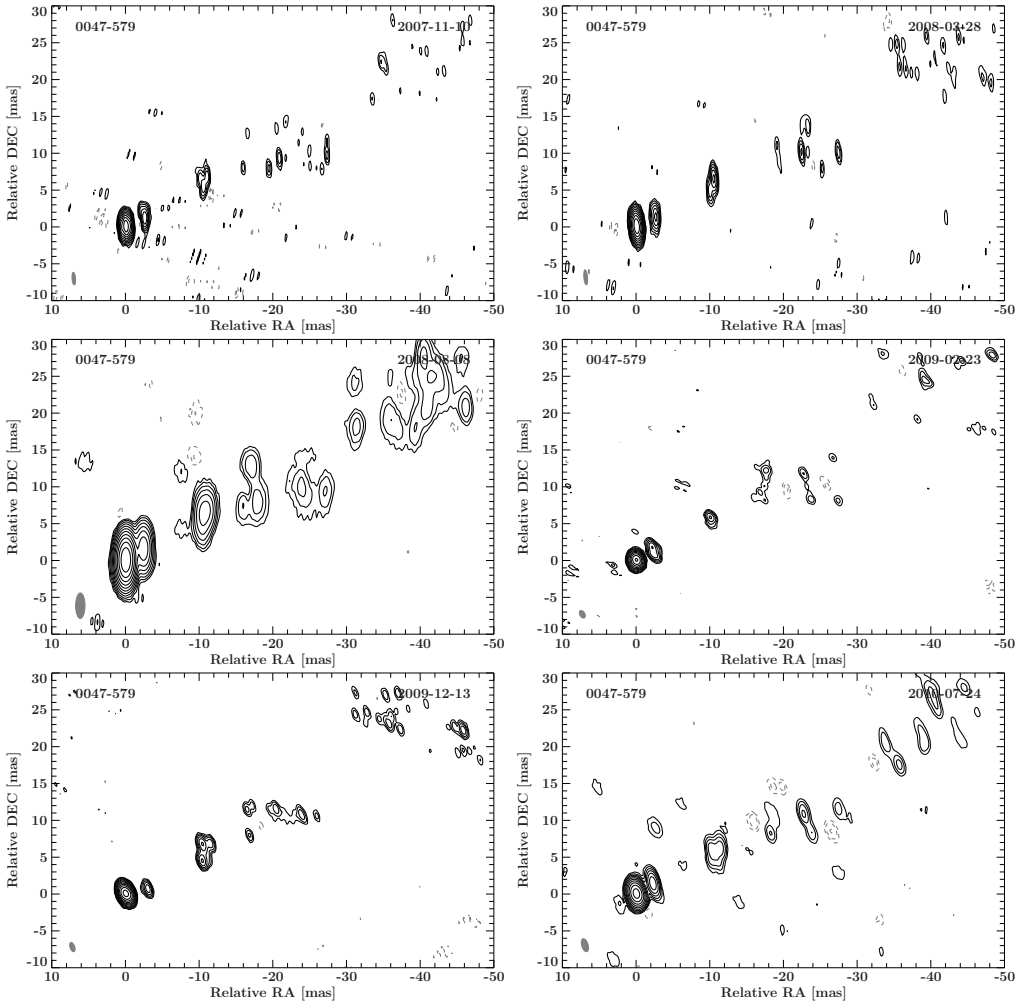

Figure 5.1.: Images of 0047-579 at the X-Band (8.4 GHz). The contour levels are set to the 3σ rms noise and increase logarithmically by a factor of two. For the imaging parameters see Tab. 5.4.

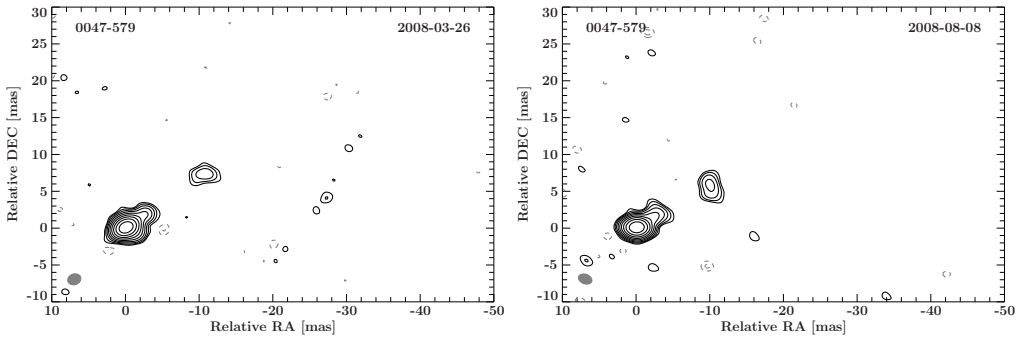

Figure 5.2.: Images of 0047-579 at the K-Band (22.3 GHz). The contour levels are set to the 3σ rms noise and increase logarithmically by a factor of two. For the imaging parameters see Tab. 5.5.

0506-612

0506-612 is a quasar associated with a γ-ray source in the *Fermi* 1FGL catalogue. The images of Ojha et al. (2004) show it as an unresolved point source, while the first epoch TANAMI paper (Ojha et al. 2010) presents a component near the core ($\sim$ 3 mas at a position angle of $\sim$ -50° @land extended emission about 30-80 mas from the core. The images in this work (Fig. 5.3) confirm the component near the core. The extended emission is found at a different position angle ($\sim$ -110°) than the component and is about 50-80 mas away from the core (see Fig. 5.3). In the tapered images (Fig. A.2) the jet structure has a curved shape. In the K-band images only an unresolved point source could be found (see Fig. 5.4) because the component has very low flux (see Tab. A.1) and the long baselines are missing in the K-band observations.

0625-354

0625-354 also known as OH 342 is a source with different classifications and the lowest redshift in this sample (z=0.054594 (Quintana & Ramirez 1995)). It has been detected by *Fermi* (Abdo et al. 2010b) and *ROSAT* (Brinkmann et al. 1994), as well as observed with *BeppoSAX* (Trussoni et al. 1999) and *XMM-Newton* (Gliozzi et al. 2008). The radio images for example of the VLA (Very Large Array)[1] in Fig. 5.5 (archival VLA-data, provided by T. Cheung) suggest a FR I radio galaxy as it was also classified by Ojha et al. (2010) and Venturi et al. (2000), while Wills et al. (2004) suggest a BL Lac classification based on the optical spectrum and the optical image of a point source from Govoni et al. (2000). Gliozzi et al. (2008) present the source as part of a LINER sample because of its low flux. The 2.3 GHz image of Venturi et al. (2000) shows a faint jet in the south-east direction, which is also found in the 8.4 GHz images of this work and the TANAMI paper. In the images in this work a component near the core and a second one at about 5 mas is clearly visible. At about 15 mas, a fainter component can be found (see Fig. 5.6), which can be also seen in the tapered images (Fig. A.3). However the TANAMI observations result in only the one-sided jet, while radio galaxies usually also show the counter-jet. The K-band images indicate the jet in the same direction but no component can be identified in the extended emission (see Fig. 5.7).

1104-445

This source has been observed at 2.3 GHz as part of the SHEVE VLBI program and has a jet in the east-north-east direction (Preston et al. 1989). It was also observed at 4.8 GHz by Shen et al. (1997) and Tingay et al. (2002). Shen et al. (1997) support a curvature from north-east to north at about 1.8 mas, which was not found in the TANAMI

[1] http://www.vla.nrao.edu/

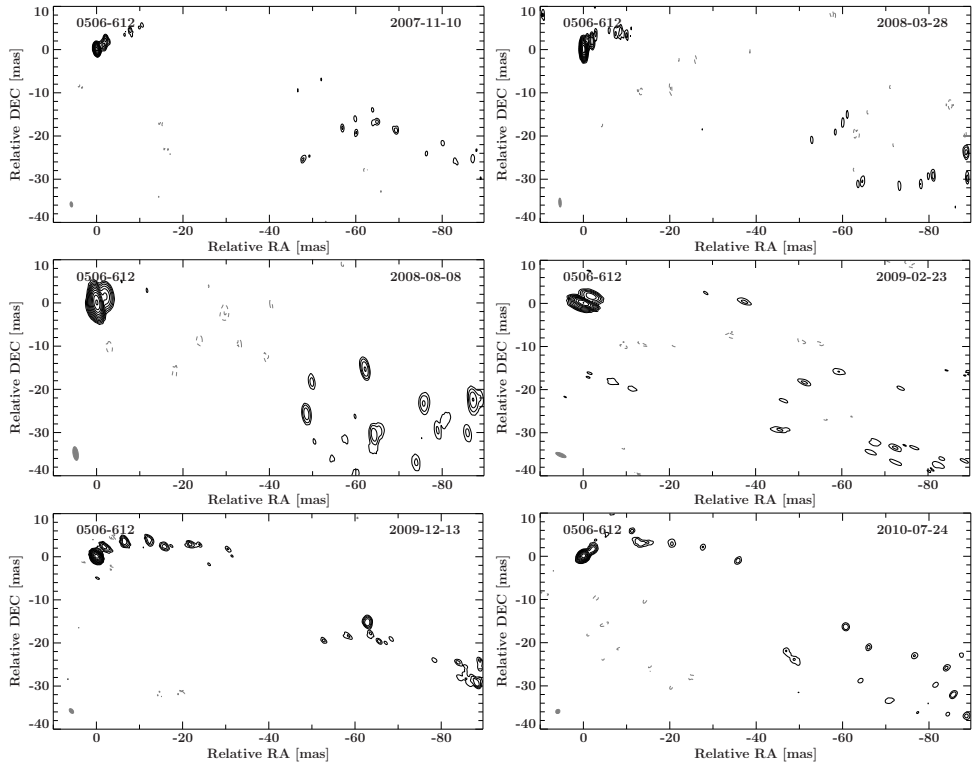

Figure 5.3.: Images of 0506-612 at the X-Band (8.4 GHz). The contour levels are set to the 3σ rms noise and increase logarithmically by a factor of two. For the imaging parameters see Tab. 5.4.

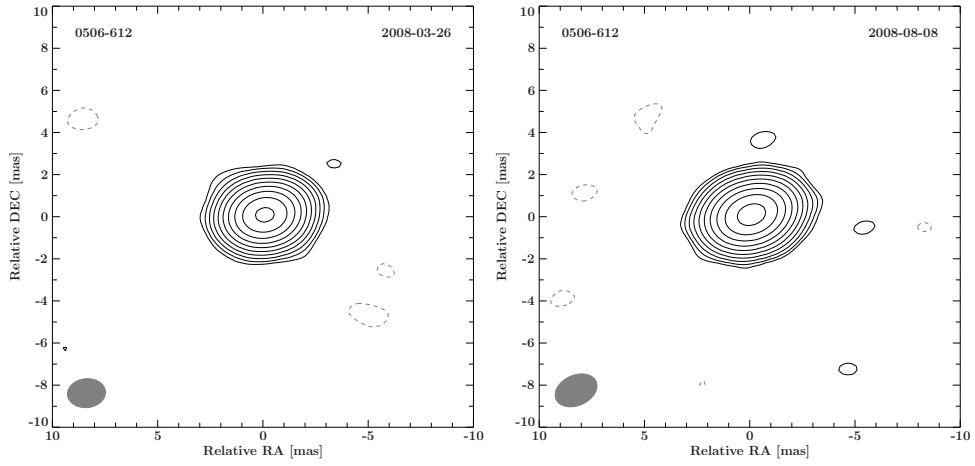

Figure 5.4.: Images of 0506-612 at the K-Band (22.3 GHz). The contour levels are set to the 3σ rms noise and increase logarithmically by a factor of two. For the imaging parameters see Tab. 5.5.

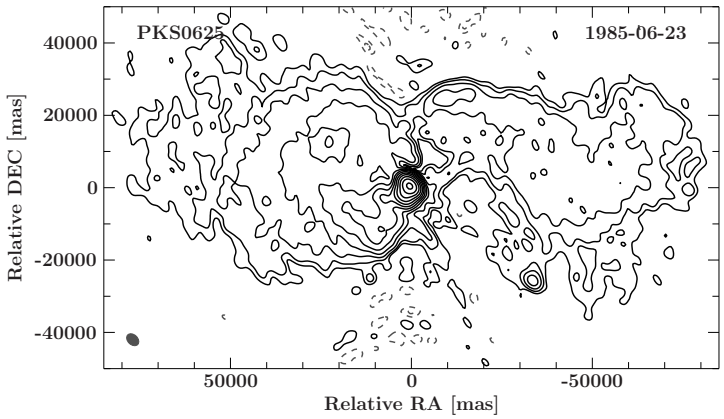

Figure 5.5.: Brightness distribution of 0625-354 observed with the VLA (archival VLA-data, provided by T. Cheung)

observations from the first epoch (Ojha et al. 2010). The images of this work show one component and indications of another component in the north of the first one. The last three epochs also indicate a new component very near the core. The shape of the jet could confirm the suggestion of a curvature in the jet (see Fig. 5.8). Also the K-band images show the component in the north-east of the core (see Fig. 5.9).

1323-526

1323-526 is a γ-ray source detected by *Fermi* (Abdo et al. 2010a) and *EGRET* (Bignall et al. 2008). However, it is still unclassified and no redshift could be determined. McCulloch et al. (2005) observed the source with Ceduna telescope and found intra-day variability in the centimeter-wavelength emission. For the first epoch TANAMI (Ojha et al. 2010) showed a jet in south direction out to 8 mas. In this work (see Fig. 5.10 and Fig. 5.11) the jet is heavily resolved but indicates emission in the direction to the south.

2005-489

PKS 2005-489 is one of the brightest known BL Lac source (Wall et al. 1986; H.E.S.S. Collaboration 2010) at all wavelengths in the Southern Hemisphere and classified as a high-frequency peaked BL Lac (Sambruna et al. 1995). The source was detected at γ-ray energies with *EGRET* (Lin et al. 1999) and *Fermi* (Abdo et al. 2010b). It was one of the bright γ-ray sources in the first three months of operation of *Fermi*. 2005-489 has also been detected in the TeV regime by HESS and was reported to have the softest VHE spectrum ($\Gamma = 4.0$) by Aharonian et al. (2005). After four years of monitoring, the

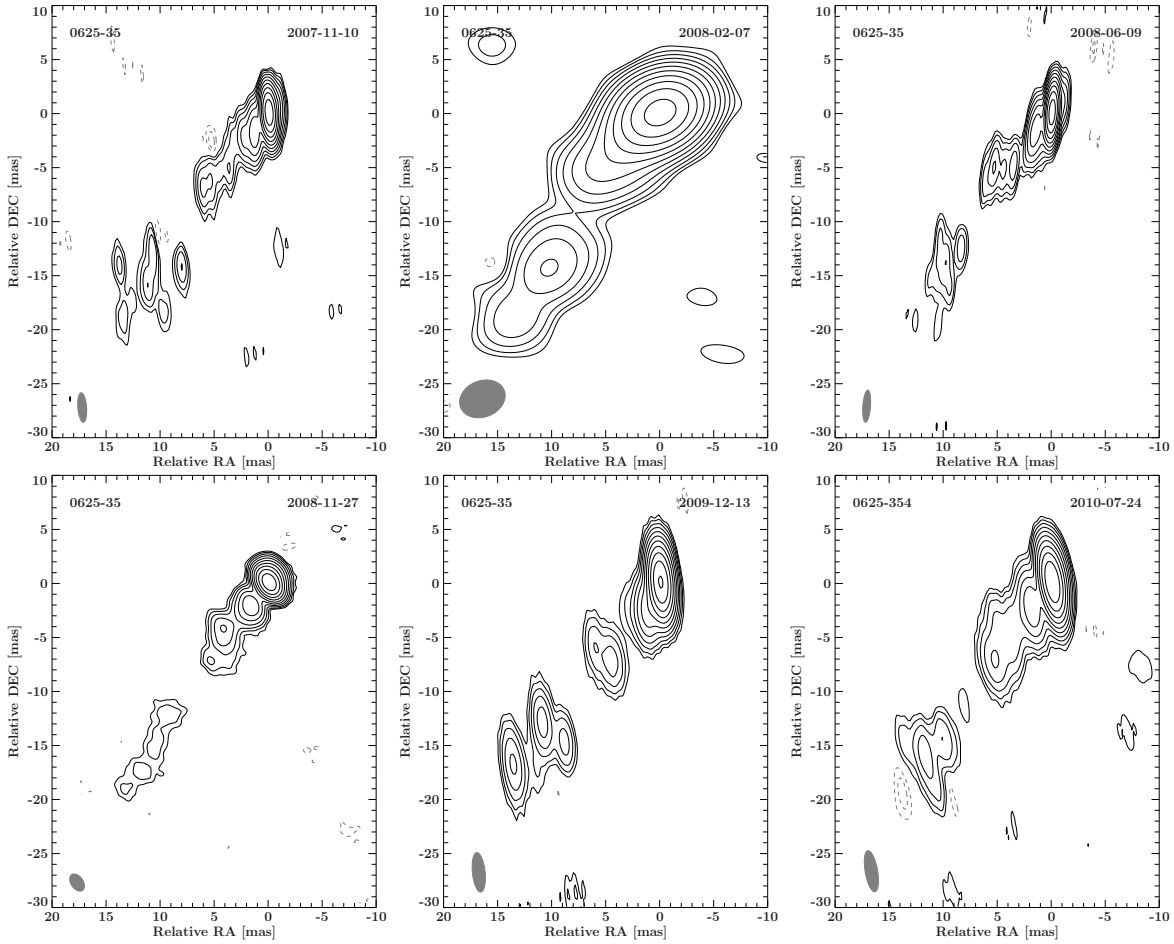

Figure 5.6.: Images of 0625-354 at the X-Band (8.4 GHz). The contour levels are set to the 3σ rms noise and increase logarithmically by a factor of two. For the imaging parameters see Tab. 5.4.

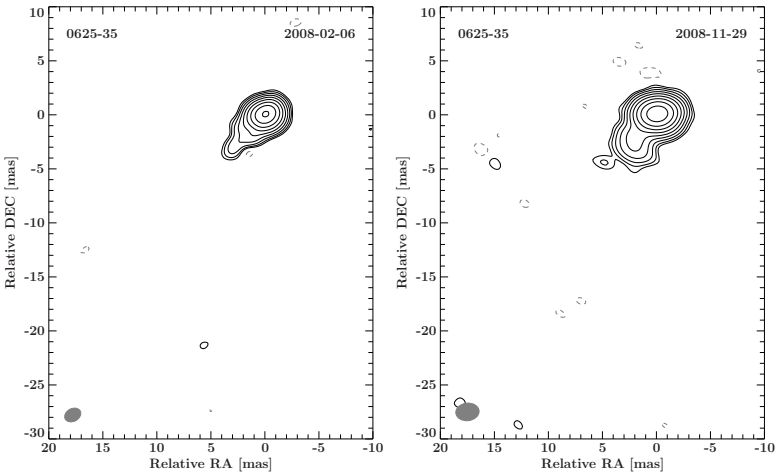

Figure 5.7.: Images of 0625-354 at the K-Band (22.3 GHz). The contour levels are set to the 3σ rms noise and increase logarithmically by a factor of two. For the imaging parameters see Tab. 5.5.

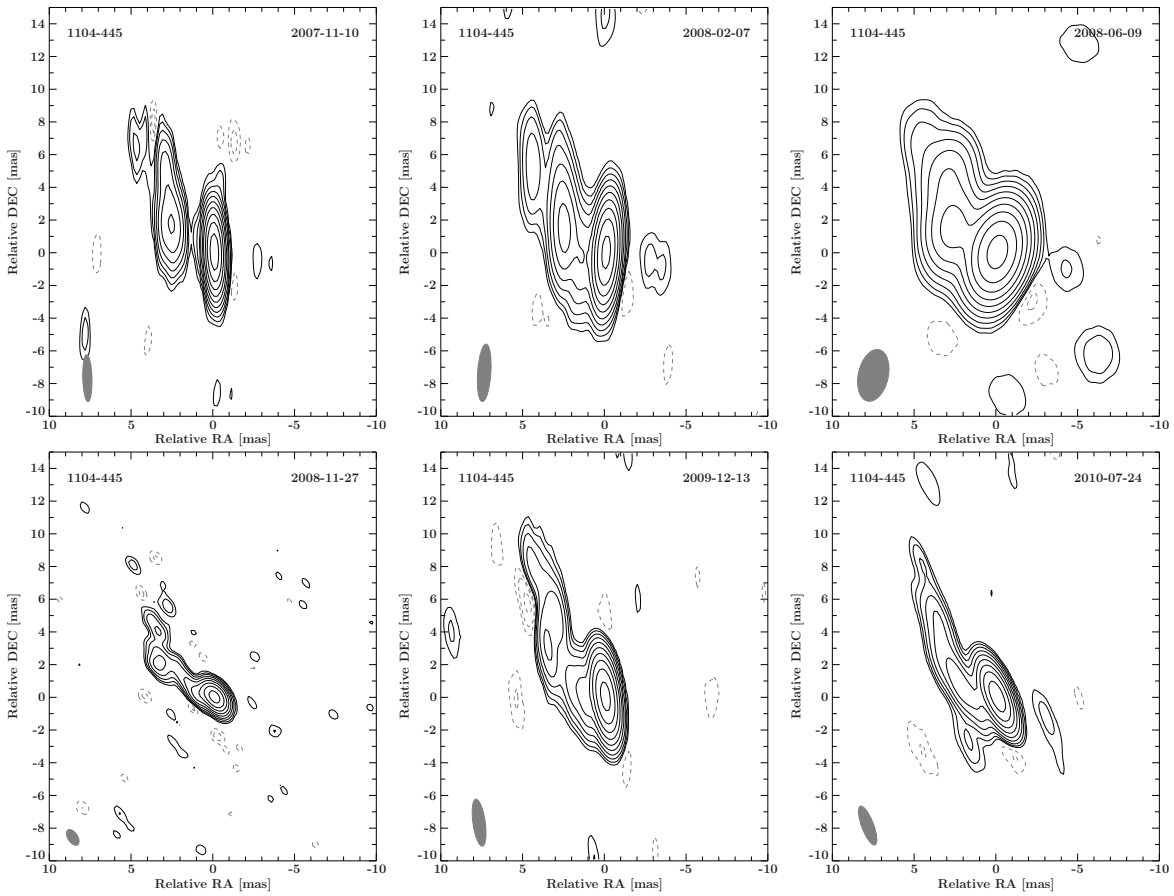

Figure 5.8.: Images of 1104-445 at the X-Band (8.4 GHz). The contour levels are set to the 3σ rms noise and increase logarithmically by a factor of two. For the imaging parameters see Tab. 5.4.

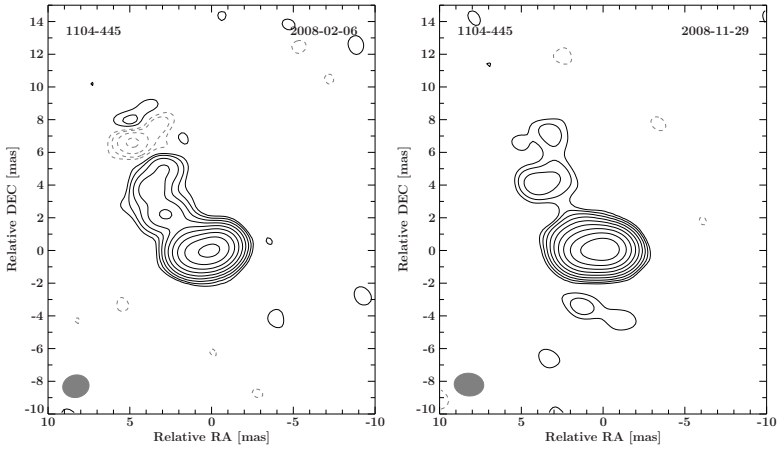

Figure 5.9.: Images of 1104-445 at the K-Band (22.3 GHz). The contour levels are set to the 3σ rms noise and increase logarithmically by a factor of two. For the imaging parameters see Tab. 5.5.

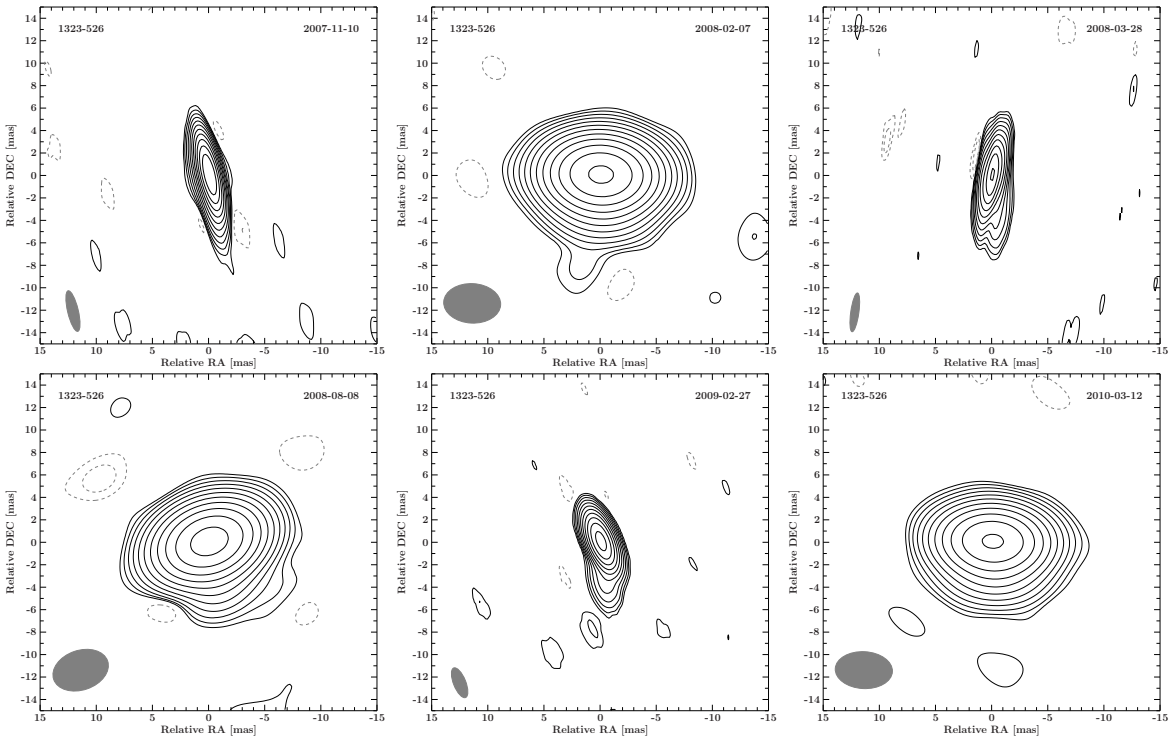

Figure 5.10.: Images of 1323-526 at the X-Band (8.4 GHz). The contour levels are set to the 3σ rms noise and increase logarithmically by a factor of two. For the imaging parameters see Tab. 5.4.

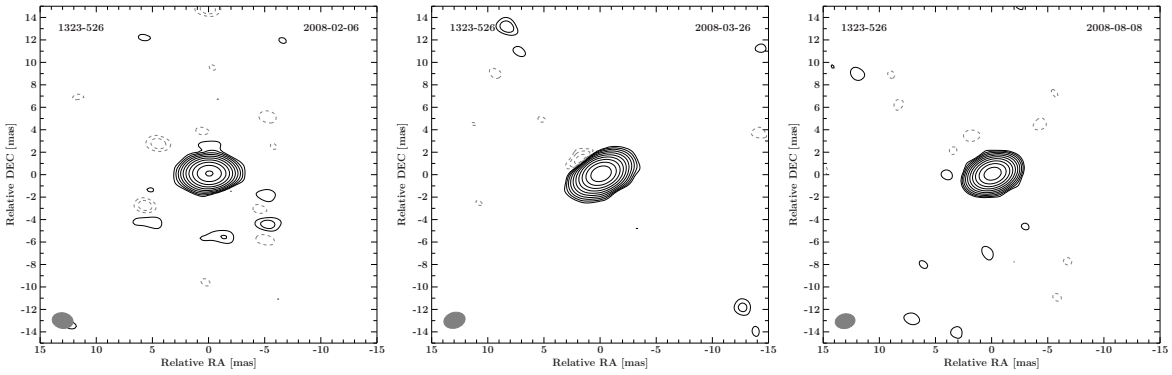

Figure 5.11.: Images of 1323-526 at the K-Band (22.3 GHz). The contour levels are set to the 3σ rms noise and increase logarithmically by a factor of two. For the imaging parameters see Tab. 5.5.

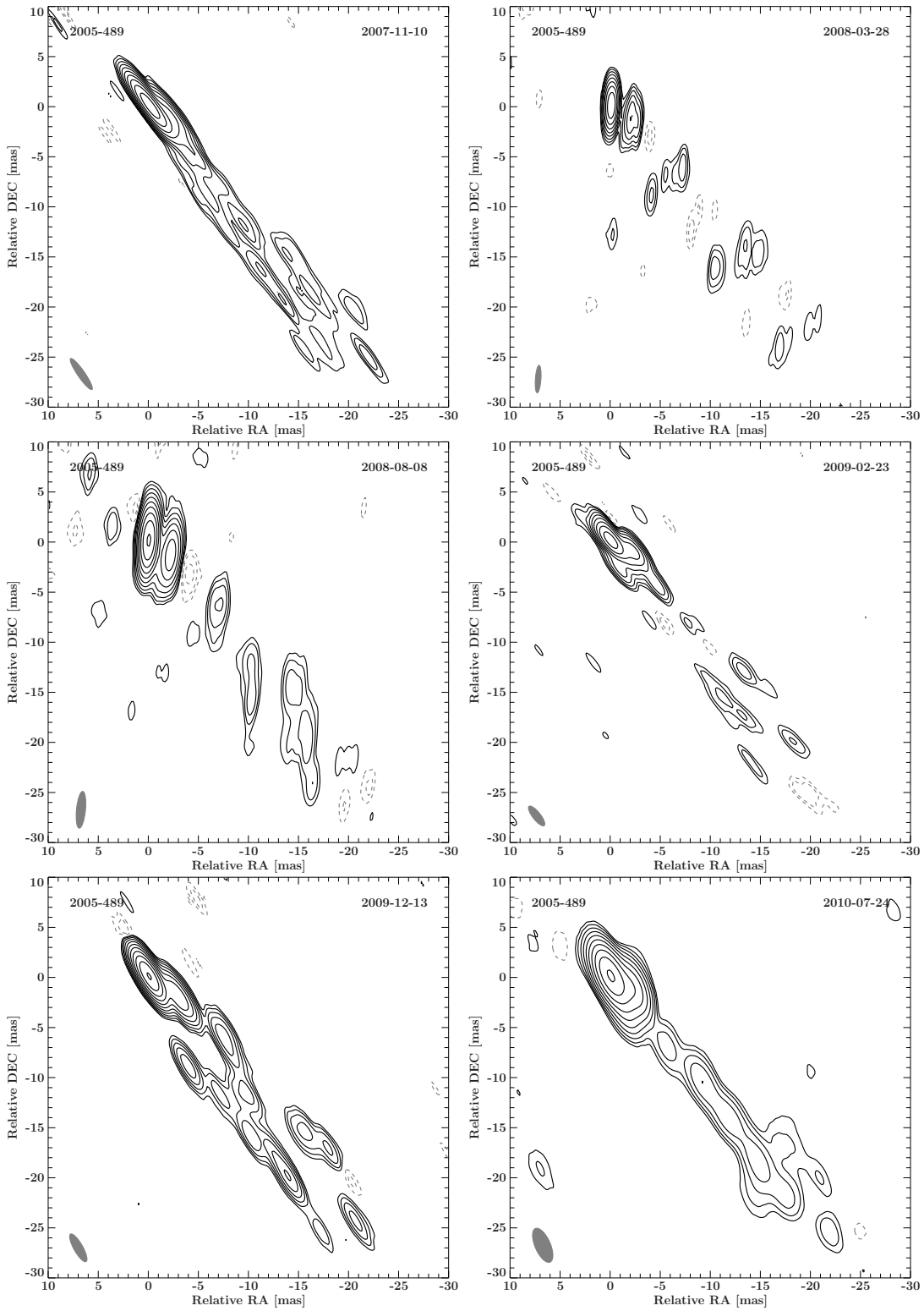

Figure 5.12.: Images of 2005-489 at the X-Band (8.4 GHz). The contour levels are set to the 3σ rms noise and increase logarithmically by a factor of two. For the imaging parameters see Tab. 5.4.

Table 5.1.: Source list

Source[a]	Name[b]	R.A.[c] (J2000.0)	Dec.[c] (J2000.0)	ID[d]	Redshift z	Magnitude V[e]	LAT[f]
0047-579	PKS B0047-579	$00^h49^m59^s$	-57°38'27"	Q	1.797[1]	18.50	Y
0506-612	PKS B0506-612	$05^h06^m43^s$	-61°09'40"	Q	1.093[2]	16.85	Y
0625-354	PKS B0625-354	$06^h27^m06^s$	-35°29'15"	G	0.054594[3]	16.50	Y
1104-445	PKS B1104-445	$11^h07^m08^s$	-44°49'07"	Q	1.598[1]	18.20	N
1323-526	PMN J1326-5256	$13^h46^m48^s$	-52°56'22"	U	-	-	Y
2005-489	PKS B2005-489	$20^h09^m25^s$	-48°49'53"	B	0.0710[4]	15.30	Y
2052-474	PKS B2052-474	$20^h56^m16^s$	-47°14'47"	Q	1.489[5]	19.10	Y
2326-477	PKS B2326-477	$23^h29^m17^s$	-47°30'19"	Q	1.30417[6]	16.79	C

[a] IAU B1950 source designation
[b] Name in NED (NASA/IPAC Extragalactic Database), preferring the Parkes Radio Catalogue in B1950 coordinates
[c] Right ascension and declination (J2000.0)
[d] Identification to the optical counterpart after Véron-Cetty & Véron (2006): G - galaxy, Q - quasar, B - blazar, U - unclassified
[e] Optical magnitude
[f] Associated with Fermi/LAT detections of the 1FGL catalogue (Abdo et al. 2010a): Y - detected, N - not detected, C - candidate after Böck (2012)
References: [1] Peterson et al. (1976), [2] Hewitt & Burbidge (1989), [3] Quintana & Ramirez (1995), [4] Falomo et al. (1987), [5] Jauncey et al. (1984), [6] Jones et al. (2009)

H.E.S.S. Collaboration (2010) reported a soft VHE spectrum of $\Gamma = 3.20$. The source was also studied in the X-ray-band with observations of *BeppoSAX* and *RossiXTE* by Tagliaferri et al. (2001). In the radio, the observations of Shen et al. (1998) at 4.8 GHz revealed no jet structure, while the observations of the LBA with associated telescopes from Ojha et al. (2005) show a component in south-west direction from the core at about 3 mas. The TANAMI first epoch images (Ojha et al. 2010) show a jet with low surface brightness and a wide opening angle in south-west direction. The images in this work in Fig. 5.12 show a jet with a less wide opening angle over all six epochs, where in most epochs a component near the core at about 2 mas is visible. At distances beyond ∼5 mas, the jet has highly resolved diffuse emission (see Fig. 5.12), which can hardly modelled by Gaussian components and therefore it is difficult to track and identify individual features. However in the tapered images the extended emission is clearly visible (Fig. A.4). The K-band images (see Fig. 5.13 show the component near the core but the distant jet structure is not visible.

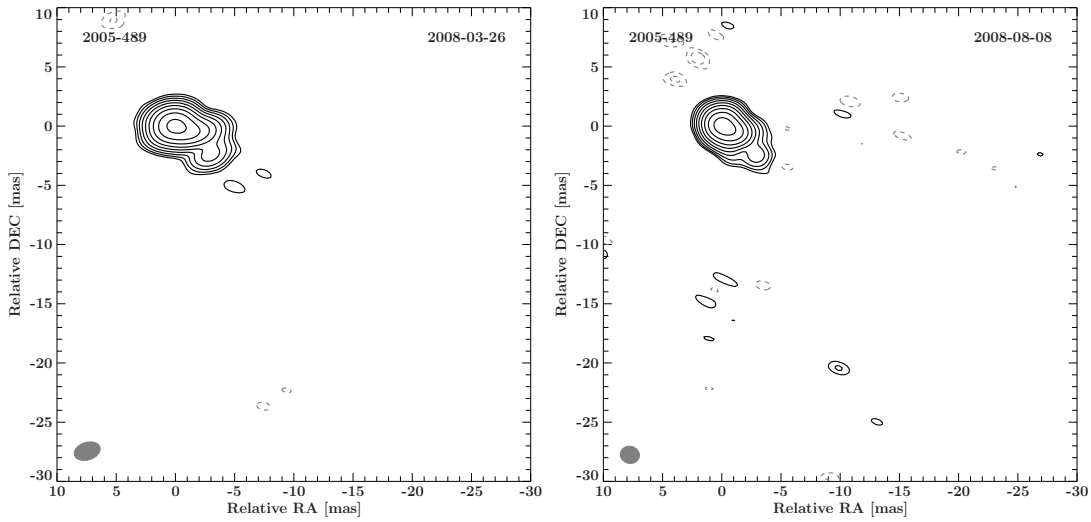

Figure 5.13.: Images of 2005-489 at the K-Band (22.3 GHz). The contour levels are set to the 3σ rms noise and increase logarithmically by a factor of two. For the imaging parameters see Tab. 5.5.

2052-474

2052-474 was detected by EGRET (Hartman et al. 1999) and associated with a *Fermi* source (Abdo et al. 2010a). Marshall et al. (2005) observed the source with *Chandra* and found no extended X-ray emission on scales larger than 1 arcsec. The radio images from Ojha et al. (2004) show a unresolved source at sub-parsec-scales. The TANAMI paper of the first epoch (Ojha et al. 2010) show a weak jet in the west direction, but the images presented in this work are not confirming this jet. Fig. 5.14 and Fig. 5.15 show only a core. The high noise in the images does not allow to check whether there is an extended structure, but the weak features found in the imaging process where in every epoch in different directions leading to the assumption to be only artefacts of the noise.

2326-477

This quasar at redshift (z=1.30417) is a candidate for an association with a *Fermi* source by Böck (2012). It was also observed with SHEVE at 2.3 GHz (Preston et al. 1989), where the image shows an unresolved point source. Also Scott et al. (2004) with VSOP found a compact unresolved core at 4.8 GHz. Tingay et al. (2003) found a higher mean flux density with ATCA and moderate variability. The first epoch image of TANAMI (Ojha et al. 2010) shows two jet components besides the core: one in east direction at about 6 mas and another one in north-east direction at about 10 mas. The images in this work confirm these two components and show a bent jet structure with substantial curvature northward behind the east component at 6 mas and indications of a curving

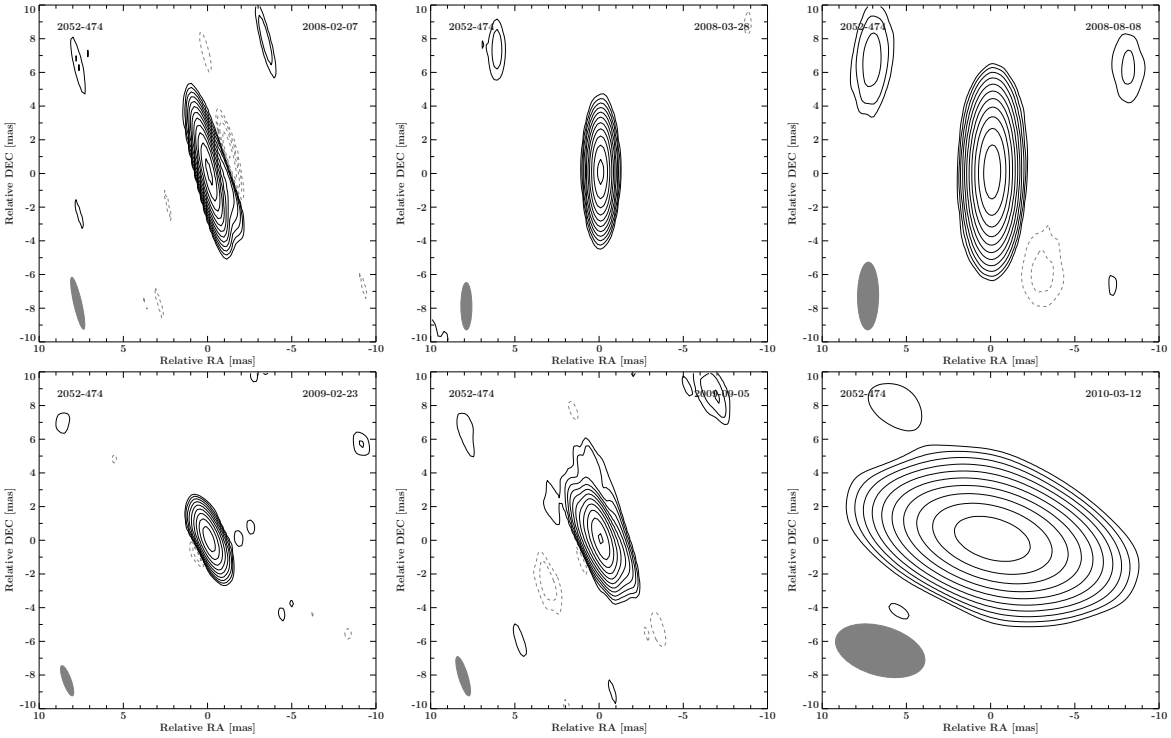

Figure 5.14.: Images of 2052-474 at the X-Band (8.4 GHz). The contour levels are set to the 3σ rms noise and increase logarithmically by a factor of two. For the imaging parameters see Tab. 5.4.

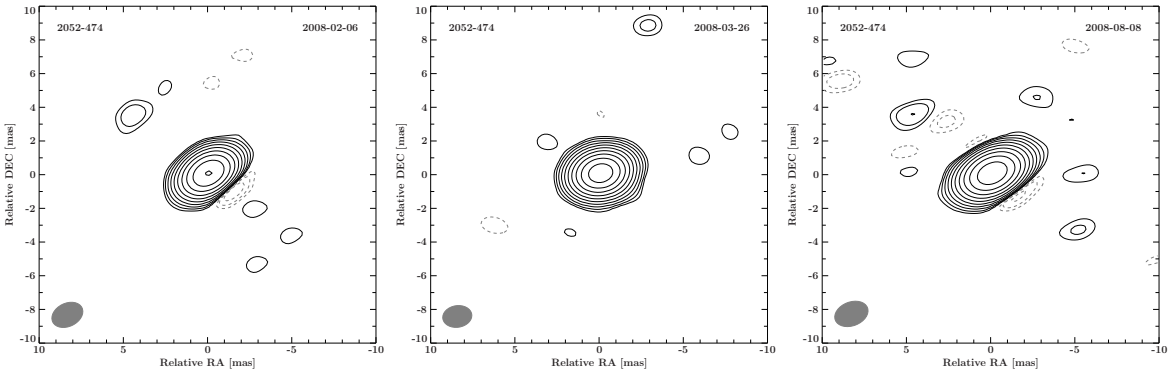

Figure 5.15.: Images of 2052-474 at the K-Band (22.3 GHz). The contour levels are set to the 3σ rms noise and increase logarithmically by a factor of two. For the imaging parameters see Tab. 5.5.

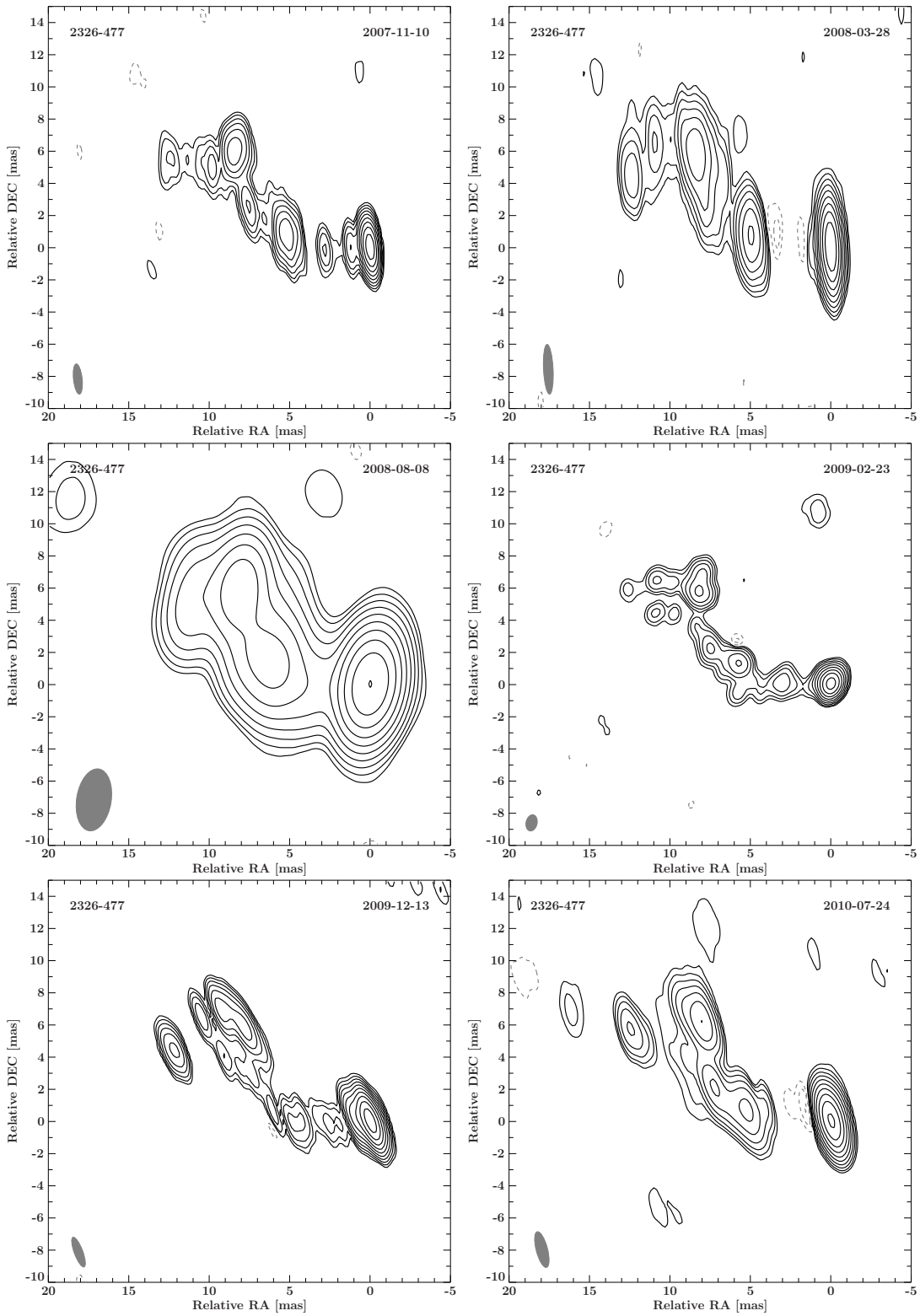

Figure 5.16.: Images of 2326-477 at the X-Band (8.4 GHz). The contour levels are set to the 3σ rms noise and increase logarithmically by a factor of two. For the imaging parameters see Tab. 5.4.

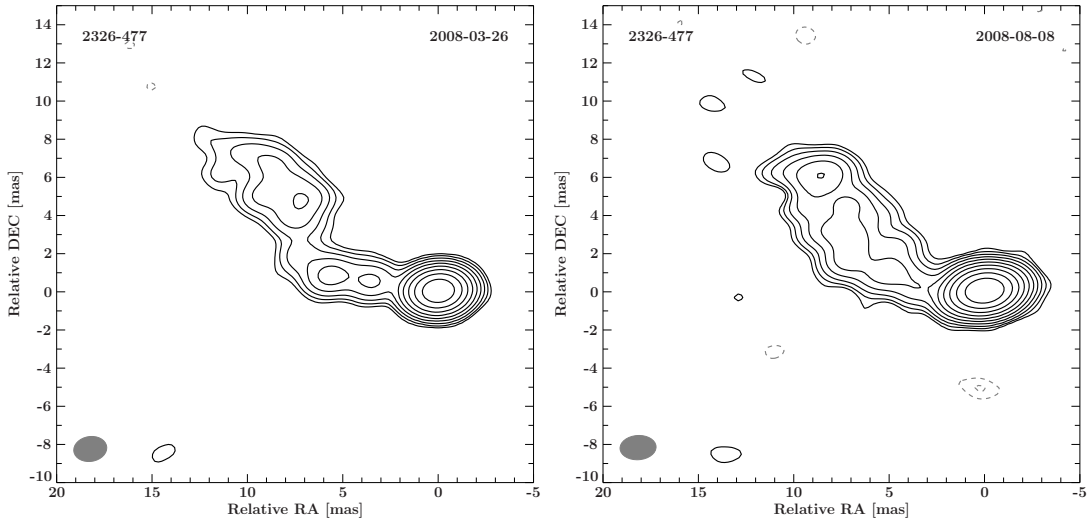

Figure 5.17.: Images of 2326-477 at the K-Band (22.3 GHz). The contour levels are set to the 3σ rms noise and increase logarithmically by a factor of two. For the imaging parameters see Tab. 5.5.

back in east direction again after the second component (see Fig. 5.16). This shape can also be found in the K-band images (see Fig. 5.17).

Table 5.2.: List of all observation epochs

Epoch (date)	Epoch (name)	Participating Telescopes	Sources of Sample observed	Frequency band
Nov. 10, 2007	V252A	Parkes, ATCA, Mopra, Hobart, Ceduna, Hartebeesthoek	0047-579, 0506-612, 0625-354, 1104-445, 1323-526, 2005-489, 2326-477	X-band
Feb. 6, 2008	V252B	Parkes, ATCA, Mopra, Hobart, Ceduna, DSS43	0625-354, 1104-445, 1323-526, 2052-474	K-band
Feb. 7, 2008	V252C	Parkes, ATCA, Mopra, Hobart, Ceduna, Hartesbeesthoek, DSS43	0625-354, 1104-445, 1323-526, 2052-474	X-band
Mar. 26, 2008	V252D	Parkes, ATCA, Mopra, Hobart, Ceduna, DSS43	0047-579, 0506-612, 1323-526, 2005-489, 2052-474, 2326-477	K-band
Mar. 28, 2008	V252E	Parkes, ATCA, Mopra, Hobart, Ceduna, Hartebeesthoek, DSS43	0047-579, 0506-612, 1323-526, 2005-489, 2052-474, 2326-477	X-band
Jun. 9, 2008	V252F	Parkes, ATCA, Mopra, Hobart, Ceduna, Hartebeesthoek	0625-354, 1104-445	X-band
Aug. 8, 2008	V252G	Parkes, ATCA, Mopra, Hobart, Ceduna, Hartebeesthoek	0047-579, 0506-612, 1323-526, 2005-489, 2052-474, 2326-477	K-band
Aug. 8, 2008	V252H	Parkes, ATCA, Mopra, Hobart, Ceduna, Hartebesthoek, DSS45	0047-579, 0506-612, 1323-526, 2005-489, 2052-474, 2326-477	X-band
Nov. 27, 2008	V252I	Parkes, ATCA, Mopra, Hobart, Ceduna, O'Higgins, Tigo, DSS43	0625-354, 1104-445	X-band
Nov. 29, 2008	V252J	Parkes, ATCA, Mopra, Hobart, Ceduna, DSS43	0625-354, 1104-445	K-band
Feb. 23, 2009	V252K	Parkes, ATCA, Mopra, Hobart, Ceduna, DSS43, DSS45, O'Higgins, Tigo	0047-579, 0506-612, 2005-489, 2052-474, 2326-477	X-band
Feb. 27, 2009	V252L	Parkes, ATCA, Mopra, Hobart, Ceduna, DSS45, O'Higgins, Tigo	1323-526	X-band
Sep. 6, 2009	V252N	Parkes, ATCA, Mopra, Hobart, Ceduna, DSS43, Tigo	2052-474	X-band
Dec. 14, 2009	V252O	Parkes, ATCA, Mopra, Hobart, Ceduna, Tigo	0047-579, 0506-612, 0625-354, 1104-445, 2005-489, 2326-477	X-band
Mar. 12, 2010	V252P	Parkes, ATCA, Mopra, Hobart, Ceduna, DSS43	1323-526, 2052-474	X-band
Jul. 24, 2010	V252S	Parkes, ATCA, Mopra, Hobart, Ceduna, DSS43, Tigo	0047-579, 0506-612, 0625-354, 1104-445, 2005-489, 2326-477	X-band

X-Band corresponds to 8.4 GHz
K-Band corresponds to 22.3 GHz

5.2. Imaging Results

The results of imaging the datasets of the sample are listed in Tab. 5.4 for the X-band observations and in Tab. 5.5 for the K-band. For the values of the brightness temperature T_b and the core luminosity a Gaussian circular component was fitted to the uv-data for each observation. The model-fitting parameters of the components can be found in Tab. A.1, Tab. A.2, Tab. A.3 and Tab. A.4. The sizes of the component have a limit for a minimum size θ_{lim} calculated after Kovalev et al. (2005) with the mean of the major axis θ_{maj} and minor axis θ_{min} FWHMs and the signal-to-noise ratio using the following equation:

$$\theta_{lim} = \theta_{mean}\sqrt{\frac{4\ln 2}{\pi}\ln\frac{\mathrm{SNR}}{\mathrm{SNR}-1}} \tag{5.2.1}$$

For fits with smaller components $\theta_{fit} < \theta_{lim}$ the size was adjusted to the resolution minimum. This limit was used for all model components not only for the core components, but in nearly every model the component sizes were larger than the limit.

Brightness temperatures

With the core components the brightness temperature was calculated using the formula (Kovalev et al. 2005):

$$T_b = \frac{2\ln 2}{\pi k_B}\frac{S_{core}\lambda^2(1+z)}{\theta_{maj}\theta_{min}} \tag{5.2.2}$$

with k_B the Boltzmann-constant, S_{core} the core flux, λ the wavelength of the observation and z the redshift.
Considering the *inverse Compton effect* where the photons gain energy through collision with energetic particles, electrons can be cooled down through the losses of the collisions, called Compton catastrophe. The Compton catastrophe is dependent of the frequency and the energy distribution. After Kellermann & Pauliny-Toth (1969) this results in a limit for the brightness temperature of about $\sim 10^{12}$ K. Readhead (1994) derived an equipartition limit for the brightness temperature T_b of $\sim 5 \times 10^{11}$ K, where most radio sources in his studies showed a cut-off. This equipartition limit also is significantly lower than the limit predicted for the inverse Compton catastrophe.
The values in Tab. 5.4 show values between 10^{10} - 10^{12} K. The sources with low redshift (0625-354, 2005-489) and 1323-526 with exception of the first epoch have the lower brightness temperatures at about 10^{10} K, while the sources with high redshift reach values between 10^{11} - 10^{12} K. All values except the first three epochs of 2052-474, the first epoch of 0506-612 and the first epoch of 1323-526 are below the limit of 10^{12} K determined by Kellermann & Pauliny-Toth (1969). Comparing the values with the first epoch paper of TANAMI (Ojha et al. 2010) all of the values in this work are similar to the published brightness temperatures, which can be also seen in the diagram in Fig.

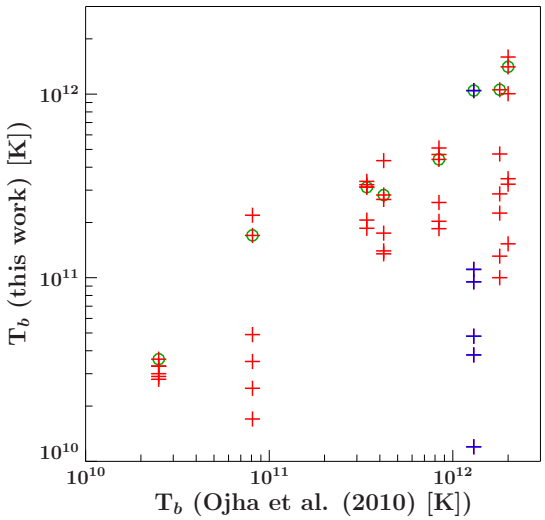

Figure 5.18.: Comparison of the brightness temperatures T_b with the first epoch TANAMI paper by Ojha et al. (2010), where the green circle values correspond to the first epoch observations of this work.
The blue points correspond to the values of 1323-526, where no redshift is known and $z = 0$ was used.

5.18 (the data points with green circles correspond to the same epoch). In the same paper the BL Lacs and galaxies were the objects with the lowest brightness temperature. This is confirmed in this work, but only one BL Lac (2005-489) and one galaxy (0625-354) are part of the sample.
The values of the K-band images seen in Tab. 5.5 are all about one magnitude lower than the corresponding values of the X-band observation. They are all between 10^8 - 10^{11} K and are below the equipartition value of 10^{11} K (Readhead 1994) with the exception of two values of 2052-474 going to 10^{11} K. Also in the K-band the two sources 0625-354 and 2005-489 (lowest redshift and BL Lac/galaxy) are the objects with the lowest brightness temperatures at about 10^8 K, while the rest ranges between 10^9 - 10^{11} K. The difference between X- and K-band can be explained with the different frequencies and flux densities (see eq. 5.2.2). To compare the X-band and the K-band brightness temperatures, the values of T_b, were plotted in the diagram on the left of Fig. 5.19. However the values are dependent (see Eq. 5.2.2) on the spectral index and the frequency. In the right diagram T_b/λ^2 of X- and K-band are plotted, where the K-band values are corrected with the spectral index calculated from the model core components. With the correction of the K-band flux density, a line through the origin is expected. Considering a scattering through various errors and different component sizes (see Eq. 5.2.2), the diagram with corrected K-band values deviates less than without considering the spectral index.
Considering the temporal evolution of these values it is obvious that the values strongly dependent on the uv-coverage. The epochs with missing long baselines, identifiable

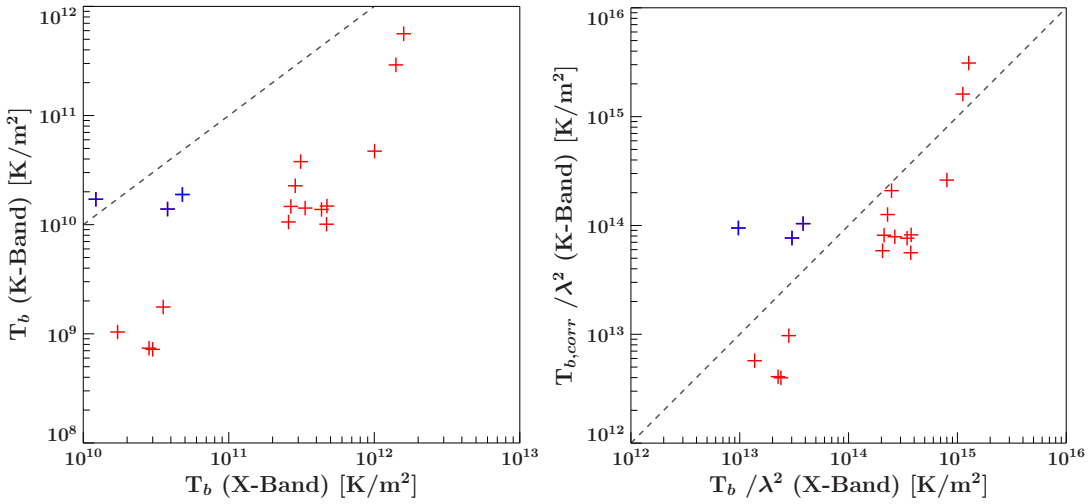

Figure 5.19.: Comparison of the brightness temperatures T_b of the K-band and the X-band: on the left: T_b of X- and K-band
On the right: T_b/λ^2 of X- and K-band, where the K-band values are corrected with the spectral index, calculated from the core components seen in Tab. A.1 - A.4.
The blue points correspond to the values of 1323-526, where no redshift is known and $z = 0$ was used.

through the large beam sizes in Tab. 5.4 or the corresponding images, show deviating brightness temperatures and differ from the values of other epochs: for example the third epoch of 0047-579 and 1104-445 show this. But the brightness temperature also depends on the size of the fitted core component. Smaller components lead to higher brightness temperatures. This can be seen also in equation eq. 5.2.2.

Luminosities

The luminosity values are in the range 10^{24} - 10^{28} W Hz^{-1} for both X-band (Tab. 5.4) and K-band (Tab. 5.5). Also here a difference can be seen between the sources with high redshift in comparison with the ones with low redshift. The low redshift sources (0625-354 and 2005-489) have luminosities of about 10^{24} W Hz^{-1}, while the other are between 10^{27} - 10^{28} W Hz^{-1}. This is expected because of the luminosity-distance function $L = 4\pi S d_{lum}^2$ with a quadratic distance d_{lum} dependency and flux density limited sample.
In comparison with the values for the total luminosity of the TANAMI paper (Ojha et al. 2010) the X-band values differ less than 5% with exception of 2326-477 deviating about 9%. But the magnitudes are consistent in every observation. Ojha et al. (2010) also found that TANAMI galaxies have lower luminosities and quasars are all above 10^{26} W Hz^{-1}, which is consistent with the values of 0625-354 in this work having the weakest

Table 5.3.: Distances and scales of the sources

Source	z	Luminsotiy Distance (Mpc)	Angular Diameter Distance (Mpc)	Scale (pc) for 1 mas
0047-579	1.797	13401	1713.0	8.30
0506-612	1.093	7212	1646.3	7.98
0625-354	0.054594	236	212.2	1.03
1104-445	1.598	11596	1718.0	8.33
1323-526	-	-	-	-
2005-489	0.071	306	266.8	1.29
2052-474	1.489	10606	1712.0	8.30
2326-477	1.30417	8987	1692.7	8.21

Cosmology: $H_0 = 73$ km s^{-1} Mpc^{-1}, $\Omega_m = 0.27$, $\Omega_\Lambda = 0.73$

luminosity, while all sources classified as quasars have luminosities above 10^{27} W Hz^{-1}. At 2005-489 the first epoch has a low core luminosity which is a result of the modelling with a component close to the core, which takes some flux of the core. At 2052-474 and 2326-477 an increase in the core luminosity is noticeable in the last two epochs. This follows the core flux and is discussed in Sect. 5.3.
The K-band values in Tab. 5.5 are consistent with the X-band values showing the same magnitudes and being slightly lower because of the lower fluxes. Also these values show 0625-354 to exhibit the weakest luminosities and the quasars all above 10^{27} W Hz^{-1}.

Morphology

In the sample of this work all sources except 2052-474 show a jet structure to one side after the classification scheme adapted from Kellermann et al. (1998). 2052-474 seems to be a compact unresolved object (see Sect. 5.1), even if it was classified as single sided in the TANAMI paper by Ojha et al. (2010). No double sided jet structure has been found. Additional to the single sided structure two of the sources (1104-445 and 2326-477) show substantial curvature in their structure.
To get an impression on the different scales of the jets of the sources in this work, the mas-scale can be transformed into a pc-scale (see Tab. 5.3). In this scale the jet of 0047-579 can be seen over a distance of ∼250 pc, while the resolved components are on a jet length of ∼80 pc. For 0506-612 also the resolved jet is in the scale of ∼70 pc, while the jet length seen in tapered images reaches a distance of about ∼650 pc from the core. The jet of 0625-354 has a resolved jet on scales of ∼20 pc due to its vicinity to Earth. 1104-445 has a resolved jet length of ∼70 pc, being similar to the sources 0047-579 and

Table 5.4.: Imaging parameters of the X-band (8.4 GHz) epochs

Source	Epoch	Contour[a]	S_{peak}	S_{total}	θ_{maj}	θ_{min}	P.A.	T_b	Core Lum.	Total Lum.
	yyyy-mm-dd	(mJy beam^{-1})	(Jy beam^{-1})	(Jy)	(mas)	(mas)	(°)	(10^{11} K)	(W Hz^{-1})	(W Hz^{-1})
0047-579	2007-11-10	0.782	0.736	1.415	1.70	0.46	4.2	2.82	$2.63{\cdot}10^{28}$	$3.04{\cdot}10^{28}$
0047-579	2008-03-28	0.913	0.836	1.466	2.04	0.48	4.9	2.67	$2.77{\cdot}10^{28}$	$3.15{\cdot}10^{28}$
0047-579	2008-08-08	1.064	1.271	1.555	3.45	1.26	-0.2	4.34	$2.91{\cdot}10^{28}$	$3.34{\cdot}10^{28}$
0047-579	2009-02-23	2.018	0.626	1.122	1.11	0.67	29.9	1.75	$1.99{\cdot}10^{28}$	$2.41{\cdot}10^{28}$
0047-579	2009-12-13	1.544	0.796	1.428	1.31	0.64	19.5	1.35	$2.78{\cdot}10^{28}$	$3.07{\cdot}10^{28}$
0047-579	2010-07-24	0.699	0.718	1.155	1.83	0.87	17.1	1.40	$2.07{\cdot}10^{28}$	$2.48{\cdot}10^{28}$
0506-612	2007-11-10	3.748	0.814	0.955	1.19	0.58	7.7	10.56	$5.35{\cdot}10^{27}$	$5.94{\cdot}10^{27}$
0506-612	2008-03-28	0.789	0.906	1.103	2.05	0.57	3.1	4.72	$6.44{\cdot}10^{27}$	$6.87{\cdot}10^{27}$
0506-612	2008-08-08	0.933	1.006	1.176	3.17	1.18	9.1	2.86	$6.73{\cdot}10^{27}$	$7.32{\cdot}10^{27}$
0506-612	2009-02-23	1.286	0.714	0.936	2.53	0.82	67.8	2.25	$5.18{\cdot}10^{27}$	$5.83{\cdot}10^{27}$
0506-612	2009-12-13	1.193	0.671	0.986	1.28	0.76	40.4	1.31	$5.32{\cdot}10^{27}$	$6.14{\cdot}10^{27}$
0506-612	2010-07-24	0.661	0.582	0.882	1.04	0.89	-43.2	1.00	$4.80{\cdot}10^{27}$	$5.49{\cdot}10^{27}$
0625-354	2007-11-10	0.542	0.273	0.348	2.73	0.80	4.4	1.70	$1.86{\cdot}10^{24}$	$2.32{\cdot}10^{24}$
0625-354	2008-02-07	0.690	0.377	0.460	4.33	3.35	-68.4	0.17	$2.45{\cdot}10^{24}$	$3.07{\cdot}10^{24}$
0625-354	2008-06-09	0.930	0.355	0.454	2.98	0.71	-4.3	2.19	$2.47{\cdot}10^{24}$	$3.03{\cdot}10^{24}$
0625-354	2008-11-27	0.595	0.295	0.401	1.77	1.13	34.7	0.35	$2.28{\cdot}10^{24}$	$2.67{\cdot}10^{24}$
0625-354	2009-12-13	0.999	0.306	0.380	3.66	1.17	5.9	0.49	$2.13{\cdot}10^{24}$	$2.54{\cdot}10^{24}$
0625-354	2010-07-24	0.374	0.279	0.354	3.85	1.15	9.9	0.25	$2.06{\cdot}10^{24}$	$2.36{\cdot}10^{24}$
1104-445	2007-11-10	1.094	0.958	1.365	2.87	0.56	1.6	4.41	$1.82{\cdot}10^{28}$	$2.20{\cdot}10^{28}$
1104-445	2008-02-07	1.289	1.153	1.658	3.52	0.80	-3.8	4.69	$2.11{\cdot}10^{28}$	$2.67{\cdot}10^{28}$
1104-445	2008-06-09	1.464	1.223	1.520	3.22	1.83	-12.6	5.09	$2.02{\cdot}10^{28}$	$2.45{\cdot}10^{28}$
1104-445	2008-11-27	1.979	0.911	1.658	1.08	0.59	32.7	2.57	$2.29{\cdot}10^{28}$	$2.67{\cdot}10^{28}$
1104-445	2009-12-13	1.467	1.107	1.606	2.89	0.75	8.0	2.03	$2.20{\cdot}10^{28}$	$2.58{\cdot}10^{28}$
1104-445	2010-07-24	1.483	0.936	1.540	2.53	0.73	20.8	1.85	$1.93{\cdot}10^{28}$	$2.48{\cdot}10^{28}$
1323-526	2007-11-10	1.159	0.982	1.024	3.71	0.94	13.4	10.45*	-	-
1323-526	2008-02-07	1.295	1.347	1.395	5.07	3.51	87.0	0.48*	-	-
1323-526	2008-03-28	0.472	0.717	1.026	3.48	0.72	-8.0	0.12*	-	-
1323-526	2008-08-08	0.913	1.080	1.121	5.07	3.52	-71.2	0.38*	-	-
1323-526	2009-02-27	1.036	1.221	1.390	2.84	1.10	21.9	1.11*	-	-
1323-526	2010-03-12	1.043	0.736	0.782	5.09	3.28	87.0	0.95*	-	-
2005-489	2007-11-10	0.910	0.388	0.635	3.76	0.72	34.7	0.36	$2.85{\cdot}10^{24}$	$7.11{\cdot}10^{24}$
2005-489	2008-03-28	0.526	0.357	0.686	2.75	0.55	-4.0	0.30	$5.37{\cdot}10^{24}$	$7.69{\cdot}10^{24}$
2005-489	2008-08-08	0.485	0.502	0.796	3.69	0.90	-5.5	0.28	$5.97{\cdot}10^{24}$	$8.92{\cdot}10^{24}$
2005-489	2009-02-23	1.302	0.397	0.759	2.44	0.78	38.3	0.33	$4.93{\cdot}10^{24}$	$8.50{\cdot}10^{24}$
2005-489	2009-12-13	1.118	0.420	0.642	3.15	0.89	29.6	0.29	$5.61{\cdot}10^{24}$	$7.20{\cdot}10^{24}$
2005-489	2010-07-24	0.333	0.399	0.604	3.66	1.53	23.7	0.33	$4.00{\cdot}10^{24}$	$6.76{\cdot}10^{24}$
2052-474	2008-02-07	1.867	1.501	1.704	3.16	0.47	13.0	14.08	$2.27{\cdot}10^{28}$	$2.29{\cdot}10^{28}$
2052-474	2008-03-28	1.425	1.520	1.674	2.81	0.65	0.2	10.05	$2.23{\cdot}10^{28}$	$2.25{\cdot}10^{28}$
2052-474	2008-08-08	1.219	1.751	1.779	4.02	1.25	-0.6	15.92	$2.38{\cdot}10^{28}$	$2.39{\cdot}10^{28}$
2052-474	2009-02-23	2.630	1.135	1.670	1.89	0.48	19.8	3.46	$2.22{\cdot}10^{28}$	$2.25{\cdot}10^{28}$
2052-474	2009-09-05	1.519	1.210	1.851	2.43	0.54	16.8	3.23	$2.49{\cdot}10^{28}$	$2.49{\cdot}10^{28}$
2052-474	2010-03-12	2.773	1.910	2.001	5.46	2.92	73.8	1.53	$2.70{\cdot}10^{28}$	$2.69{\cdot}10^{28}$
2326-477	2007-11-10	0.627	0.509	0.953	1.88	0.53	6.1	3.11	$5.87{\cdot}10^{27}$	$9.21{\cdot}10^{27}$
2326-477	2008-03-28	0.813	0.650	1.175	3.09	0.59	2.9	3.12	$7.50{\cdot}10^{27}$	$1.14{\cdot}10^{28}$
2326-477	2008-08-08	0.641	0.764	1.296	3.88	2.15	-9.0	3.35	$7.68{\cdot}10^{27}$	$1.25{\cdot}10^{28}$
2326-477	2009-02-23	1.666	0.550	1.142	1.02	0.69	-12.5	1.86	$6.90{\cdot}10^{27}$	$1.10{\cdot}10^{28}$
2326-477	2009-12-13	2.248	0.899	1.618	1.97	0.53	20.6	3.21	$1.27{\cdot}10^{28}$	$1.56{\cdot}10^{28}$
2326-477	2010-07-24	0.875	0.840	1.539	2.29	0.71	14.7	2.06	$1.04{\cdot}10^{28}$	$1.49{\cdot}10^{28}$

Cosmology for the luminosity calculation $H_0 = 73\,\mathrm{km\,s^{-1}\,Mpc^{-1}}$, $\Omega_m = 0.27$, $\Omega_\Lambda = 0.73$
[a]: lowest Contours = 3x RMS noise in image
*: because of no redshift for 1323-526, the redshift was set to z = 0

Table 5.5.: Imaging parameters of the K-band (22.3 GHz) epochs

Source	Epoch	Contour[a]	S_{peak}	S_{total}	θ_{maj}	θ_{min}	P.A.	T_b	Core Lum.	Total Lum.
	yyyy-mm-dd	(mJy beam^{-1})	(Jy beam^{-1})	(Jy)	(mas)	(mas)	(°)	(10^{10} K)	(W Hz^{-1})	(W Hz^{-1})
0047-579	2008-03-26	3.404	0.604	0.790	1.83	1.46	-71.3	0.87	$1.64{\cdot}10^{28}$	$1.70{\cdot}10^{28}$
0047-579	2008-08-08	1.895	0.436	0.602	1.90	1.29	70.0	0.60	$1.26{\cdot}10^{28}$	$1.29{\cdot}10^{28}$
0506-612	2008-03-26	3.488	0.773	0.894	1.81	1.37	-84.2	1.28	$5.58{\cdot}10^{27}$	$5.56{\cdot}10^{27}$
0506-612	2008-08-08	2.020	0.502	0.557	2.08	1.43	-65.7	1.15	$3.40{\cdot}10^{27}$	$3.47{\cdot}10^{27}$
0625-354	2008-02-06	2.556	0.147	0.243	1.57	1.18	-61.9	0.066	$1.57{\cdot}10^{24}$	$1.62{\cdot}10^{24}$
0625-354	2008-11-29	0.972	0.179	0.219	2.15	1.61	-84.0	0.11	$1.39{\cdot}10^{24}$	$1.46{\cdot}10^{24}$
1104-445	2008-02-06	2.298	0.290	0.472	1.61	1.37	-77.6	0.35	$7.19{\cdot}10^{27}$	$7.60{\cdot}10^{27}$
1104-445	2008-11-29	1.733	0.528	0.796	1.81	1.39	84.9	0.57	$1.23{\cdot}10^{28}$	$1.28{\cdot}10^{28}$
1323-526	2008-02-06	2.823	0.644	0.688	1.86	1.38	79.9	0.97*	-	-
1323-526	2008-03-26	2.996	0.703	0.768	1.92	1.40	-73.9	1.30*	-	-
1323-526	2008-08-08	2.396	0.827	0.919	1.76	1.30	-79.2	1.16*	-	-
2005-489	2008-03-26	1.861	0.182	0.315	2.24	1.49	-72.2	0.045	$3.37{\cdot}10^{24}$	$3.52{\cdot}10^{24}$
2005-489	2008-08-08	1.159	0.206	0.371	1.62	1.44	76.1	0.051	$4.09{\cdot}10^{24}$	$4.16{\cdot}10^{24}$
2052-474	2008-02-06	4.306	0.895	0.862	1.92	1.37	-64.0	15.50	$1.21{\cdot}10^{28}$	$1.16{\cdot}10^{28}$
2052-474	2008-03-26	3.665	0.872	0.968	1.73	1.28	-81.3	2.77	$1.31{\cdot}10^{28}$	$1.30{\cdot}10^{28}$
2052-474	2008-08-08	3.244	1.344	1.331	2.04	1.41	-69.0	43.55	$1.84{\cdot}10^{28}$	$1.79{\cdot}10^{28}$
2326-477	2008-03-26	3.600	0.577	0.759	1.74	1.29	-80.9	3.01	$5.98{\cdot}10^{27}$	$7.34{\cdot}10^{27}$
2326-477	2008-08-08	1.832	0.623	0.840	1.88	1.27	-86.3	1.29	$6.97{\cdot}10^{27}$	$8.11{\cdot}10^{27}$

Cosmology for the luminosity calculation $H_0 = 73\,\mathrm{km\,s^{-1}\,Mpc^{-1}}$, $\Omega_m = 0.27$, $\Omega_\Lambda = 0.73$
[a]: lowest Contours = 3x RMS noise in image
*: because of no redshift for 1323-526, the redshift was set to z = 0

0506-612. 2005-489 is similar to 0625-354 having a jet length of ∼35 pc. 2326-477 is a distant source with a resolved jet length of ∼120 pc. Therefore the resolution in all images corresponds to a pc-scale.

5.3. Multi-epoch analysis

Models

The brightness distribution for all X-band observations of all sources has been parametrized by fitting circular model components with a 2D Gaussian emission profile in the visibility domain (see Sect. 4.2.3). In Fig. 5.20 - 5.23 the location of the Gaussian model components are shown overlaid on the CLEAN-images of the brightness distribution (Fig. 5.1 - 5.16). Only the X-band images were used because of higher resolution and better uv-coverage. The color of the model components represents the identification over all epochs. If the model component was found in at least five epochs, a linear regression fit was made. Model components with large diameter mostly collect diffuse extended emission instead of being a clear feature to localize in the brightness distribution. Therefore the outer components and features with low contour levels are not reliable for a multi-epoch analysis. For the following results the components are numbered with rising

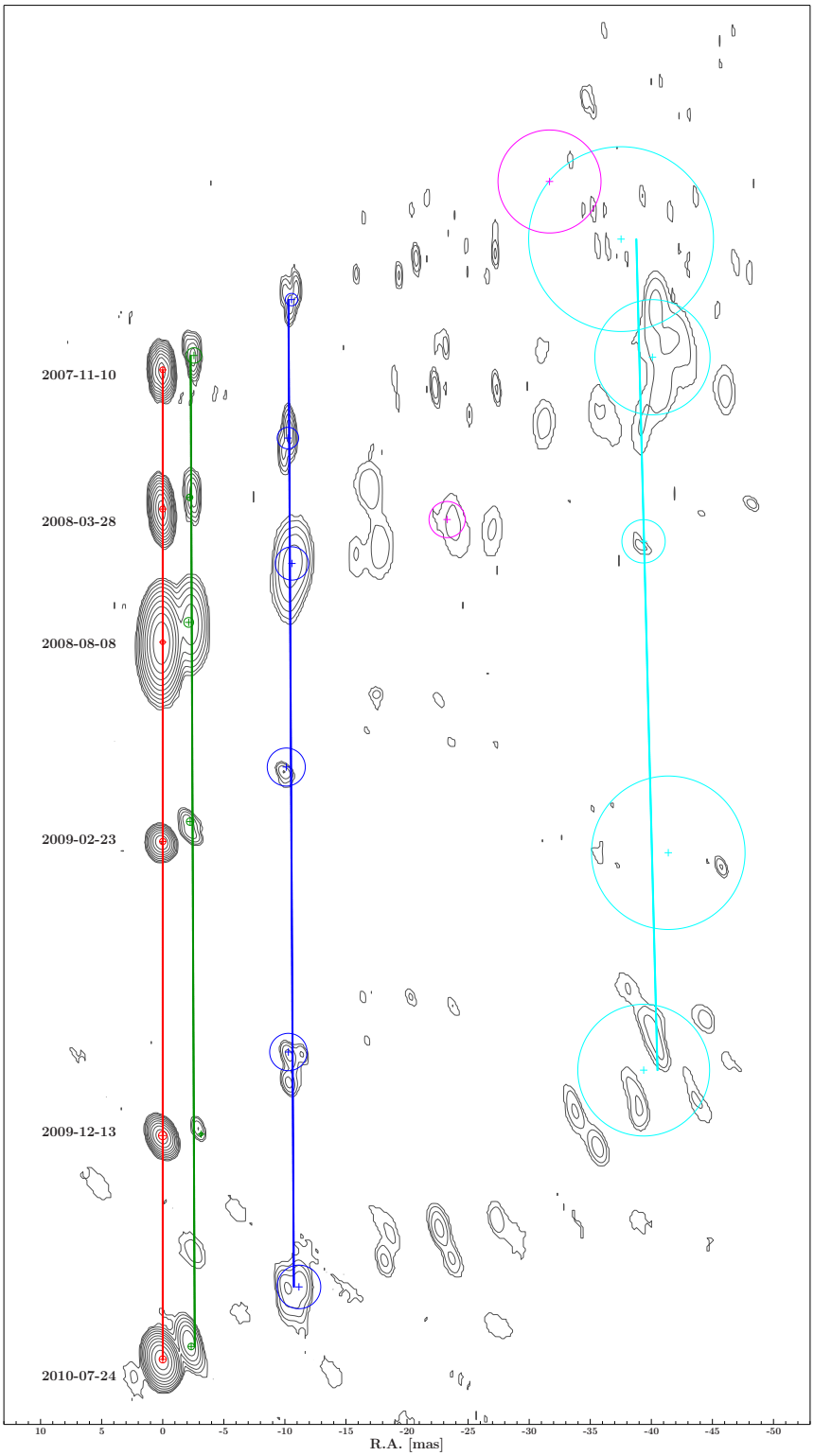

Figure 5.20.: Component association for all six epochs of 0047-579

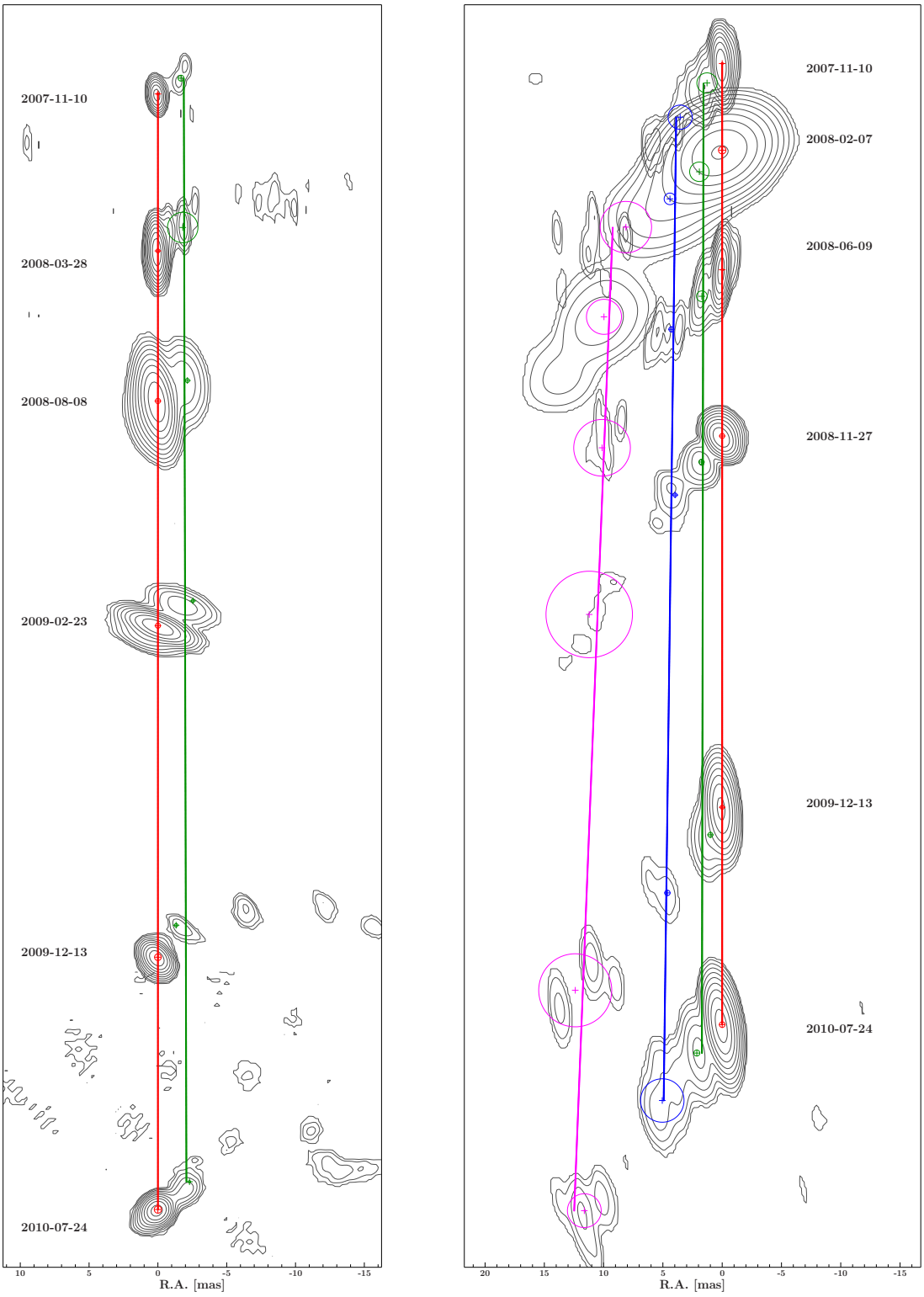

Figure 5.21.: Component association for all six epochs of 0506-612 (left) and 0625-354 (right)

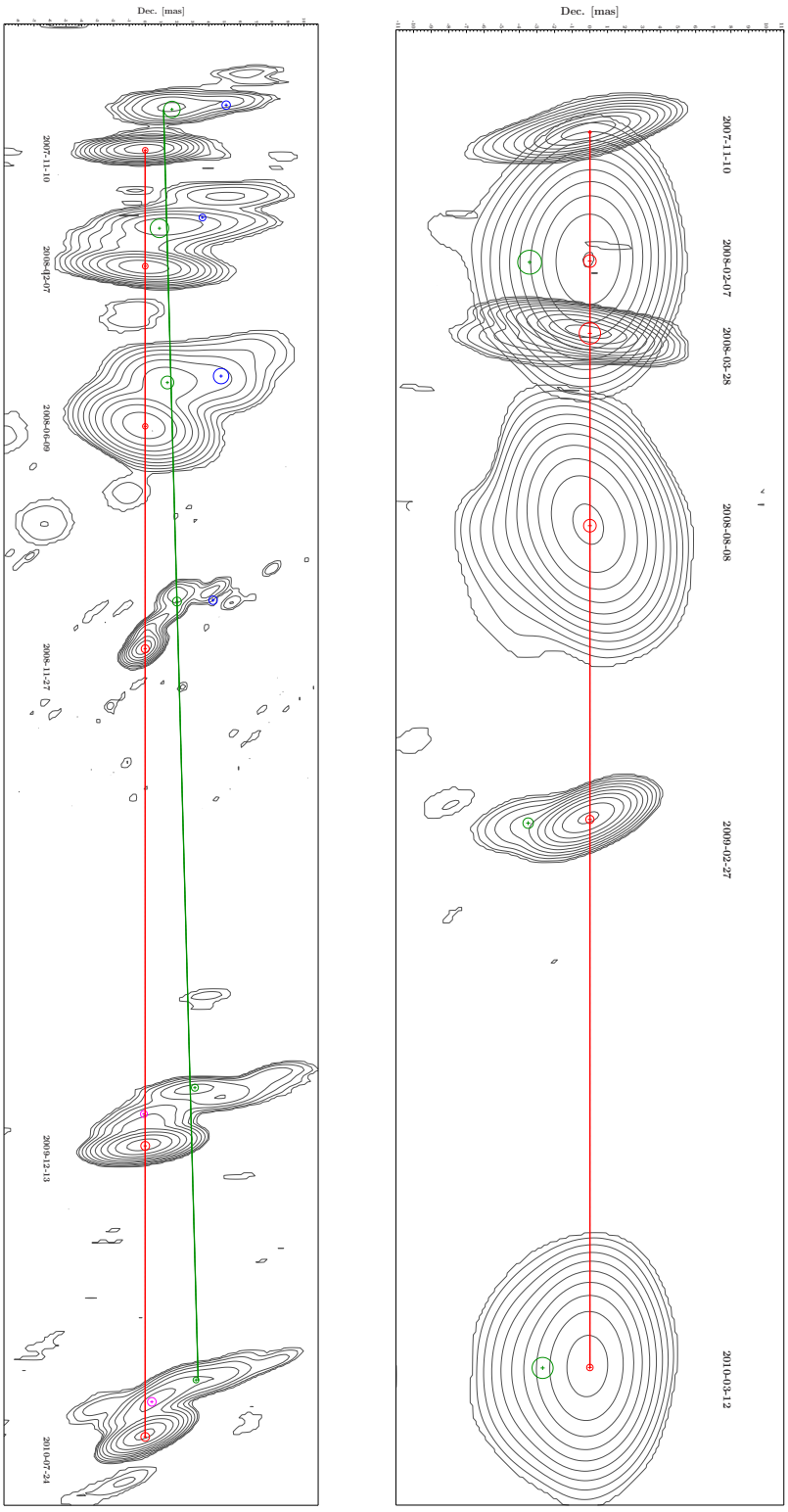

Figure 5.22.: Component association for all six epochs of 1104-445 (top) and 1323-526 (bottom)

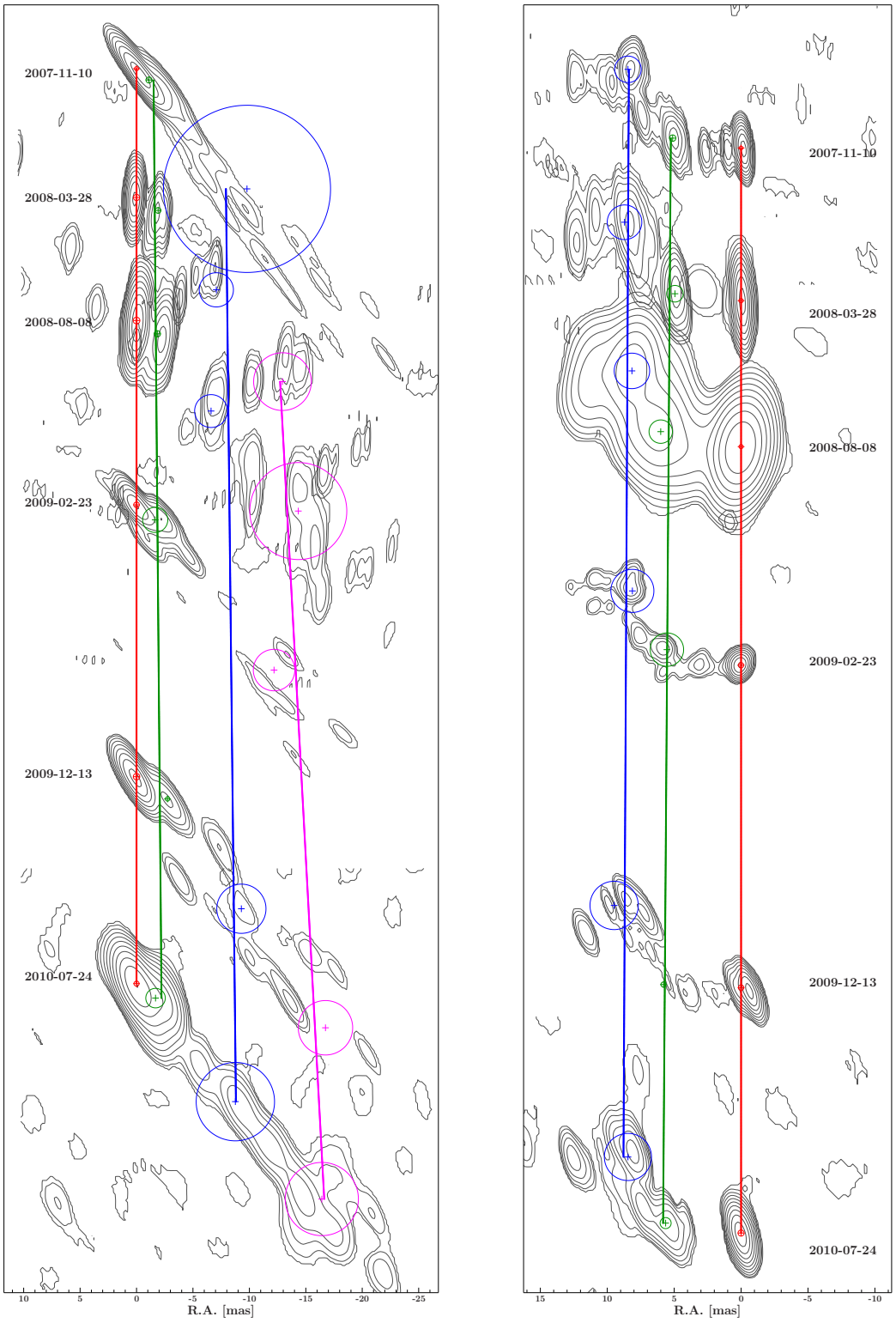

Figure 5.23.: Component association for all six epochs of 2005-489 (left) and 2326-474 (right)

number in distance from the core component in the first epoch (also can be seen in Fig. 5.28 - 5.30), components appearing in later epochs got the next number (see Fig. 5.29). The model of 0047-579 shows two jet components near the core in every epoch and some extended emission at larger distance. This extended emission is characterized by large low surface-brightness components and and is partially resolved. Therefore only the first two components are considered reliable.
Fig. 5.21 shows the multi-epoch model of 0506-612 with only one component found near the core. In two epochs some more extended emission is visible. Also the more distant emission about 50-80 mas away from the core could not be modelled because of too faint extended features and uncertain localization.
0625-354 is modelled with three components (Fig. 5.21). All components are found in every epoch. The second epoch has worse uv-coverage than all the other epochs.
The jet of 1104-445 (Fig. 5.22) is modelled with two components besides the core in every epoch. While the distant component of the first four epochs becomes faint and vanishes, in the last two epochs a new component near the core is found. The outer component of the first epochs cannot be modelled in the last two epochs even if the images suggest still a weak component in the corresponding region. The images of the first three epochs also show weak emission east of component 2.
1323-526 has no component found in every epoch (Fig. 5.22). The beams are very large due to missing long baselines in three epochs. However in three of the six epochs the modelling shows also a component in the south of the core.
2005-489 is modelled with three components (see Fig. 5.23). Component 2 and 3 are only found in five of the six epochs. Component 3 is very hard to locate, because the component is only partially resolved in most epochs. Component 2 is also difficult to locate in the observations of Nov. 2007 and Dec. 2009. Only component 1 can be tracked and identified in every epoch.
2052-474 was modelled with only a core component. Therefore a multi-epoch image was omitted and also no kinematic study is possible for this source.
2326-477 (Fig. 5.23) contains a jet structure with S-shape and two identified components. A third component is suggested in the images but could not be localized in the modelling process. Component 1 is very weak in the observation of Dec. 2009. However it can be found and fits in the position expected from the other epochs. Because of the S-shape it is difficult to determine a jet angle for this object similar to 1104-445.

Flux density

Fig. 5.24 - 5.27 show the temporal flux evolution of each identified component. All objects have a dominant core flux density. All plots show error bars for the flux density values. This error is an estimated relative error of 10% on each value resulting from calibration and imaging errors. The core flux of 0625-354 (Fig. 5.25) shows a core with low variability. An ideal expectation of a constant flux in the radio galaxy leads to a relative error for the mean of the flux density of 10.68%. Ignoring the first epoch, it would be

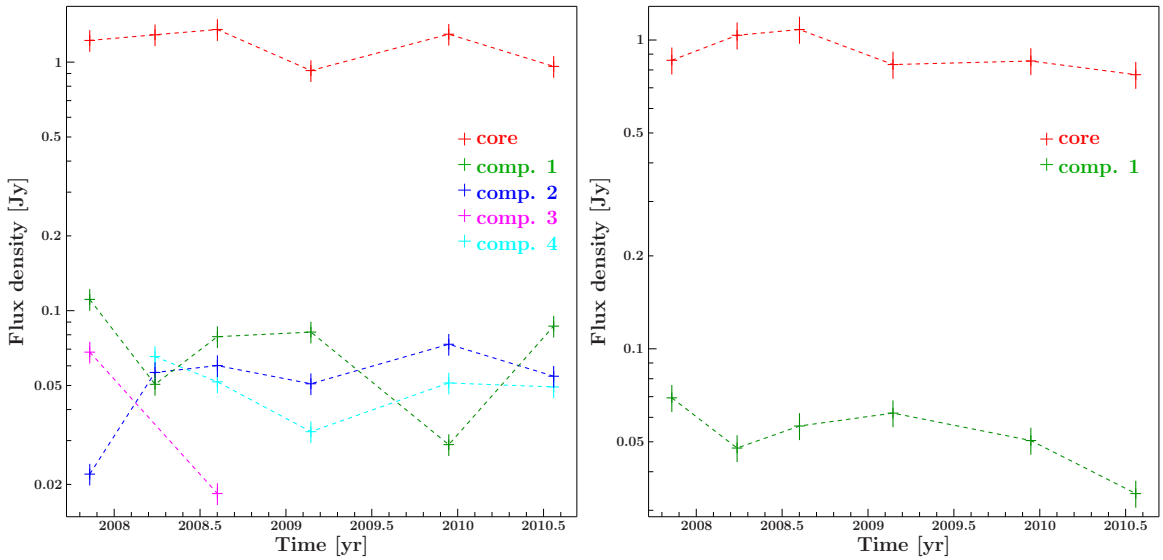

Figure 5.24.: Evolution of flux density over all epochs for 0047-579 (left) and 0506-612 (right). The error bars indicate a global error of 10% for the flux density values.

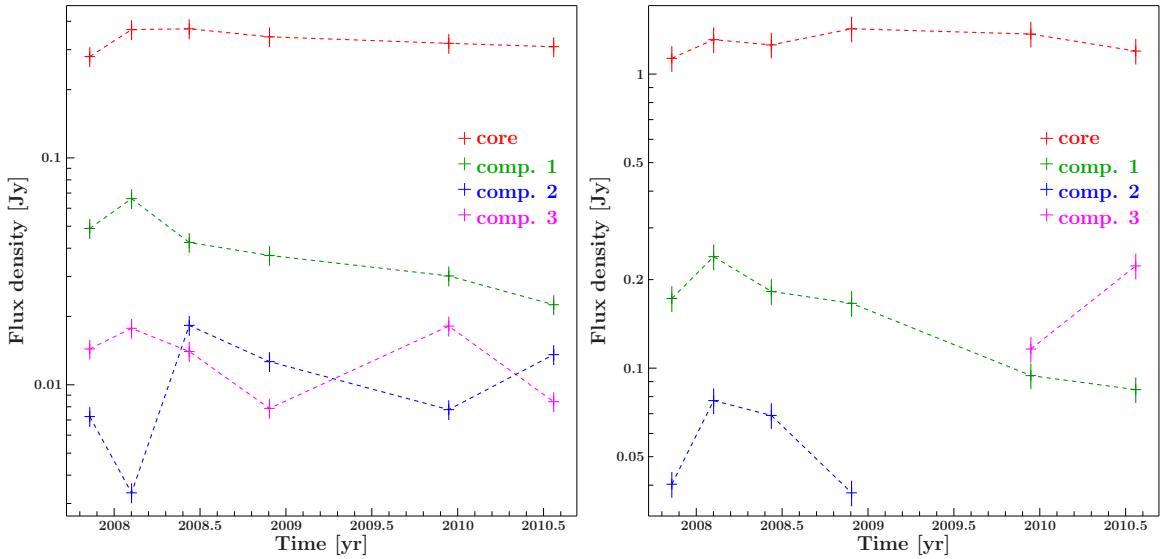

Figure 5.25.: Evolution of flux density over all epochs for 0625-354 (left) and 1104-445 (right). The error bars indicate a global error of 10% for the flux density values.

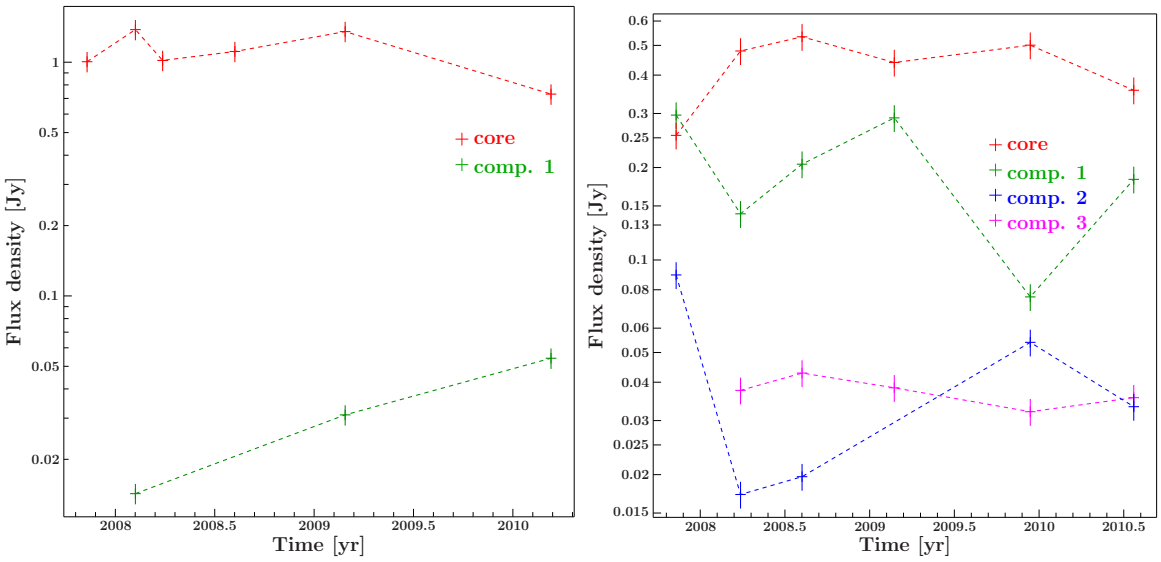

Figure 5.26.: Evolution of flux density over all epochs for 1323-526 (left) and 2005-489 (right). The error bars indicate a global error of 10% for the flux density values.

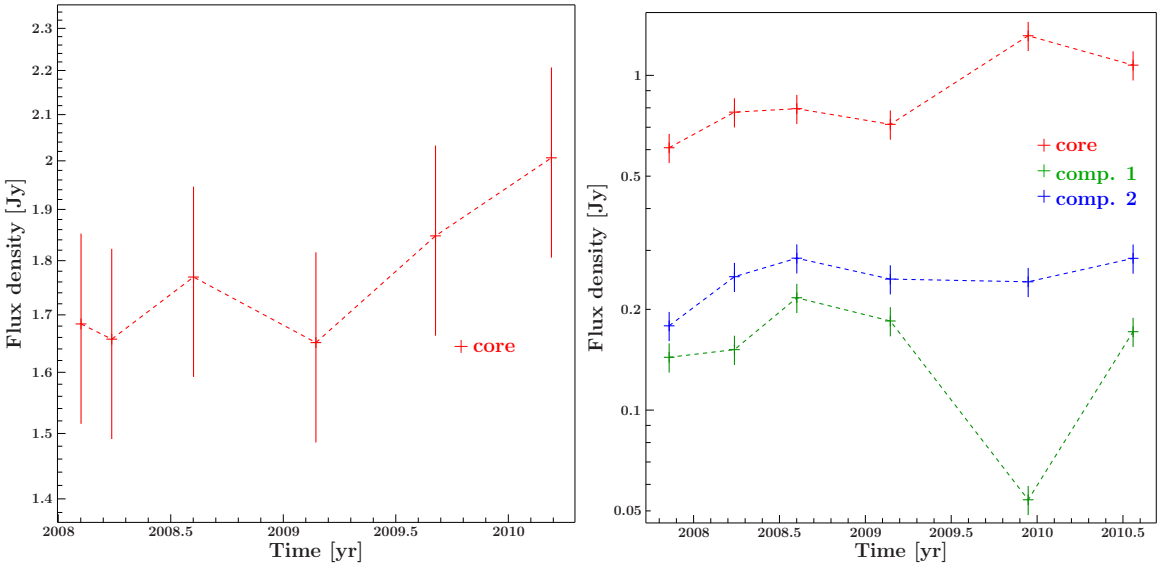

Figure 5.27.: Evolution of flux density over all epochs for 2052-474 (left) and 2326-477 (right). The error bars indicate a global error of 10% for the flux density values.

only 8.07%. However the flux density can in fact show low-level variability, so that an universal uncertainty of 10% for all epochs is assumed. For non-isolated jet components, this is an underestimation of the true uncertainties because adjacent components can be strongly coupled in the modelling process.
0047-579 (Fig. 5.24) shows that the jet components have flux densities about one order of magnitude lower than the core. Component 1 is very weak in the fifth epoch like mentioned and seen before. Component 2 is weak in the first epoch but remains stable in the other epochs. The distant components consisting of small emission regions combined in large components show low flux density.
The flux density of 0506-612 (Fig. 5.24) is somewhat enhanced in the epochs of Mar. and Aug. 2008. The single jet component decreases in flux density. In the second epoch, the core could have collected some of the flux of the component being close to the core, resulting in a decrease of the flux in component 1 and an increase of flux in the core.
0625-354 (Fig. 5.25) shows a globally lower flux density in the first epoch, which could be due to an amplitude calibration error. The core remains stable over time, while component 1 gets fainter over time while moving away from the core. Component 2 is very weak in the second epoch and shows a decrease of flux density in the observation of Dec. 2009. Component 3 was also weak in the images in the epochs of Jun. and Nov. 2008, which can also be seen in the flux density.
The flux density evolution of 1104-445 (Fig. 5.25) shows again a nearly stable core and a decreasing flux of the first component moving away from the core. Component 2 gets fainter over time, explaining that it is probably too faint to be detected in the last two epochs. Therefore a new component in the last two epochs is found which rises in flux density, making it distinguishable from the core.
1323-526 (Fig 5.26) shows variability in the flux of the core. The single jet component is about two orders of magnitude weaker than the core, explaining why it is hard to detect in the other epochs.
Fig 5.26 shows 2005-489 a weaker flux density in the first epoch but the component near the core has a relatively high flux density. This might be due to a strong coupling of the core and the nearby component 1. Also here the observation of Dec. 2009 shows a weak component. Component 3 is hard to locate because it is only partially resolved.
Like mentioned in Sect. 5.2 the core luminosities for 2052-474 and 2326-477 show a rising flux density in the last two epochs. For 2052-474 this increase in flux density was also observed by Blanchard et al. (2012) (Fig. 5 of the paper), where it was associated with one of two flaring events seen in the lightcurves of *Fermi* in February and June 2009 (Abdo et al. 2010c). A flare in the optical in June/July 2009 was also observed by Hauser et al. (2009) with *ATOM* (Automatic Telescope for Optical Monitoring, operated by the HESS Collaboration). Blanchard et al. (2012) find a maximum in the flux density at July 2010, while the last epoch of the data in this work is in March 2010 and therefore it shows only the beginning of the increase of the flux density.
2326-477 has an increase in flux density mainly in Dec. 2009, where the first component near the core is very weak. In this case the core could have taken some flux density due

Table 5.6.: Kinematic results using linear regression

Source	component ID	apparent velocity (mas/yr)	apparent velocity (c)	redshift z
0047-579	1	0.039 ± 0.117	2.97 ± 8.88	1.797
0047-579	2	0.210 ± 0.119	15.90 ± 9.06	1.797
0506-612	1	0.286 ± 0.118	15.60 ± 6.44	1.093
0625-354	1	0.234 ± 0.134	0.83 ± 0.47	0.055
0625-354	**2**	**1.024 ± 0.192**	**3.63 ± 0.68**	0.055
0625-354	3	1.217 ± 0.293	4.31 ± 1.04	0.055
1104-445	**1**	**0.817 ± 0.136**	**57.67 ± 9.58**	1.598
2005-489	1	0.397 ± 0.331	1.80 ± 1.50	0.071
2005-489	2	0.804 ± 0.921	3.63 ± 4.16	0.071
2005-489	3	2.556 ± 1.575	11.55 ± 7.12	0.071
2326-477	1	0.241 ± 0.202	14.84 ± 12.47	1.034
2326-477	2	0.179 ± 0.371	11.06 ± 22.91	1.034

Components in bold correspond to the excellent quality component classification by Kellermann et al. (2004)

to coupling with component 1. Besides, all components show nearly the same shape of flux density evolution like the core at this object. And like at other objects the first epoch seems weaker than the other epochs.
There is a similarity of decreasing flux densities of the core closest component in the data from Dec. 2009. 0047-579, 2005-489 and 2326-477 show all a spike in the flux density in this epoch. This can be due to coupling with the core or may have the origin in the data itself. Three of six sources observed in this epoch of the sample in this work, show this deviation.

Kinematics

Tab. 5.6 lists the values for the velocities obtained from the models through fitting a linear regression at the date to radial distance data points. Only the reliable components found in at least five epochs are used, ignoring components with only partially resolved emission. To classify the quality of components, the criteria adapted from Kellermann et al. (2004) are used. The criteria are:

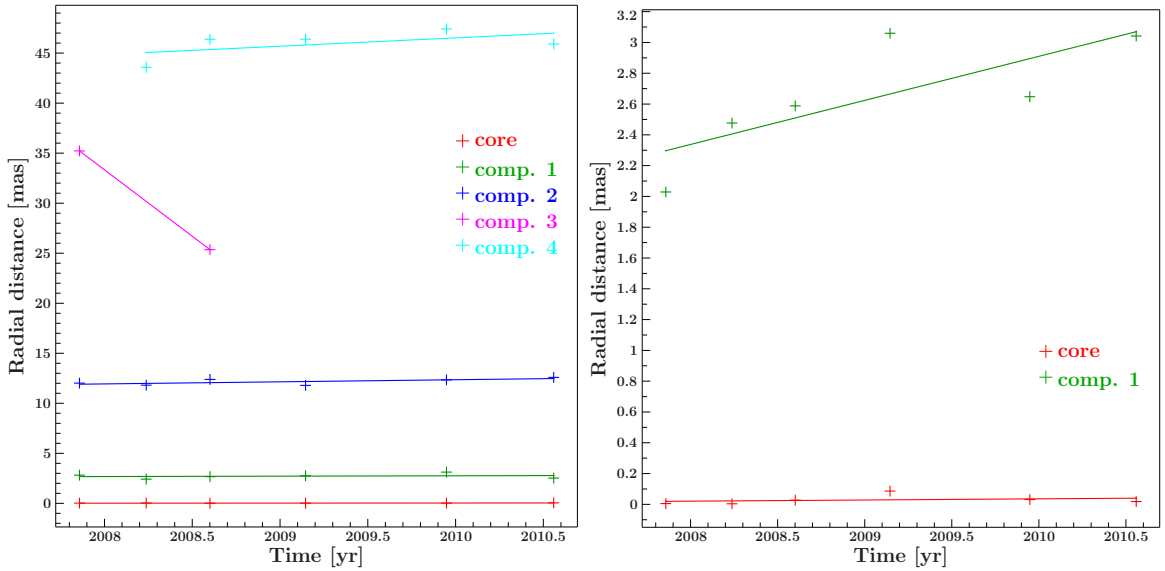

Figure 5.28.: Distance evolution over time of the components of 0047-579 (left) and 0506-612 (right)

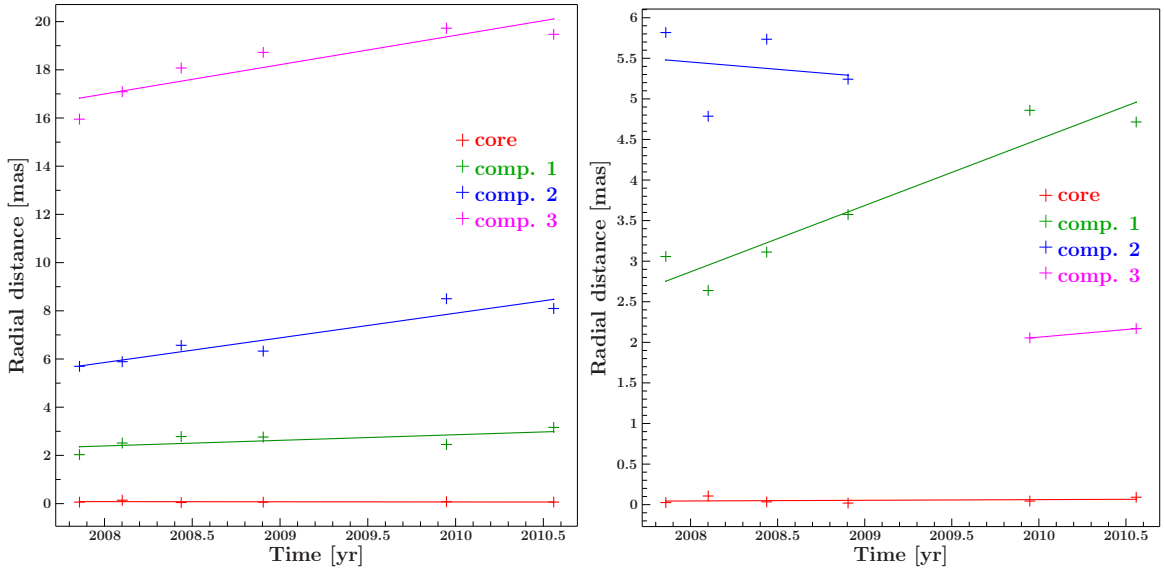

Figure 5.29.: Distance evolution over time of the components of 0625-354 (left) and 1104-445 (right)

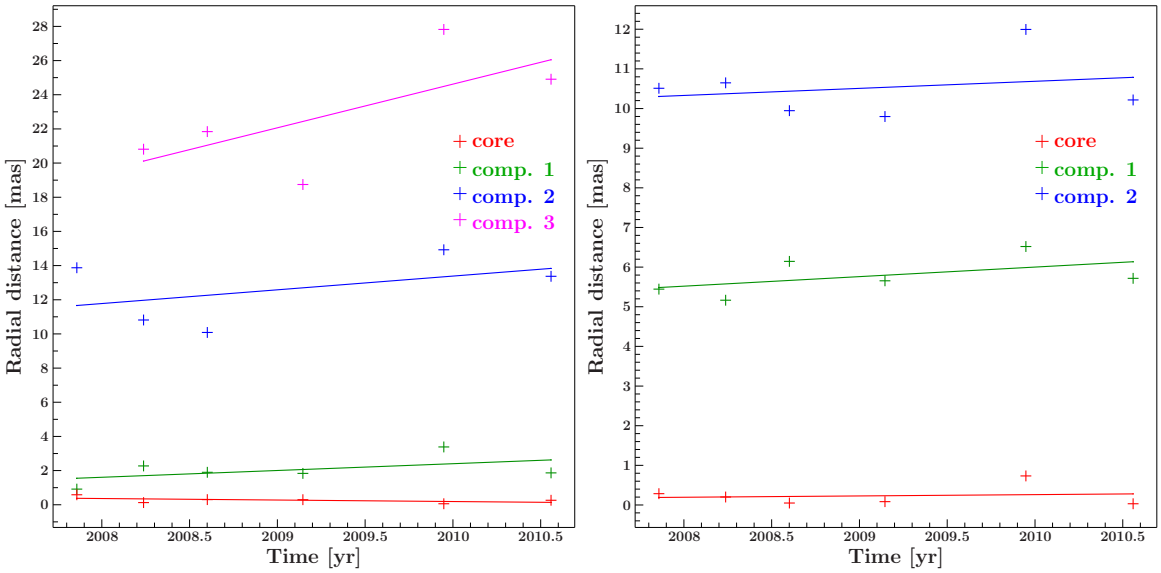

Figure 5.30.: Distance evolution over time of the components of 2005-489 (left) and 2326-477 (right)

- The component position is determined at four or more observations.
- The component is a well-defined feature whose position can be unambiguously determined to a small fraction of the beamwidth.
- The best-fitting angular speed is determined to high accuracy, defined by a significance of $\geq 5\ \sigma$, where σ is the uncertainty of the velocity.

If the component is conform with all three of the criteria are satisfied, the component is classified as "Excellent", while components satisfying only two criteria are classified as "Good", with one criteria as "Fair" and none of the criteria as "Poor". In this work two components can be classified as "Excellent", they are printed in bold in Tab. 5.6. While component 3 of 2005-489 is classified as "Fair", all other components in Tab. 5.6 can be classified as "Good", fulfilling the first two criteria. The date-distance diagrams with the linear regression fits are found at Fig. 5.28 - 5.30. The both compact sources 1323-526 and 2052-474 do not allow kinematic studies to be performed.
The gradient of the linear regression fits give the velocity in mas/yr and can be calculated to apparent velocities in units of the speed of light. The error given in Tab. 5.6 only takes in account the standard deviation of the components in the distance from the linear fit. Therefore it should be mentioned that there could also exist errors regarding the location of the components and the angle, which are not taken into account in these values. Also all data points were weighted equally, ignoring the different qualities of data in the observations of every epoch. Most of the velocities have larger relative errors.
The velocities of 0047-579 from Fig. 5.28 have both errors of about $10c$, which is the

result of minor differences from the fit but at a very high redshift. While component 1 can be a stationary feature in the limits of its error, component 2 shows a motion. Due to the range of the error the velocity is not determined very well, but apparent superluminal motion is suggested.
The jet of 0506-612 shows only one component near the core. Even though there is emission more distant, it is impossible to model a component, which can be tracked over multiple epochs. The component found has apparent superluminal motion with a velocity of $(15.6\pm6.4)c$ (see Fig. 5.28).
0625-354 has a jet of three components with significant lower relative errors (see Fig. 5.29). Component 2 is classified as "Excellent" with apparent velocity of $(3.63\pm0.68)c$. The other two components are classified as "Good" and combining all three components gives this jet a mean speed of $(2.92\pm0.44)c$. Therefore the jet shows superluminal apparent motion with a reliable velocity.
The jet of 1104-445 has only one component traceable over all epochs, but it is classified as "Excellent". It has a very high superluminal motion of $(57.7\pm9.6)c$. However the high redshift respectively the large distance leads to a higher speed than expected. Also the jet angle is difficult to determine because the jet shows substantial curvature.
Fig. 5.30 shows three components for 2005-489 and Tab. 5.6 contains velocities for all three components, but the third component is difficult to track and only classified as "Fair". It was not found in the first epoch and has a large component size in a region with no clear components. However it has a velocity with a relative error of only 62 % and therefore indicates an apparent superluminal motion of this feature. Also the second component is hard to locate clearly in the images, missing in one epoch and leads to a velocity with an error bar larger than the best value. This indicates that there probably is a component but the motion or velocity cannot be constrained. Component 1 nearest to the core is well defined and has more flux than the other components. In the first epoch it seems to be too close to the core and taking some of the core flux. Besides, the component has a velocity of $(1.8\pm1.5)c$, suggesting mildly superluminal motion.
The jet of 2326-477 shows substantial curvature, making it difficult to determine a jet position angle. However the two components are clear to identify and can be tracked in almost every epoch, only component 1 is very weak in the fifth epoch. Both epochs have almost the same speeds but different error bars. The velocity of the second component has a large uncertainty about two times of the best value. This means the component is identifiable but no motion can be measured. The first component has a speed of $(14.8\pm12.5)c$ which shows also a large uncertainty, making it difficult to determine a velocity of this jet.

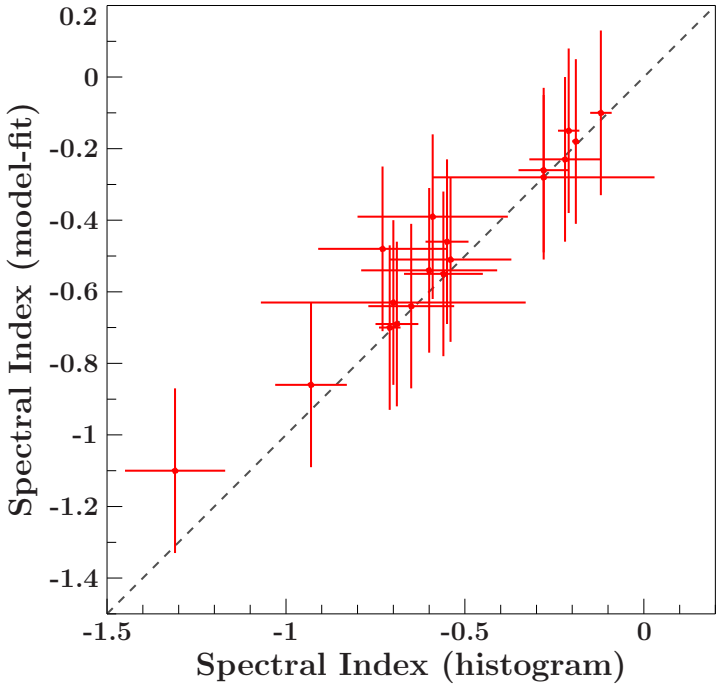

Figure 5.31.: Comparison of spectral indices obtained from core regions of spectral index maps and spectral indices calculated with core components of the model-fitting process

5.4. Spectral index maps

The combination of 8.4 and 22.3 GHz data allows the construction of spectral index images displaying the spectral properties on mas-scales (Fig. 5.33 - 5.40). The spectral index of the core was determined by counting the pixel of the spectral index map in a region corresponding to the bigger beam of the both datasets with addition of the component size of the model component in the X-band, like explained in Sect. 4.2.4. The histograms showing the different core region spectral indices are found in Fig. A.5 - A.11. The average core region spectral index and the corresponding standard deviation determined with the spectral index maps and the spectral index calculated from the flux densities of the core components for each source can be found in Tab. 5.7. The standard deviation value represents the width of the peak and hence the variation and gradients existing in the core region. Broad peaks indicate that the spectral index is not well defined across the core. However this error does not cover the uncertainties in the flux densities in the both brightness distribution maps. For the X-band observations a global uncertainty of 10% in the flux density and 20% for the K-band was assumed, because of the worse uv-coverage in the K-band. This leads to an global error for every spectral index α of 0.23 due to uncertainties in the flux densities after the following equation for the error of α calculated with Eq. 4.2.1:

Table 5.7.: Spectral indices of core region

Source	Epoch	Spectral index (histograms)	Spectral index (model-fit)
0047-579	Mar. 2008	-0.60 ± 0.19	-0.54 ± 0.23
0047-579	Aug. 2008	-0.93 ± 0.10	-0.86 ± 0.23
0506-612	Mar. 2008	-0.21 ± 0.03	-0.15 ± 0.23
0506-612	Aug. 2008	-0.71 ± 0.03	-0.70 ± 0.23
0625-354	Feb. 2008	-0.55 ± 0.06	-0.46 ± 0.23
0625-354	Nov. 2008	-0.54 ± 0.17	-0.51 ± 0.23
1104-445	Feb. 2008	-1.31 ± 0.14	-1.10 ± 0.23
1104-445	Nov. 2008	-0.70 ± 0.37*	-0.63 ± 0.23
1323-526	Feb. 2008	-0.69 ± 0.06	-0.69 ± 0.23
1323-526	Mar. 2008	-0.28 ± 0.31*	-0.28 ± 0.23
1323-526	Aug. 2008	-0.19 ± 0.01	-0.18 ± 0.23
2005-489	Mar. 2008	-0.73 ± 0.18	-0.48 ± 0.23
2005-489	Aug. 2008	-0.59 ± 0.21	-0.39 ± 0.23
2052-474	Feb. 2008	-0.65 ± 0.12	-0.64 ± 0.23
2052-474	Mar. 2008	-0.56 ± 0.11	-0.55 ± 0.23
2052-474	Aug. 2008	-0.28 ± 0.07	-0.26 ± 0.23
2326-477	Mar. 2008	-0.22 ± 0.10	-0.23 ± 0.23
2326-477	Aug. 2008	-0.12 ± 0.03	-0.10 ± 0.23

The spectral index of the core corresponds to the average value all spectral indices in the core region (for the histograms see Fig. A.5 - A.11) with errors representing the standard deviation from the mean value.
*: These values have a standard deviation larger than the uncertainties of the flux densities of σ_{flux}=0.23.

$$\sigma_\alpha = (\log \nu_X - \log \nu_K)^{-1} \sqrt{\left(\frac{\sigma_{S(X)}}{S_X}\right)^2 + \left(\frac{\sigma_{S(K)}}{S_K}\right)^2} \tag{5.4.1}$$

$$\text{for the assumed values: } \frac{\sigma_{S(X)}}{S_X} = 10\% \text{ and } \frac{\sigma_{S(K)}}{S_K} = 20\%$$

$$\sigma_\alpha = 0.229022 \tag{5.4.2}$$

To compare the two methods of calculating the spectral index, the values are plotted in Fig. 5.31. In range of their uncertainties all values are on a line through the origin, which shows that the methods are consistent. For the spectral indices from the histograms the values with lower error values than 0.23, the spectral index is well defined. Only two histograms have standard deviations larger than the uncertainty of the flux densities. The corresponding histograms of these two values also show broad peaks, influenced by gradients in the core region of the spectral index map.
All core regions have a spectral index between 0 and -1.5, where only one value is below -1.0. This is consistent with other VLBI spectral index studies for example by Lobanov

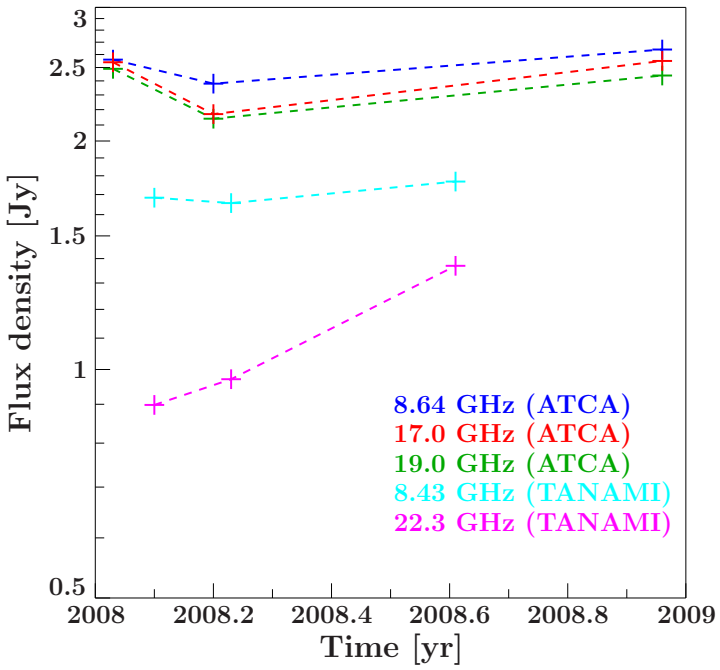

Figure 5.32.: Flux values at different frequencies measured with the TANAMI associated program C1730 (PI: *P. Edwards*; Tingay et al. (2009)) with the ATCA telescope compared with the core fluxes of 2052-474.

& Zensus (1999); Kadler et al. (2004); Ros & Lobanov (2001); Taylor et al. (2005). Taylor et al. (2005) studies a sample of 24 sources, where the spectral index of 21 sources was determined. The values are in a range of -1.32 to 0.33 with most sources being between -1 and 0. This is consistent with the values of the sample in this work. While the core of 3C 309.1 has a spectral index between -0.5 and 0 (Ros & Lobanov 2001), Lobanov & Zensus (1999) found a spectral index for the core component of 3C 345 in the range between -0.2 and -0.1. The flattest core spectra are found for 2326-477 (-0.22 and -0.12), while 0625-354, 2005-489 and 2052-474 show rather steep spectral indices of $\sim$ -0.5.

Fig. 5.33 shows the spectral index maps of 0047-579 for the epochs in Mar. and Aug. 2008. It is one of the sources where also jet components where found in the K-band and can be seen in the spectral index maps. The gradient to a steep spectral index defines the border between the core and the component close to the core, while the components are optically thin. The spectral indices of the cores in both epochs are similar with a slightly flatter spectrum in the Mar. 2008 epoch. The upper part of the second component in the first epoch and the orange border on the left in the second epoch suggests slightly different locations of the components in the images.

0506-612 (Fig. 5.34) shows no jet in the spectral index map above the 3σ rms noise level. However, in direction of the first jet component in the north-west it can be seen

that the core gets optically thinner. The different spectral indices can be interpreted as a flare through the wavelengths. While the flare is happening in the K-band in the first epoch, the wavelength of the flare has moved to the X-band in the second epoch. The spectral index map of Mar. 2008 shows a core spectral index of -0.21 ± 0.03, while the spectral index increases in Aug. 2008 to -0.71 ± 0.03.
The spectral index of 0625-354 (Fig. 5.35) remains almost constant between Feb. and Nov. 2008 at $\sim$ -0.5.
At 1104-445 (Fig. 5.36) the spectral index map of Feb. 2008 shows a very steep spectral index for the core region and an optically thin jet. The spectral index -1.31$\pm$0.14 determined with the histogram (Fig. A.8) also corresponds to a very steep spectrum, which could result of a too low flux density in the K-band brightness distribution. The core region of the spectral index map of Nov. 2008 shows a strong gradient in spectral index. This can be explained with the different shapes of the jets in the brightness distributions of X- and K-band, indicating imaging artefacts.
For 1323-526 (Fig. 5.37) three dual-frequency epochs are available. However two of the epochs are with X-band images with very large beam. In each epoch, the region in the south of the core gets optically thin, showing the direction of the jet. This is consistent with the model-fitting analysis where also components in the south were found.
The spectral index maps of 2005-489 (Fig. 5.38) show the core and indications of the first component. The first component is optical thin, while it is seen, that the core gets optical thick in the east north east. In the range of their errors also both average spectral indices of the core are consistent.
The spectral index of the core of 2052-474 (Fig. 5.39) seems to be evenly distributed in every epoch. The spectral index decreases with time. While the flux density increases in the K-band, it remains at the same level in the X-band. Compared with the flux densities of the observations with ATCA from the TANAMI associated program C1730 (PI: *P. Edwards*; Tingay et al. (2009)) the same tendency is seen there. The higher frequencies vary stronger than the 8.64 GHz observation.
Fig. 5.40 shows the core and jet structure of 2326-477. In both epochs the regions of the two components show optical thin spectral indices while the core seems to be optical thick at this object.

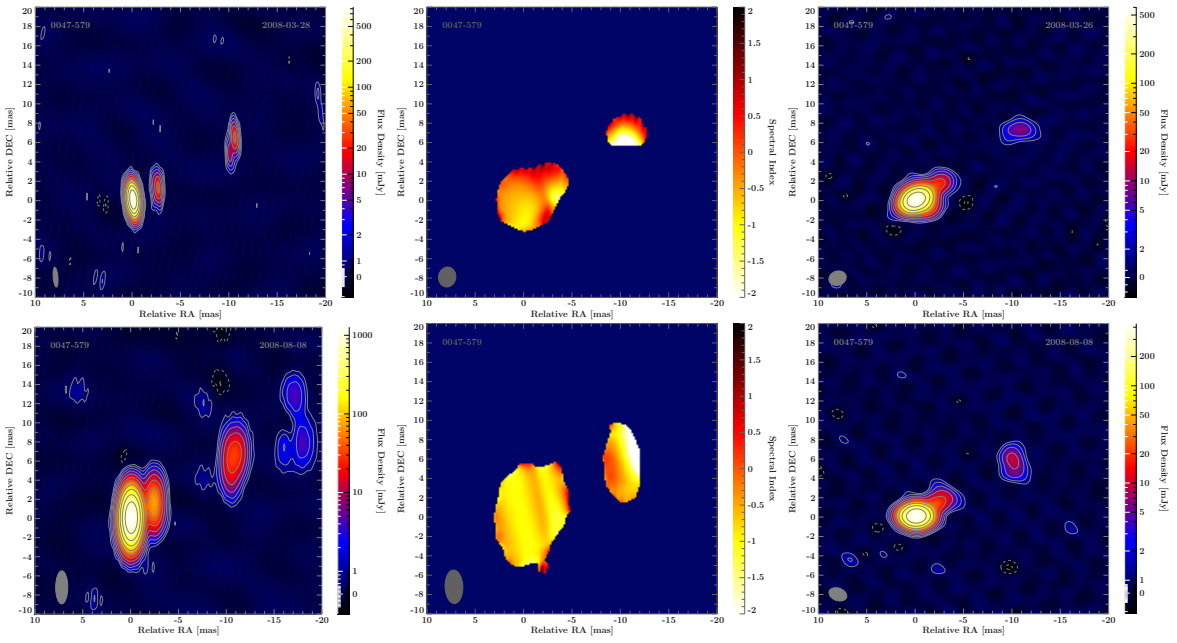

Figure 5.33.: Spectral index maps 0047-579 for the observations of Mar. 2008 (top) and Aug. 2008 (bottom). The left image shows the brightness distribution of the X-band (8.4 GHz) with a color scale for the flux density, the right image shows the brightness distribution of the K-band (22.3 GHz) with a color scale for the flux density. The mid image is the spectral index map, where the blue background represents no emission above the 3σ rms noise level and the color scale is for the spectral index. In the left corner of each image the beam of the image is presented.

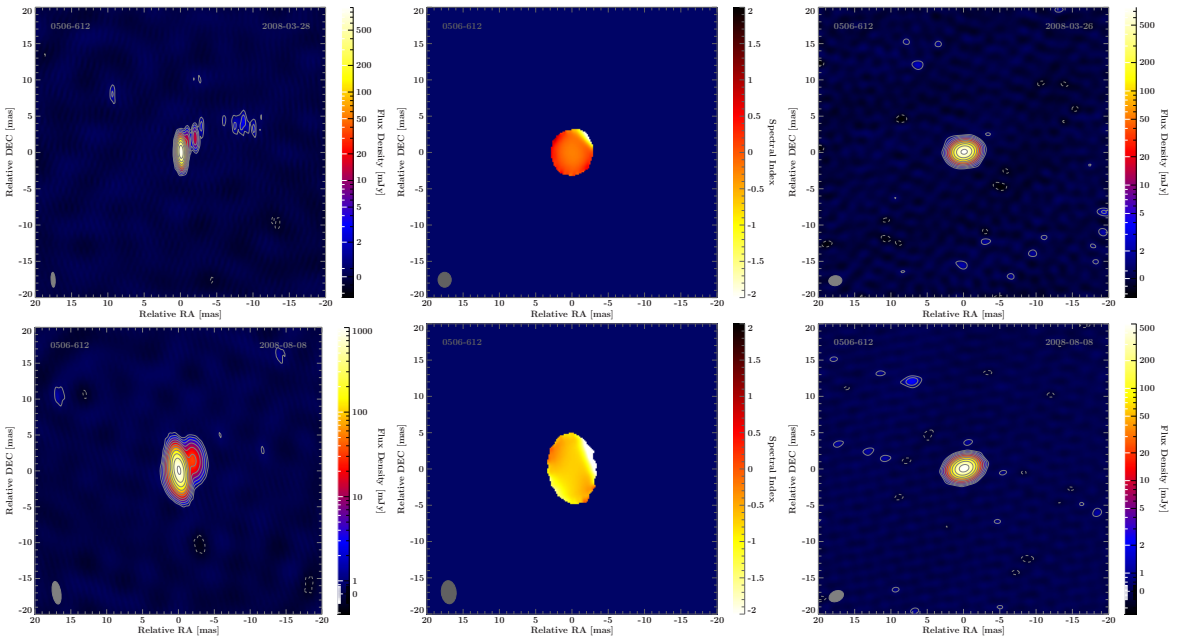

Figure 5.34.: Spectral index maps 0506-612 for the observations of Mar. 2008 (top) and Aug. 2008 (bottom) with the same concept like in Fig. 5.33.

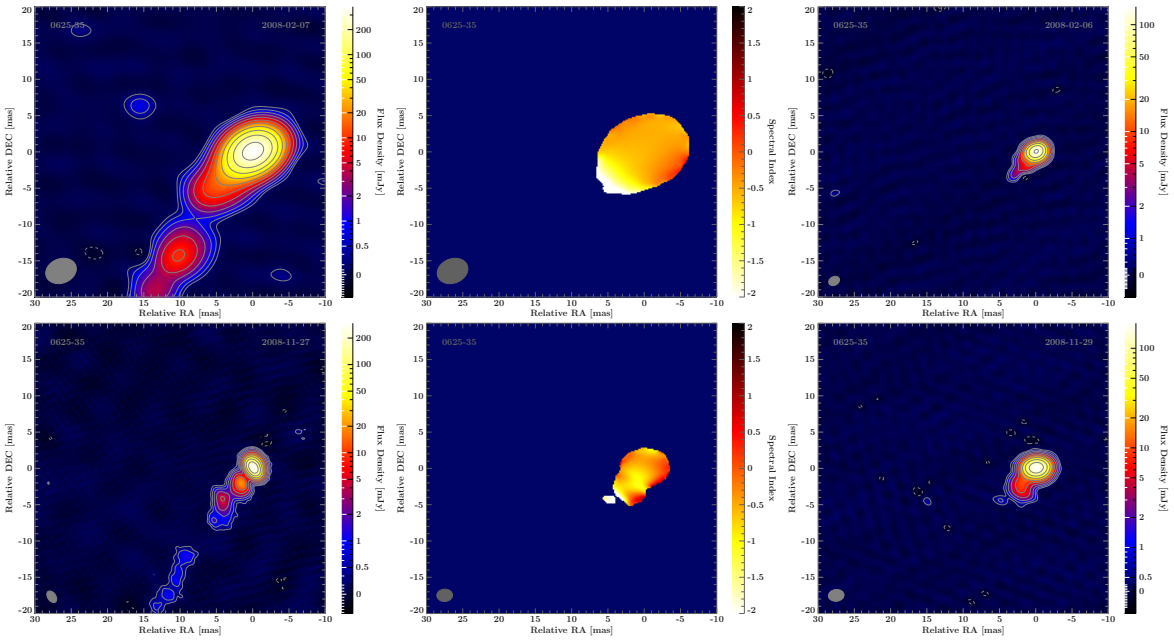

Figure 5.35.: Spectral index maps 0625-354 for the observations of Feb. 2008 (top) and Nov. 2008 (bottom) with the same concept like in Fig. 5.33.

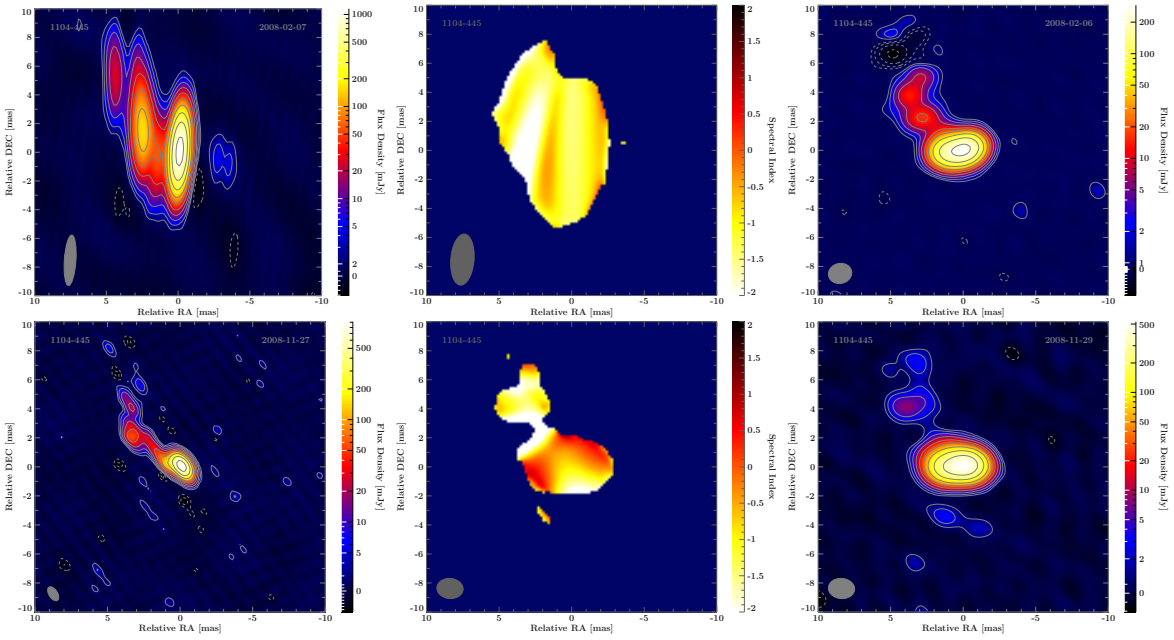

Figure 5.36.: Spectral index maps 1104-445 for the observations of Feb. 2008 (top) and Nov. 2008 (bottom) with the same concept like in Fig. 5.33.

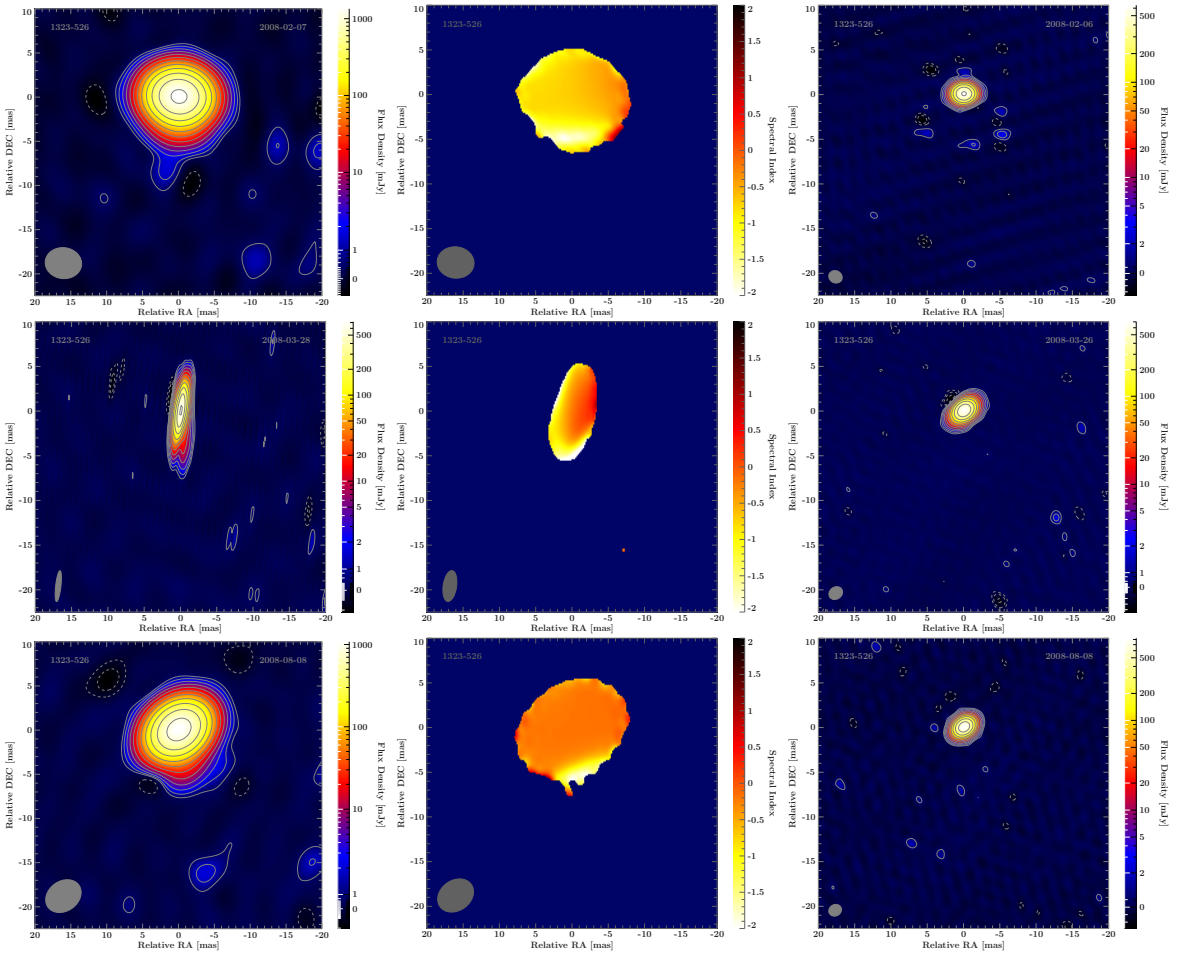

Figure 5.37.: Spectral index maps 1323-526 for the observations of Feb. 2008 (top), Mar. 2008 (mid) and Aug. 2008 (bottom) with the same concept like in Fig. 5.33.

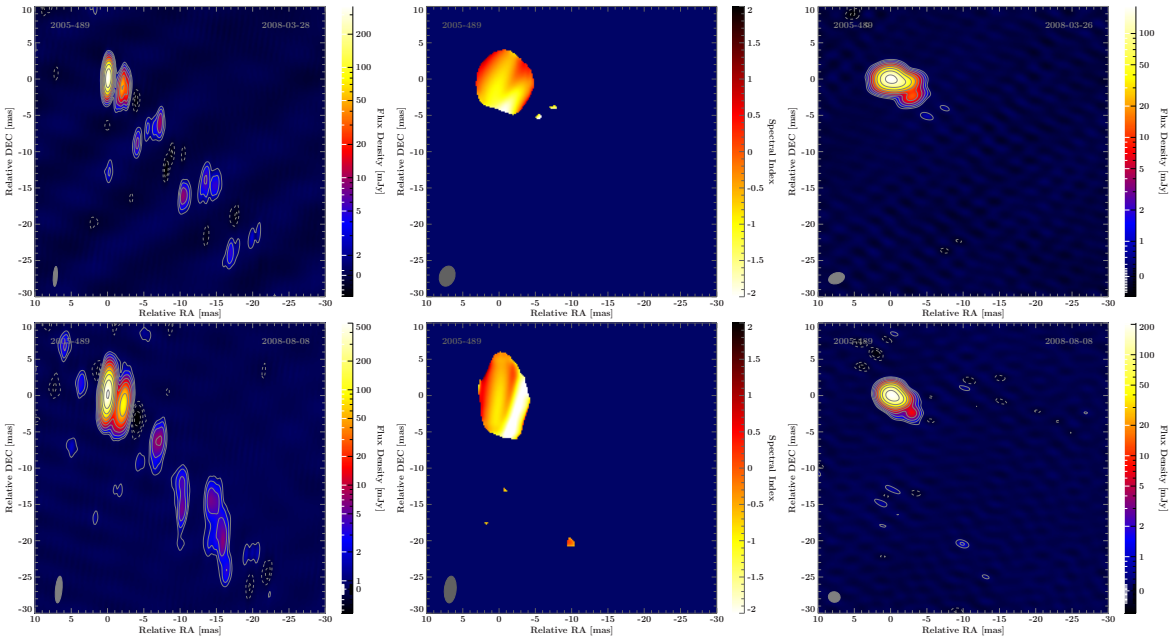

Figure 5.38.: Spectral index maps 2005-489 for the observations of Mar. 2008 (top) and Aug. 2008 (bottom) with the same concept like in Fig. 5.33.

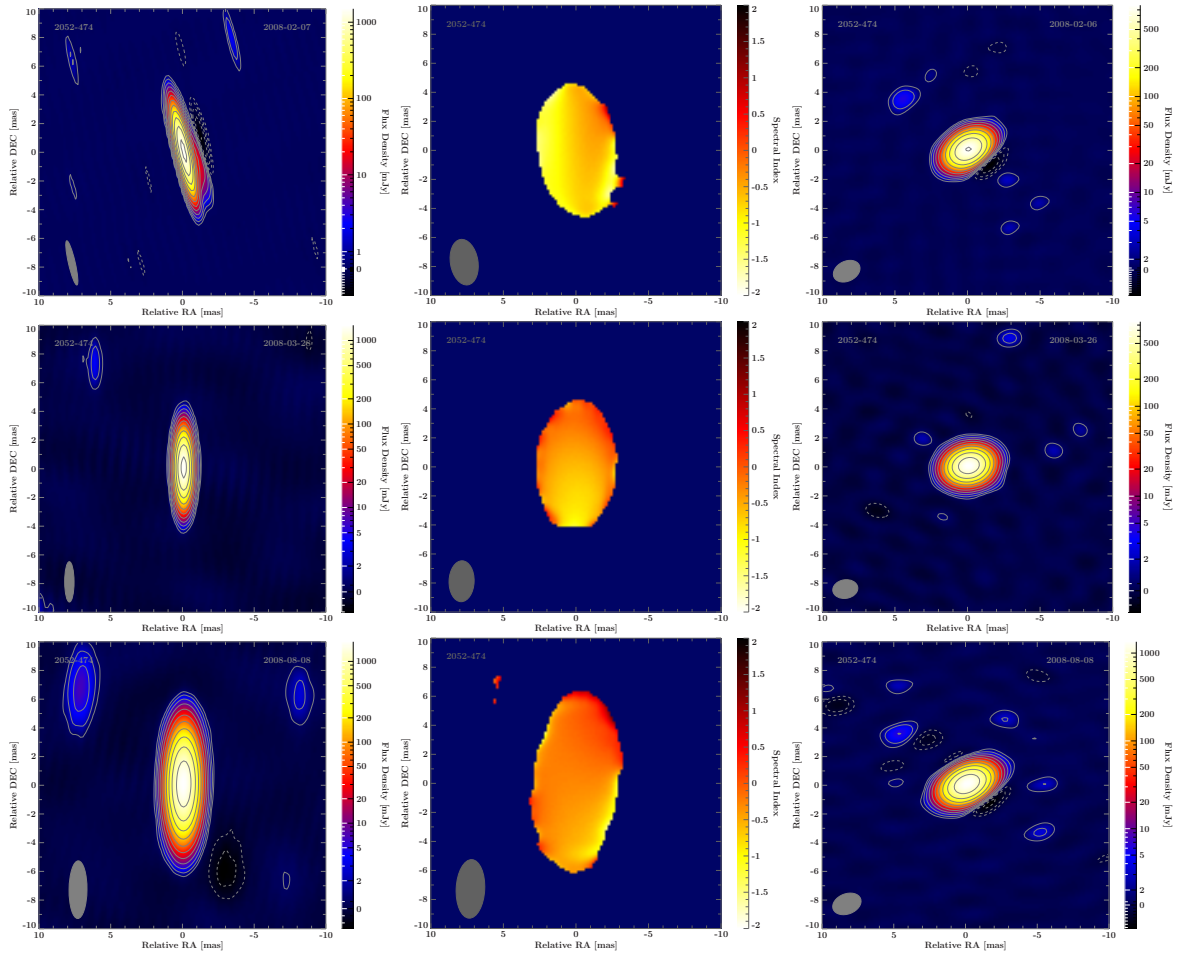

Figure 5.39.: Spectral index maps 2052-474 for the observations of Feb. 2008 (top), Mar. 2008 (mid) and Aug. 2008 (bottom) with the same concept like in Fig. 5.33.

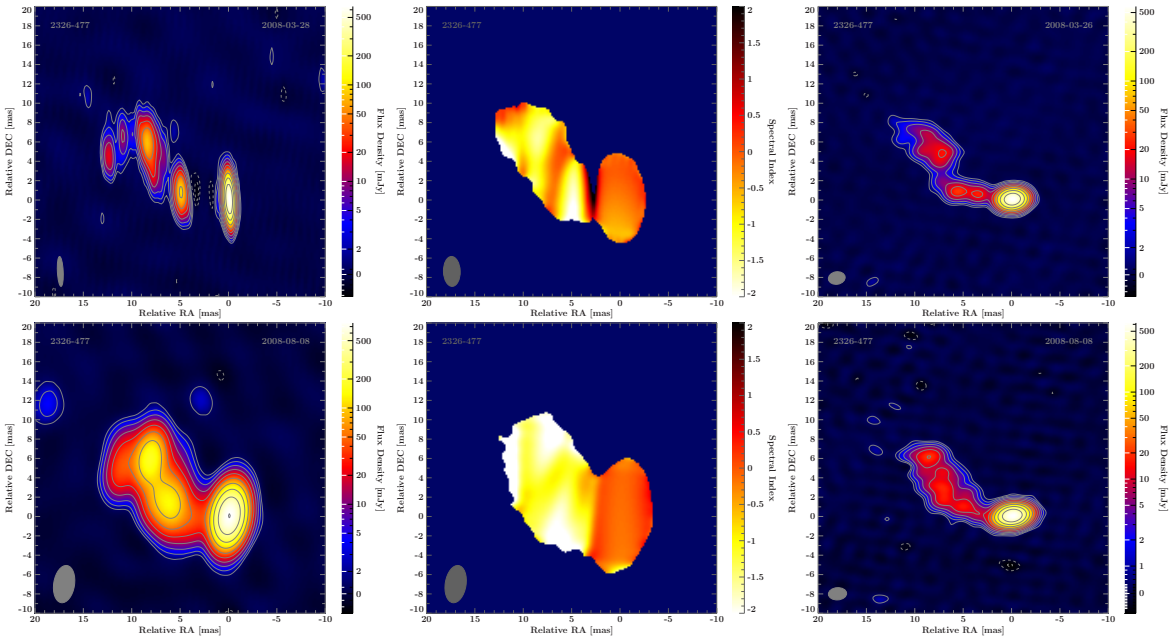

Figure 5.40.: Spectral index maps 2326-477 for the observations of Mar. 2008 (top) and Aug. 2008 (bottom) with the same concept like in Fig. 5.33.

6. Conclusion & Outlook

This work is an analysis of radio data of a sample of extragalactic jets from the TANAMI project over multiple epochs for the first time. The results in this work are consistent with the first epoch results published in the first TANAMI paper (Ojha et al. 2010). Additionally to the multi-epoch imaging results, the images of K-band observations and the evolution of flux densities, the kinematic properties of individual sources could be studied. The first time dependent spectral index maps for these sources were presented with the possibility to determine the mean spectral index of the core region.
The spectral indices were measured with two methods, histograms of the core region in the spectral index maps and calculating the spectral index from the circular Gaussian model core components. In the comparison both methods are consistent in the range of their uncertainties. In the range of their errors all spectral indices of the cores in the sample of this work are between -1 to 0. The spectral index maps mostly show only the core, because the jets were not detected in the K-band data. The jets in the spectral index maps show a steep spectral index, indicating that these regions are optically thin. The brightness temperatures in the X-band are in the range from 10^{10} - 10^{12} K and in the K-band in the range from 10^{8} - 10^{11} K. With exception of the two low-redshift sources, a radio galaxy and a blazar, the other sources have luminosities in the range of 10^{27} - 10^{28} W Hz^{-1}. The two exception are at values of about 10^{24} W Hz^{-1}. The values are on the same level in their observation epochs and are consistent with the first epoch values of Ojha et al. (2010).
The *model-fitting* for the X-band observations led to consistent jet models in six of the eight sources, giving the possibility to determine their apparent velocities. However most sources have large uncertainties for the velocities resulting from the linear regression in the date-distance plots. The jet of 0625-354 with a mean apparent velocity of $(2.92 \pm 0.44)c$ and the jet of 1104-445 have a component with excellent quality. The flux density of the most components in this work show the expected tendency to decrease over time. Future works can show which method to determine the spectral index, is more precise. Also the classification of 0625-354 is unclear, being classified as LINER, BL Lac or radio galaxy from different perspectives. The velocity of 1104-445 has to be verified with more observation epochs too.
TANAMI is an ongoing program monitoring AGN. The newer epochs of the sources treated in this thesis will fortify the models and increase the precision of the determination in the kinematic studies. Also other sources will have enough observations to study their properties. These results can contribute to the statistical properties of certain source types in the whole sample and AGN in general.

A. Additional Images and Plots

A.1. Tapered images

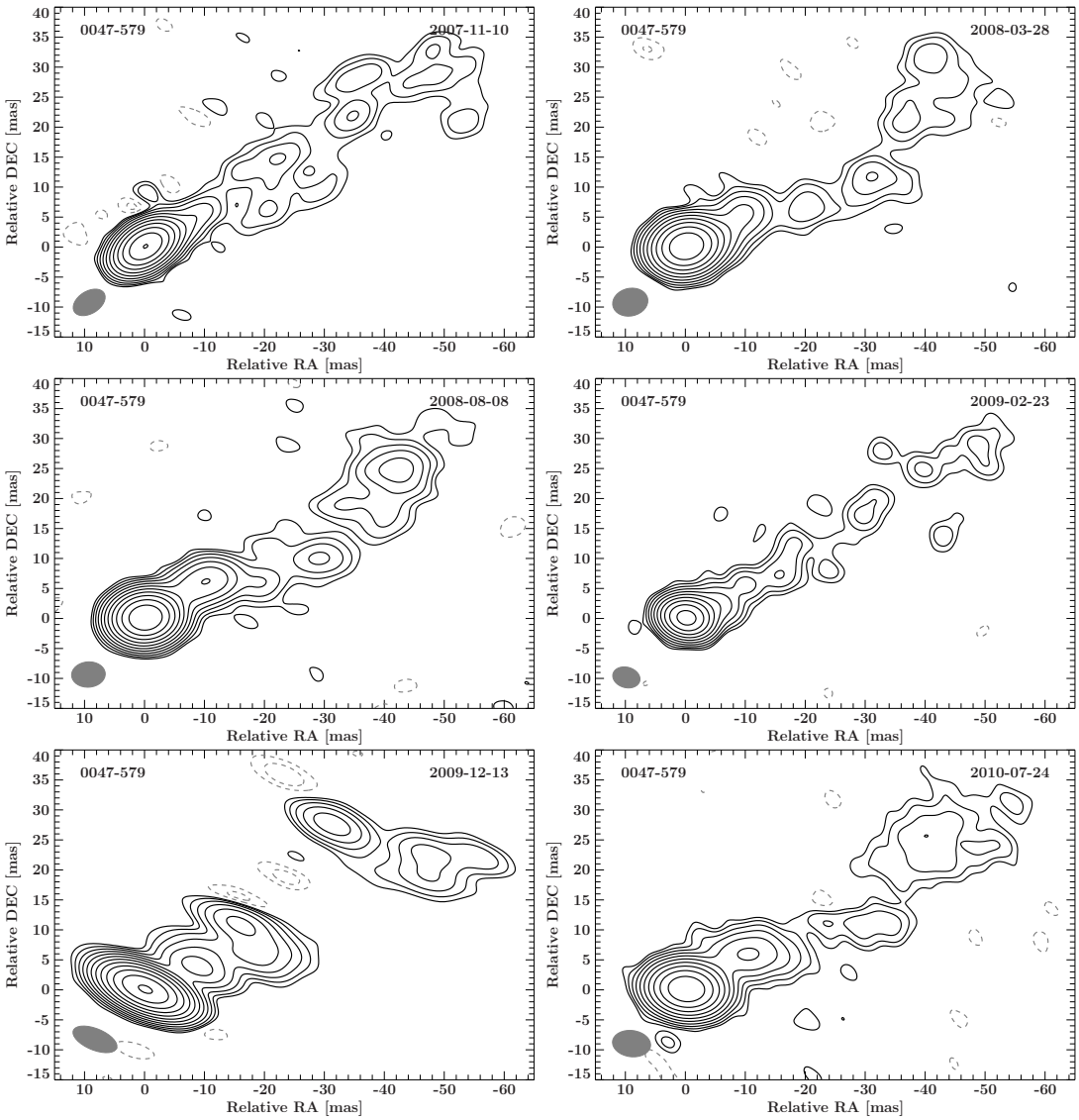

Figure A.1.: Tapered image maps 0047-579 in the X-Band (8.4 GHz) over six epochs.

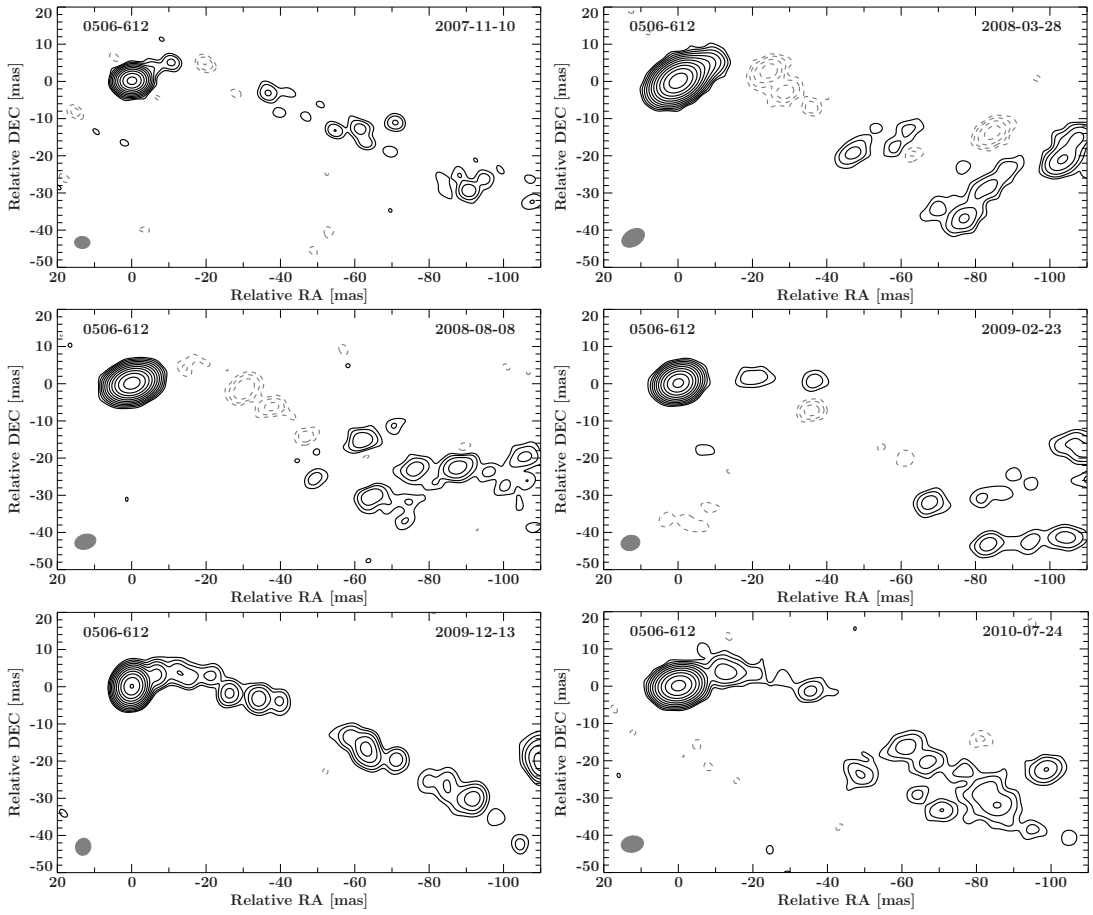

Figure A.2.: Tapered image maps 0506-612 in the X-Band (8.4 GHz) over six epochs.

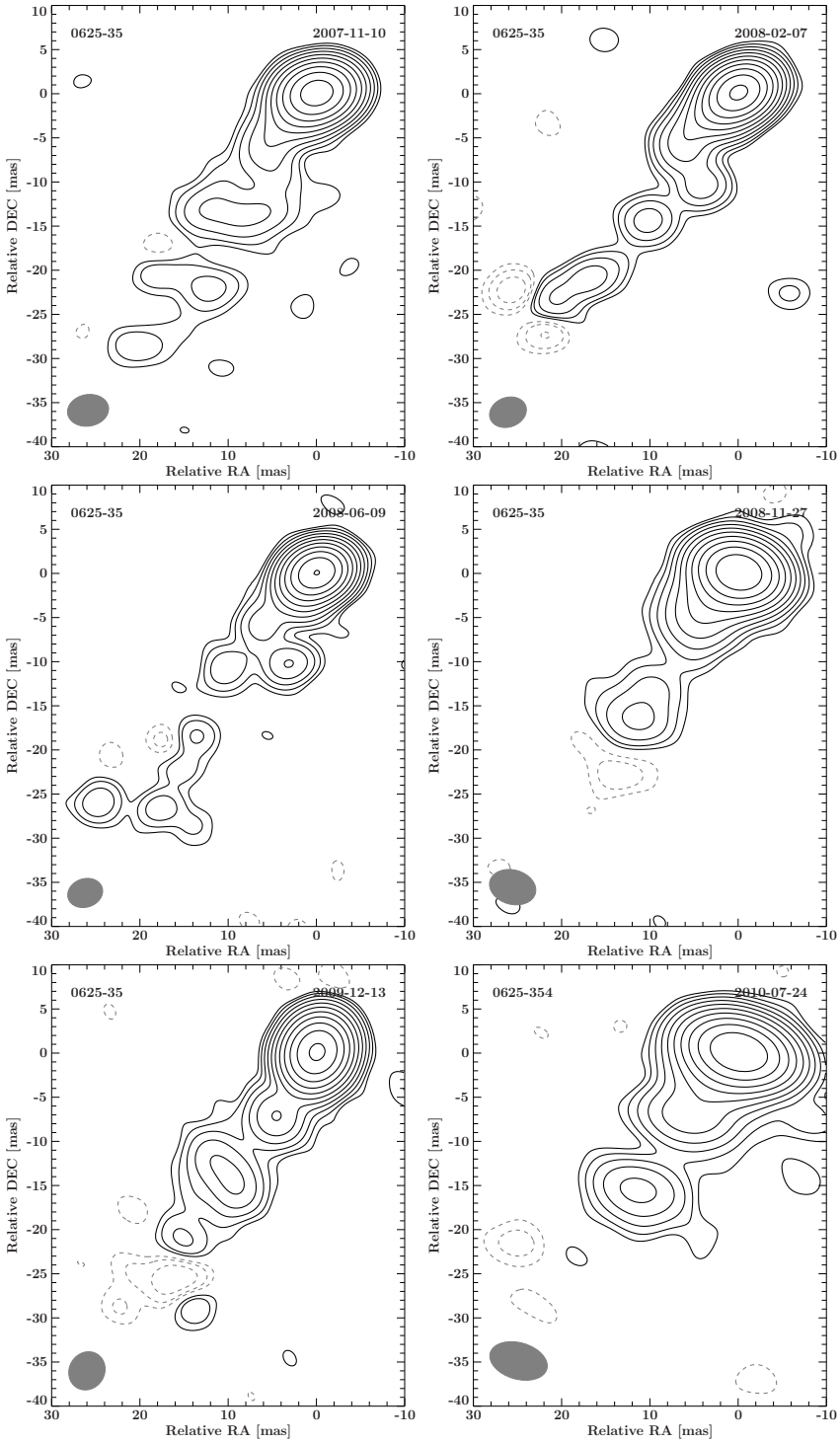

Figure A.3.: Tapered image maps 0625-354 in the X-Band (8.4 GHz) over six epochs.

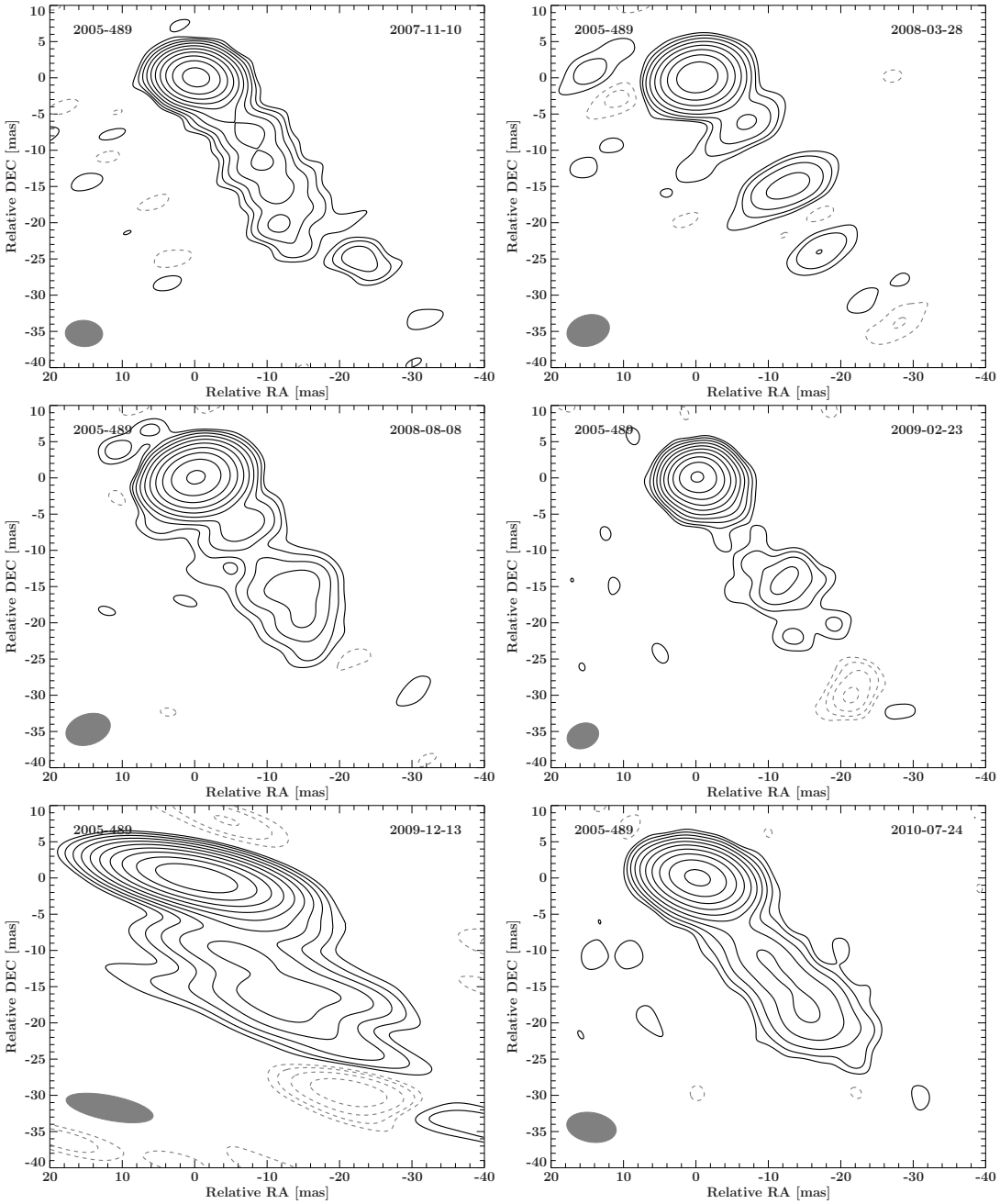

Figure A.4.: Tapered image maps 2005-489 in the X-Band (8.4 GHz) over six epochs.

A.2. Model-fit parameters

Table A.1.: Model-fit parameters for 0047-579 and 0506-612 (X-band)

Source	Epoch (date)	Comp.	Flux (Jy)	Distance (mas)	Angle °	FHWM (mas)	T_b (K)
0047-579	2007-11-10	1	0.111	2.819	-64.87	1.267	$3.40 \cdot 10^{09}$
0047-579	2007-11-10	2	0.022	12.016	-61.29	1.015	$1.05 \cdot 10^{09}$
0047-579	2007-11-10	3	0.068	35.224	-63.99	8.434	$4.70 \cdot 10^{07}$
0047-579	2007-11-10	core	1.223	0.022	19.04	0.462	$2.82 \cdot 10^{11}$
0047-579	2008-03-28	1	0.051	2.424	-65.97	0.516	$9.31 \cdot 10^{09}$
0047-579	2008-03-28	2	0.056	11.811	-60.35	1.758	$8.96 \cdot 10^{08}$
0047-579	2008-03-28	4	0.065	43.580	-59.47	15.133	$1.40 \cdot 10^{07}$
0047-579	2008-03-28	core	1.289	0.031	-27.11	0.487	$2.67 \cdot 10^{11}$
0047-579	2008-08-08	1	0.079	2.670	-52.90	0.803	$5.96 \cdot 10^{09}$
0047-579	2008-08-08	2	0.060	12.386	-58.68	2.725	$3.96 \cdot 10^{08}$
0047-579	2008-08-08	3	0.018	25.354	-66.69	2.963	$1.02 \cdot 10^{08}$
0047-579	2008-08-08	4	0.052	46.386	-59.81	9.437	$2.84 \cdot 10^{07}$
0047-579	2008-08-08	core	1.353	0.011	-167.96	0.391	$4.34 \cdot 10^{11}$
0047-579	2009-02-23	1	0.082	2.759	-54.20	0.612	$1.07 \cdot 10^{10}$
0047-579	2009-02-23	2	0.051	11.794	-58.96	3.115	$2.56 \cdot 10^{08}$
0047-579	2009-02-23	4	0.033	46.394	-58.02	3.547	$1.27 \cdot 10^{08}$
0047-579	2009-02-23	core	0.925	0.019	150.86	0.508	$1.75 \cdot 10^{11}$
0047-579	2009-12-13	1	0.029	3.122	-87.80	0.281	$1.79 \cdot 10^{10}$
0047-579	2009-12-13	2	0.073	12.339	-56.30	3.060	$3.83 \cdot 10^{08}$
0047-579	2009-12-13	4	0.051	47.412	-60.75	12.570	$1.59 \cdot 10^{07}$
0047-579	2009-12-13	core	1.296	0.023	78.51	0.684	$1.35 \cdot 10^{11}$
0047-579	2010-07-24	1	0.087	2.521	-66.40	0.532	$1.50 \cdot 10^{10}$
0047-579	2010-07-24	2	0.054	12.589	-62.10	3.573	$2.09 \cdot 10^{08}$
0047-579	2010-07-24	4	0.049	45.906	-59.00	10.790	$2.07 \cdot 10^{07}$
0047-579	2010-07-24	core	0.961	0.051	150.75	0.580	$1.40 \cdot 10^{11}$
0506-612	2007-11-10	1	0.069	2.029	-55.77	0.425	$1.41 \cdot 10^{10}$
0506-612	2007-11-10	core	0.859	0.005	160.42	0.173	$1.06 \cdot 10^{12}$
0506-612	2008-03-28	1	0.048	2.476	-46.70	2.213	$3.58 \cdot 10^{08}$
0506-612	2008-03-28	core	1.036	0.004	152.11	0.284	$4.72 \cdot 10^{11}$
0506-612	2008-08-08	1	0.056	2.588	-55.64	0.295	$2.37 \cdot 10^{10}$
0506-612	2008-08-08	core	1.081	0.028	165.46	0.372	$2.86 \cdot 10^{11}$
0506-612	2009-02-23	1	0.062	3.059	-53.53	0.240	$3.94 \cdot 10^{10}$
0506-612	2009-02-23	core	0.833	0.087	80.01	0.368	$2.25 \cdot 10^{11}$
0506-612	2009-12-13	1	0.050	2.648	-29.39	0.250	$2.96 \cdot 10^{10}$
0506-612	2009-12-13	core	0.855	0.031	124.38	0.488	$1.31 \cdot 10^{11}$
0506-612	2010-07-24	1	0.034	3.042	-48.79	0.167	$4.47 \cdot 10^{10}$
0506-612	2010-07-24	core	0.772	0.018	156.32	0.531	$1.00 \cdot 10^{11}$

Table A.2.: Model-fit parameters for 0625-354, 1104-445 and 1323-526 (X-band)

Source	Epoch (date)	Comp.	Flux (Jy)	Distance (mas)	Angle °	FHWM (mas)	T_b (K)
0625-354	2007-11-10	1	0.049	2.032	141.07	1.715	$3.08 \cdot 10^{08}$
0625-354	2007-11-10	2	0.007	5.696	141.51	2.036	$3.24 \cdot 10^{07}$
0625-354	2007-11-10	3	0.014	15.953	149.40	4.332	$1.42 \cdot 10^{07}$
0625-354	2007-11-10	core	0.280	0.063	-1.07	0.175	$1.70 \cdot 10^{11}$
0625-354	2008-02-07	1	0.066	2.513	132.60	1.639	$4.56 \cdot 10^{08}$
0625-354	2008-02-07	2	0.003	5.887	132.63	0.977	$6.48 \cdot 10^{07}$
0625-354	2008-02-07	3	0.018	17.090	144.62	2.955	$3.76 \cdot 10^{07}$
0625-354	2008-02-07	core	0.368	0.139	-32.92	0.629	$1.72 \cdot 10^{10}$
0625-354	2008-06-09	1	0.042	2.782	141.97	0.905	$9.58 \cdot 10^{08}$
0625-354	2008-06-09	2	0.018	6.568	139.29	0.423	$1.89 \cdot 10^{09}$
0625-354	2008-06-09	3	0.014	18.075	145.91	4.775	$1.14 \cdot 10^{07}$
0625-354	2008-06-09	core	0.371	0.044	-1.54	0.177	$2.19 \cdot 10^{11}$
0625-354	2008-11-27	1	0.037	2.762	140.71	0.429	$3.73 \cdot 10^{09}$
0625-354	2008-11-27	2	0.013	6.326	141.01	0.340	$2.02 \cdot 10^{09}$
0625-354	2008-11-27	3	0.008	18.724	143.18	7.291	$2.73 \cdot 10^{06}$
0625-354	2008-11-27	core	0.342	0.060	4.63	0.422	$3.54 \cdot 10^{10}$
0625-354	2009-12-13	1	0.030	2.451	156.68	0.416	$3.23 \cdot 10^{09}$
0625-354	2009-12-13	2	0.008	8.501	147.25	0.454	$6.96 \cdot 10^{08}$
0625-354	2009-12-13	3	0.018	19.724	141.15	6.159	$8.82 \cdot 10^{06}$
0625-354	2009-12-13	core	0.320	0.078	-16.29	0.346	$4.94 \cdot 10^{10}$
0625-354	2010-07-24	1	0.023	3.161	137.54	0.508	$1.61 \cdot 10^{09}$
0625-354	2010-07-24	2	0.014	8.096	141.47	3.662	$1.87 \cdot 10^{07}$
0625-354	2010-07-24	3	0.008	19.473	143.36	2.851	$1.91 \cdot 10^{07}$
0625-354	2010-07-24	core	0.309	0.066	-7.00	0.476	$2.51 \cdot 10^{10}$
1104-445	2007-11-10	1	0.172	3.057	57.10	1.031	$7.41 \cdot 10^{09}$
1104-445	2007-11-10	2	0.040	5.817	29.21	0.528	$6.59 \cdot 10^{09}$
1104-445	2007-11-10	core	1.131	0.026	-177.87	0.342	$4.41 \cdot 10^{11}$
1104-445	2008-02-07	1	0.239	2.639	70.65	1.168	$8.02 \cdot 10^{09}$
1104-445	2008-02-07	2	0.078	4.786	41.52	0.423	$1.98 \cdot 10^{10}$
1104-445	2008-02-07	core	1.309	0.106	102.95	0.357	$4.69 \cdot 10^{11}$
1104-445	2008-06-09	1	0.182	3.112	63.61	0.804	$1.29 \cdot 10^{10}$
1104-445	2008-06-09	2	0.069	5.735	33.82	0.966	$3.38 \cdot 10^{09}$
1104-445	2008-06-09	core	1.257	0.035	118.08	0.336	$5.09 \cdot 10^{11}$
1104-445	2008-11-27	1	0.166	3.575	56.28	0.556	$2.44 \cdot 10^{10}$
1104-445	2008-11-27	2	0.038	5.243	35.69	0.531	$6.07 \cdot 10^{09}$
1104-445	2008-11-27	core	1.425	0.020	-170.37	0.502	$2.57 \cdot 10^{11}$
1104-445	2009-12-13	1	0.094	4.859	49.81	0.441	$2.20 \cdot 10^{10}$
1104-445	2009-12-13	3	0.116	2.054	92.10	0.433	$2.82 \cdot 10^{10}$
1104-445	2009-12-13	core	1.368	0.044	83.31	0.554	$2.03 \cdot 10^{11}$
1104-445	2010-07-24	1	0.085	4.715	48.25	0.365	$2.88 \cdot 10^{10}$
1104-445	2010-07-24	3	0.223	2.169	80.56	0.545	$3.41 \cdot 10^{10}$
1104-445	2010-07-24	core	1.198	0.091	-132.10	0.543	$1.85 \cdot 10^{11}$
1323-526	2007-11-10	core	1.005	0.009	-171.83	0.130	$1.04 \cdot 10^{12}$
1323-526	2008-02-07	1	0.014	3.426	-178.96	1.352	$1.37 \cdot 10^{08}$
1323-526	2008-02-07	core	1.379	0.009	168.40	0.710	$4.80 \cdot 10^{10}$
1323-526	2008-03-28	core	1.018	0.002	-139.84	1.210	$1.22 \cdot 10^{10}$
1323-526	2008-08-08	core	1.111	0.011	98.46	0.716	$3.80 \cdot 10^{10}$
1323-526	2009-02-27	1	0.031	3.499	-176.58	0.593	$1.54 \cdot 10^{09}$
1323-526	2009-02-27	core	1.353	0.008	2.09	0.463	$1.11 \cdot 10^{11}$
1323-526	2010-03-12	1	0.054	2.633	-179.11	1.193	$6.66 \cdot 10^{08}$
1323-526	2010-03-12	core	0.731	0.050	-18.46	0.367	$9.49 \cdot 10^{10}$

Table A.3.: Model-fit parameters for 2005-489, 2052-474 and 2326-477 (X-band)

Source	Epoch (date)	Comp.	Flux (Jy)	Distance (mas)	Angle °	FHWM (mas)	T_b (K)
2005-489	2007-11-10	1	0.296	0.918	-125.30	0.531	$1.98 \cdot 10^{10}$
2005-489	2007-11-10	2	0.089	13.874	-137.16	14.810	$7.67 \cdot 10^{06}$
2005-489	2007-11-10	core	0.255	0.587	36.94	0.367	$3.56 \cdot 10^{10}$
2005-489	2008-03-28	1	0.141	2.273	-118.00	0.505	$1.04 \cdot 10^{10}$
2005-489	2008-03-28	2	0.017	10.815	-138.50	3.030	$3.53 \cdot 10^{07}$
2005-489	2008-03-28	3	0.038	20.812	-141.24	5.113	$2.71 \cdot 10^{07}$
2005-489	2008-03-28	core	0.479	0.127	-49.64	0.548	$3.00 \cdot 10^{10}$
2005-489	2008-08-08	1	0.205	1.901	-120.25	0.558	$1.24 \cdot 10^{10}$
2005-489	2008-08-08	2	0.020	10.087	-140.63	2.910	$4.36 \cdot 10^{07}$
2005-489	2008-08-08	3	0.043	21.842	-139.69	8.593	$1.09 \cdot 10^{07}$
2005-489	2008-08-08	core	0.533	0.299	42.92	0.594	$2.83 \cdot 10^{10}$
2005-489	2009-02-23	1	0.290	1.835	-127.02	2.229	$1.10 \cdot 10^{09}$
2005-489	2009-02-23	3	0.038	18.748	-140.22	3.674	$5.33 \cdot 10^{07}$
2005-489	2009-02-23	core	0.440	0.297	39.55	0.497	$3.33 \cdot 10^{10}$
2005-489	2009-12-13	1	0.076	3.383	-124.59	0.385	$9.59 \cdot 10^{09}$
2005-489	2009-12-13	2	0.054	14.923	-141.31	4.358	$5.32 \cdot 10^{07}$
2005-489	2009-12-13	3	0.032	27.821	-142.91	4.822	$2.58 \cdot 10^{07}$
2005-489	2009-12-13	core	0.501	0.061	-37.90	0.572	$2.86 \cdot 10^{10}$
2005-489	2010-07-24	1	0.183	1.866	-125.11	1.727	$1.15 \cdot 10^{09}$
2005-489	2010-07-24	2	0.033	13.375	-139.99	6.944	$1.29 \cdot 10^{07}$
2005-489	2010-07-24	3	0.036	24.910	-139.25	6.484	$1.59 \cdot 10^{07}$
2005-489	2010-07-24	core	0.357	0.263	37.14	0.451	$3.29 \cdot 10^{10}$
2052-474	2008-02-07	core	1.684	0.000	-166.79	0.229	$1.41 \cdot 10^{12}$
2052-474	2008-03-28	core	1.657	0.000	-159.67	0.269	$1.00 \cdot 10^{12}$
2052-474	2008-08-08	core	1.769	0.000	-0.47	0.220	$1.59 \cdot 10^{12}$
2052-474	2009-02-23	core	1.651	0.001	-154.24	0.456	$3.46 \cdot 10^{11}$
2052-474	2009-09-05	core	1.848	0.001	-16.83	0.499	$3.23 \cdot 10^{11}$
2052-474	2010-03-12	core	2.006	0.000	13.67	0.756	$1.53 \cdot 10^{11}$
2326-477	2007-11-10	1	0.144	5.444	82.51	0.480	$2.53 \cdot 10^{10}$
2326-477	2007-11-10	2	0.179	10.511	56.21	1.979	$1.84 \cdot 10^{09}$
2326-477	2007-11-10	core	0.608	0.285	95.52	0.281	$3.11 \cdot 10^{11}$
2326-477	2008-03-28	1	0.152	5.166	84.51	1.239	$4.00 \cdot 10^{09}$
2326-477	2008-03-28	2	0.250	10.648	56.78	2.585	$1.52 \cdot 10^{09}$
2326-477	2008-03-28	core	0.777	0.201	97.06	0.317	$3.13 \cdot 10^{11}$
2326-477	2008-08-08	1	0.217	6.144	79.73	1.747	$2.86 \cdot 10^{09}$
2326-477	2008-08-08	2	0.284	9.946	55.51	2.650	$1.63 \cdot 10^{09}$
2326-477	2008-08-08	core	0.795	0.049	121.24	0.309	$3.36 \cdot 10^{11}$
2326-477	2009-02-23	1	0.185	5.654	79.00	2.495	$1.20 \cdot 10^{09}$
2326-477	2009-02-23	2	0.246	9.797	56.10	3.217	$9.59 \cdot 10^{08}$
2326-477	2009-02-23	core	0.714	0.084	173.52	0.393	$1.87 \cdot 10^{11}$
2326-477	2009-12-13	1	0.054	6.519	86.42	0.386	$1.46 \cdot 10^{10}$
2326-477	2009-12-13	2	0.242	11.995	58.22	3.609	$7.49 \cdot 10^{08}$
2326-477	2009-12-13	core	1.313	0.733	76.03	0.406	$3.22 \cdot 10^{11}$
2326-477	2010-07-24	1	0.172	5.717	82.42	0.825	$1.02 \cdot 10^{10}$
2326-477	2010-07-24	2	0.284	10.217	56.13	3.522	$9.23 \cdot 10^{08}$
2326-477	2010-07-24	core	1.073	0.031	66.40	0.457	$2.07 \cdot 10^{11}$

Table A.4.: Model-fit parameters (K-band)

Source	Epoch (date)	Comp.	Flux (Jy)	Distance (mas)	Angle °	FHWM (mas)	T_b (K)
0047-479	2008-03-26	core	0.765	0.021	-61.04	0.783	$8.74 \cdot 10^{09}$
0047-479	2008-08-08	core	0.587	0.049	-63.49	0.828	$5.99 \cdot 10^{09}$
0506-612	2008-03-26	core	0.896	0.001	-100.26	0.605	$1.28 \cdot 10^{10}$
0506-612	2008-08-08	core	0.547	0.009	21.53	0.499	$1.15 \cdot 10^{10}$
0625-354	2008-02-06	core	0.235	0.020	-147.57	0.968	$6.62 \cdot 10^{08}$
0625-354	2008-11-29	core	0.209	0.046	164.47	0.717	$1.07 \cdot 10^{09}$
1104-445	2008-02-06	core	0.447	0.040	17.30	0.916	$3.46 \cdot 10^{09}$
1104-445	2008-11-29	core	0.768	0.055	113.05	0.935	$5.71 \cdot 10^{09}$
1323-526	2008-02-06	core	0.706	0.024	35.33	0.428	$9.67 \cdot 10^{09}$
1323-526	2008-03-26	core	0.773	0.007	-152.38	0.385	$1.30 \cdot 10^{10}$
1323-526	2008-08-08	core	0.928	0.004	-107.44	0.448	$1.16 \cdot 10^{10}$
2005-489	2008-03-26	core	0.301	0.173	-102.65	1.335	$4.53 \cdot 10^{08}$
2005-489	2008-08-08	core	0.365	0.141	-122.23	1.392	$5.05 \cdot 10^{08}$
2052-474	2008-02-06	core	0.898	0.000	-39.21	0.190	$1.55 \cdot 10^{11}$
2052-474	2008-03-26	core	0.971	0.000	-47.55	0.468	$2.77 \cdot 10^{10}$
2052-474	2008-08-08	core	1.370	0.000	44.80	0.140	$4.36 \cdot 10^{11}$
2326-477	2008-03-26	core	0.619	0.005	-31.29	0.344	$3.01 \cdot 10^{10}$
2326-477	2008-08-08	core	0.721	0.001	48.03	0.567	$1.29 \cdot 10^{10}$

A.3. Spectral index core region histograms

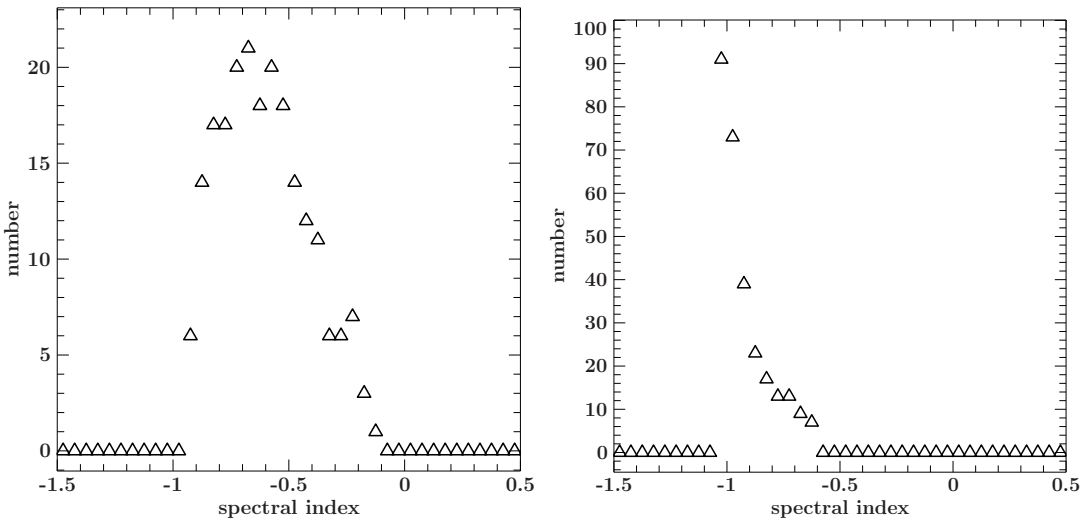

Figure A.5.: Histogram of the core region of 0047-579 with pixel counts of spectral indices in bins of 0.05.

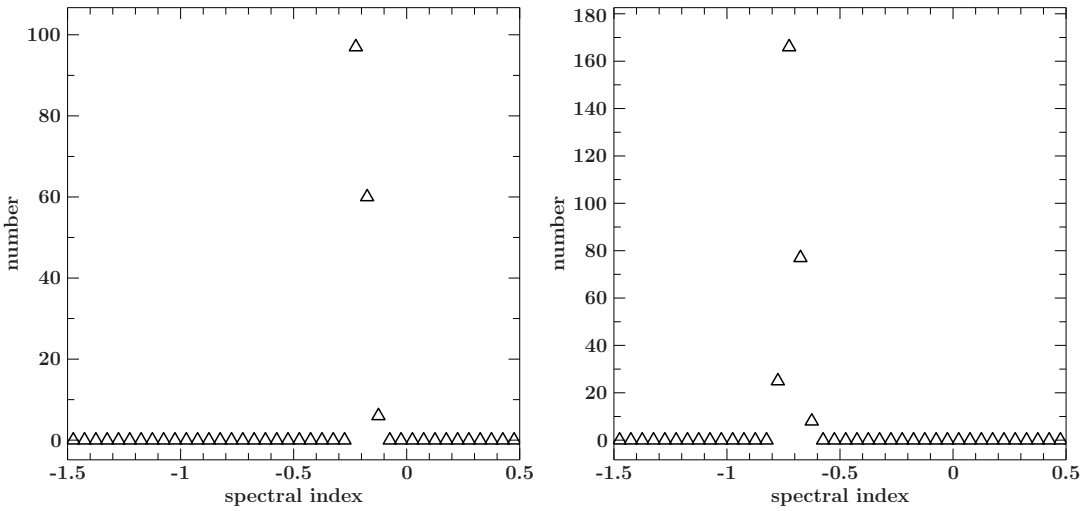

Figure A.6.: Histogram of the core region of 0506-6112 with pixel counts of spectral indices in bins of 0.05.

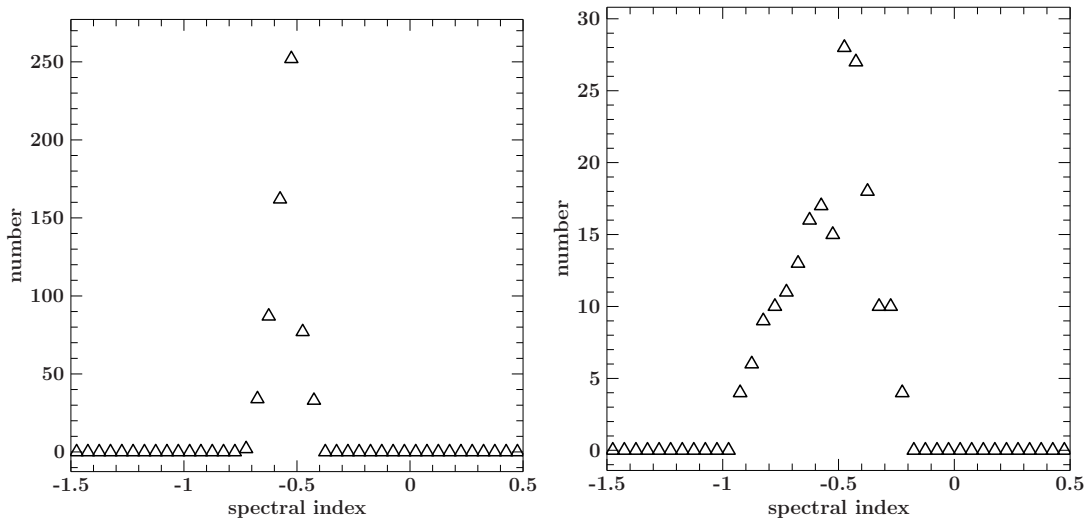

Figure A.7.: Histogram of the core region of 0625-354 with pixel counts of spectral indices in bins of 0.05.

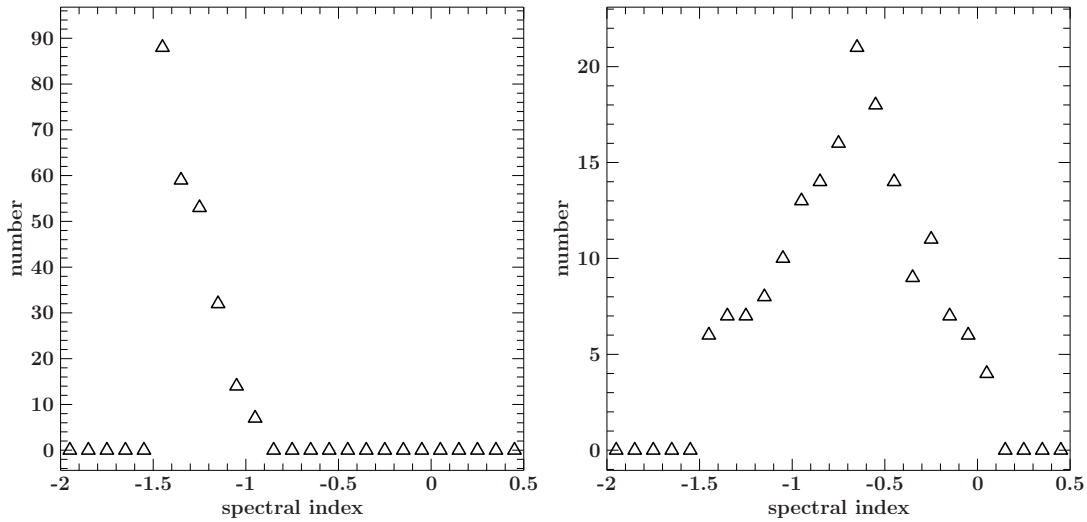

Figure A.8.: Histogram of the core region of 1104-445 with pixel counts of spectral indices in bins of 0.1.

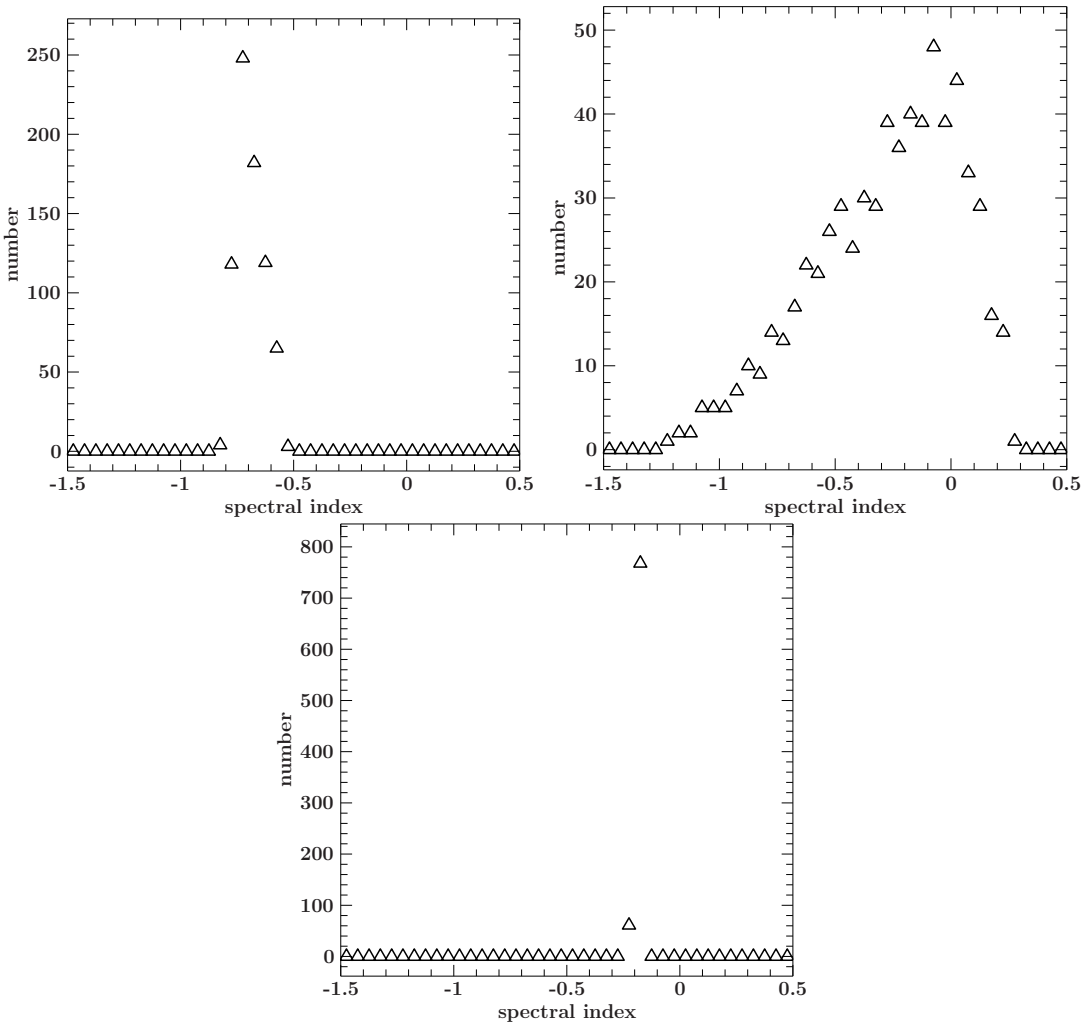

Figure A.9.: Histogram of the core region of 1323-526 with pixel counts of spectral indices in bins of 0.05.

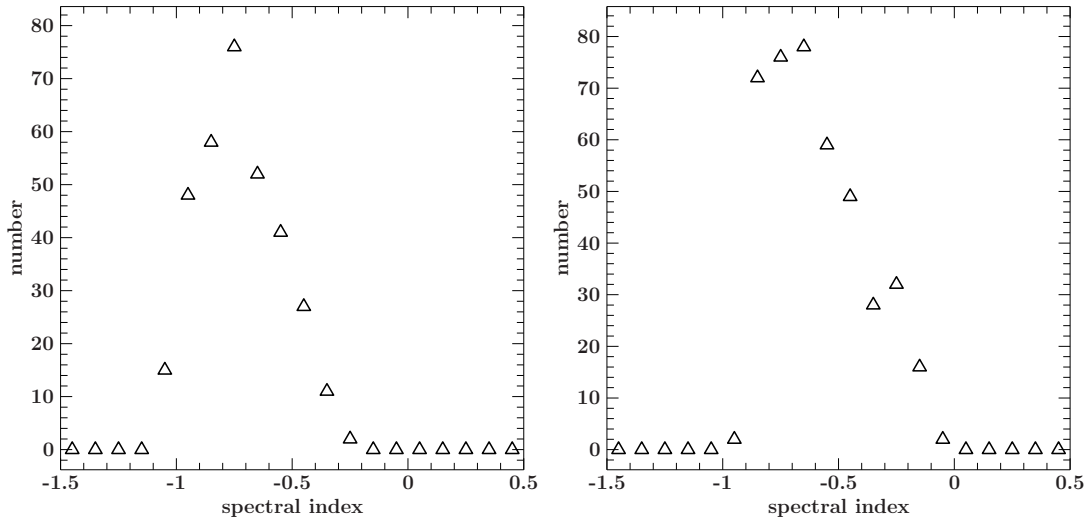

Figure A.10.: Histogram of the core region of 2005-489 with pixel counts of spectral indices in bins of 0.1.

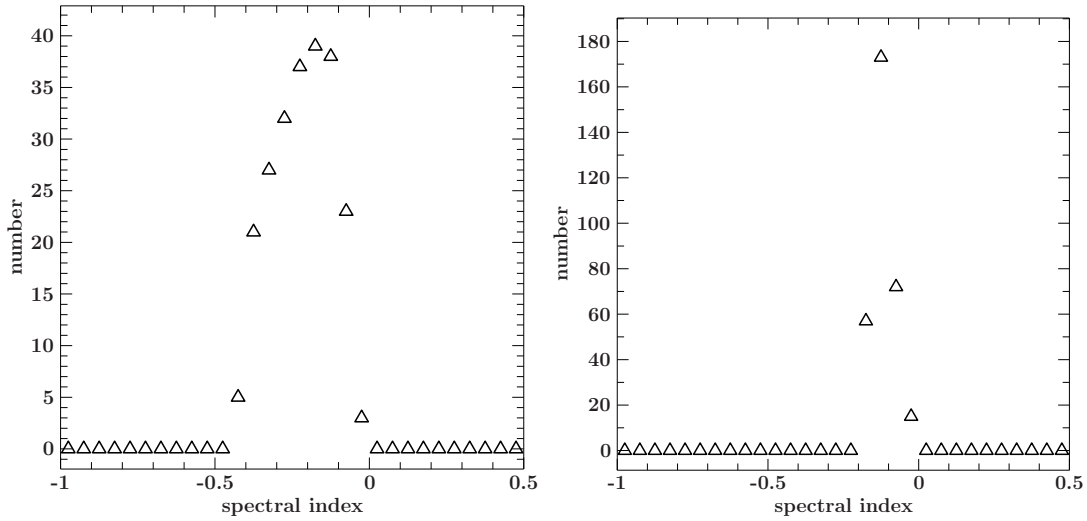

Figure A.11.: Histogram of the core region of 2326-477 with pixel counts of spectral indices in bins of 0.05.

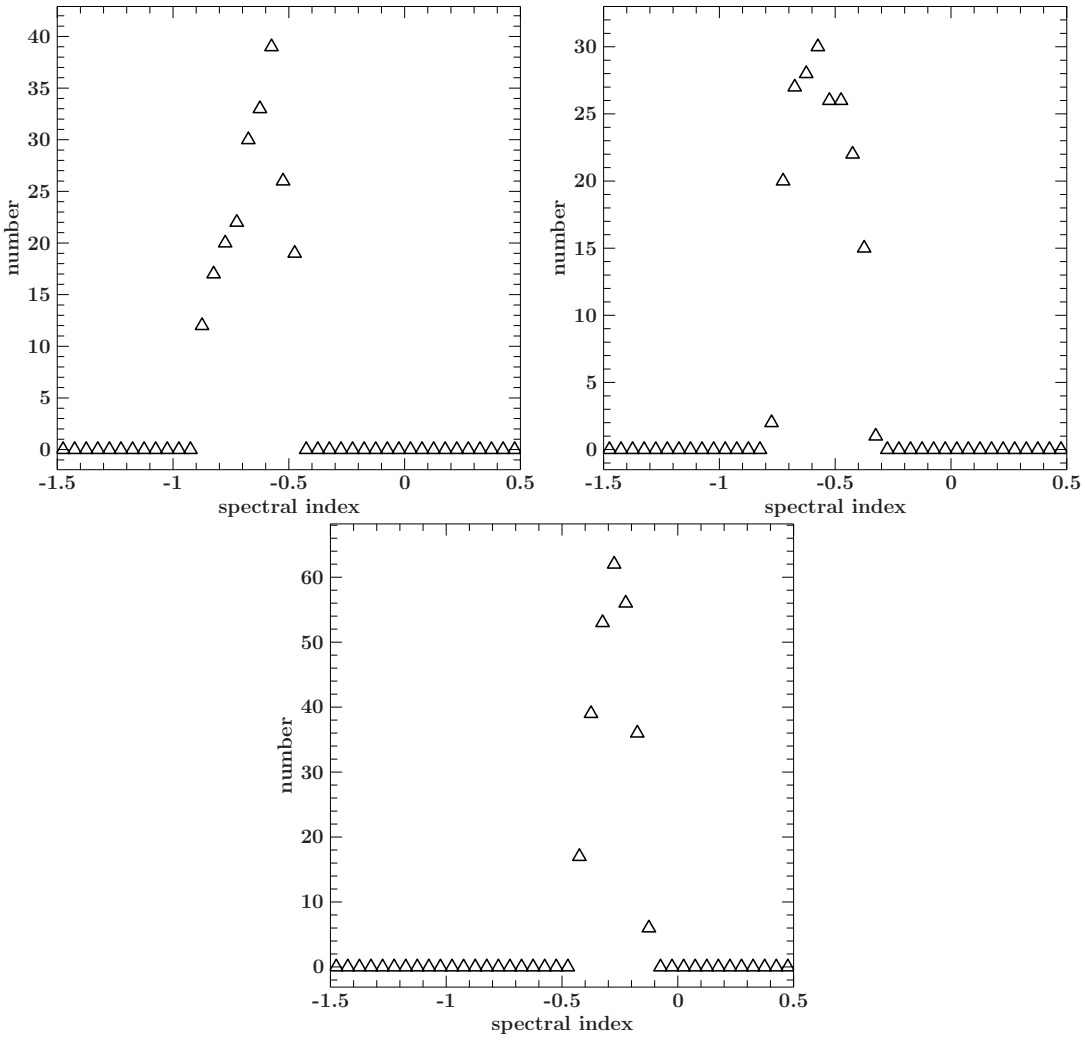

Figure A.12.: Histogram of the core region of 2052-474 with pixel counts of spectral indices in bins of 0.05.

List of Figures

List of Tables

Bibliography

Abdo A.A., Ackermann M., Ajello M., et al., 2010a, VizieR Online Data Catalog 218, 80405

Abdo A.A., Ackermann M., Ajello M., et al., 2010b, ApJS 188, 405

Abdo A.A., Ackermann M., Ajello M., et al., 2010c, ApJ 722, 520

Aharonian F., Akhperjanian A.G., Aye K.M., et al., 2005 436, L17

Antonucci R., 1993, ARA&A 31, 473

Arshakian T.G., León-Tavares J., Böttcher M., et al., 2012 537, A32

Atwood W.B., Abdo A.A., Ackermann M., et al., 2009, ApJ 697, 1071

Bevington P.R., Robinson D.K., 2003, Data reduction and error analysis for the physical sciences

Bignall H., Cimo G., Jauncey D., et al., 2008, ArXiv e-prints

Blanchard J.M., Lovell J.E.J., Ojha R., et al., 2012 538, A150

Boeck M., Kadler M., Tosti G., et al., 2009, ArXiv e-prints

Bridle A.H., Perley R.A., 1984, ARA&A 22, 319

Brinkmann W., Siebert J., Boller T., 1994 281, 355

Burke B.F., Graham-Smith F., 2010, An Introduction to Radio Astronomy, Cambridge University Press

Burrows D.N., Hill J.E., Nousek J.A., et al., 2005, Space Sci. Rev. 120, 165

Böck M., 2012, Ph.D. thesis, University of Erlangen-Nuremburg

Deller A.T., Tingay S.J., Bailes M., West C., 2007, PASP 119, 318

Diamond P.J., 1995, In: Zensus J.A., Diamond P.J., Napier P.J. (eds.) Very Long Baseline Interferometry and the VLBA, Vol. 82. Astronomical Society of the Pacific Conference Series, p. 227

Doeleman S., 2008, Journal of Physics Conference Series 131, 012055

Eckart A., Genzel R., 1996, Nat 383, 415

Falomo R., Maraschi L., Treves A., Tanzi E.G., 1987, ApJL 318, L39

Fanaroff B.L., Riley J.M., 1974, MNRAS 167, 31P

Fomalont E., 1981, National Radio Astronomy Observatory Newsletter 3, 3

Frater R.H., Brooks J.W., Whiteoak J.B., 1992, Journal of Electrical and Electronics Engineering Australia 12, 103

Gliozzi M., Foschini L., Sambruna R.M., Tavecchio F., 2008 478, 723

Govoni F., Falomo R., Fasano G., Scarpa R., 2000 143, 369

Greisen E.W., 1998, In: Albrecht R., Hook R.N., Bushouse H.A. (eds.) Astronomical Data Analysis Software and Systems VII, Vol. 145. Astronomical Society of the Pacific Conference Series, p. 204

Hada K., Doi A., Kino M., et al., 2011, Nat 477, 185

Hartman R.C., Bertsch D.L., Bloom S.D., et al., 1999, ApJS 123, 79

Hartman R.C., Bertsch D.L., Fichtel C.E., et al., 1992, In: Shrader C.R., Gehrels N., Dennis B. (eds.) NASA Conference Publication, Vol. 3137. NASA Conference Publication, p.116

Hauser M., Behera B., Hagen H., Wagner S., 2009, The Astronomer's Telegram 2158, 1

Heckman T.M., 1980, A&A 87, 152

H.E.S.S. Collaboration 2010 511, A52

Hewitt A., Burbidge G., 1989, ApJS 69, 1

Hirabayashi H., Hirosawa H., Kobayashi H., et al., 2000, PASJ 52, 955

Hoffmeister C., 1929, Astronomische Nachrichten 236, 233

Högbom J.A., 1974 15, 417

Jansen F., Lumb D., Altieri B., et al., 2001 365, L1

Jauncey D.L., Batty M.J., Wright A.E., et al., 1984, ApJ 286, 498

Jauncey D.L., Reynolds J.E., Tzioumis A.K., et al., 1994, In: Robertson J.G., Tango W.J. (eds.) Very High Angular Resolution Imaging, Vol. 158. IAU Symposium, p.131

Jones D.H., Read M.A., Saunders W., et al., 2009, MNRAS 399, 683

Kadler M., Ros E., Lobanov A.P., et al., 2004 426, 481

Kellermann K.I., Lister M.L., Homan D.C., et al., 2004, ApJ 609, 539

Kellermann K.I., Pauliny-Toth I.I.K., 1969, ApJL 155, L71

Kellermann K.I., Sramek R., Schmidt M., et al., 1989, AJ 98, 1195

Kellermann K.I., Vermeulen R.C., Zensus J.A., Cohen M.H., 1998, AJ 115, 1295

Khachikyan É.Y., Weedman D.W., 1971, Astrophysics 7, 231

Komossa S., Voges W., Xu D., et al., 2006, AJ 132, 531

Kovalev Y.Y., Kellermann K.I., Lister M.L., et al., 2005, AJ 130, 2473

Kovalev Y.Y., Lobanov A.P., Pushkarev A.B., Zensus J.A., 2008 483, 759

Krauss F., 2013, Master thesis, Friedrich-Alexander-Universität Erlangen-Nürnberg

Krolik J.H., 1999, Active galactic nuclei : from the central black hole to the galactic environment, Princeton University Press

Lawrence A., 1987, PASP 99, 309

Levenberg K., 1944, Quarterly of Applied Mathematics 2 164

Lin Y.C., Bertsch D.L., Bloom S.D., et al., 1999, ApJ 525, 191

Lister M.L., Aller H.D., Aller M.F., et al., 2009a, AJ 137, 3718

Lister M.L., Aller M., Aller H., et al., 2011, ApJ 742, 27

Lister M.L., Homan D.C., 2005, AJ 130, 1389

Lister M.L., Homan D.C., Kadler M., et al., 2009b, ApJL 696, L22

Lobanov A.P., 1998 330, 79

Lobanov A.P., Zensus J.A., 1999, ApJ 521, 509

Longair M.S., 2011, High Energy Astrophysics, Cambridge University Press

Marscher A.P., 2009, ArXiv e-prints 0909.2576

Marshall H.L., Schwartz D.A., Lovell J.E.J., et al., 2005, ApJS 156, 13

McCulloch P.M., Ellingsen S.P., Jauncey D.L., et al., 2005, AJ 129, 2034

Miller J.S., 1994, In: Bicknell G.V., Dopita M.A., Quinn P.J. (eds.) The Physics of Active Galaxies, Vol. 54. Astron. Soc. Pacific, Conf. Ser., p. 149

Mueller C., 2011, Diplomarbeit, Friedrich-Alexander-Universität Erlangen-Nürnberg

Mueller C., Kadler M., Ojha R., et al., 2011 530, L11

Ojha R., Fey A.L., Charlot P., et al., 2005, AJ 130, 2529

Ojha R., Fey A.L., Johnston K.J., et al., 2004, AJ 127, 3609

Ojha R., Kadler M., Böck M., et al., 2010 519, A45

Osterbrock D.E., Mathews W.G., 1986, ARA&A 24, 171

Paragi Z., Reynolds C., Biggs A.D., et al., 2005, In: Romney J., Reid M. (eds.) Future Directions in High Resolution Astronomy, Vol. 340. Astronomical Society of the Pacific Conference Series, p. 611

Peacock J.A., Miller L., Longair M.S., 1986, MNRAS 218, 265

Pearson T.J., 1995, In: Zensus J.A., Diamond P.J., Napier P.J. (eds.) Very Long Baseline Interferometry and the VLBA, Vol. 82. Astronomical Society of the Pacific Conference Series, p. 268

Pearson T.J., Readhead A.C.S., 1981, ApJ 248, 61

Peterson B.A., Jauncey D.L., Condon J.J., Wright A.E., 1976, ApJL 207, L5

Peterson B.M., 1997, An Introduction to Active Galactic Nuclei

Polatidis A.G., Wilkinson P.N., Xu W., et al., 1995, ApJS 98, 1

Preston R.A., Jauncey D.L., Meier D.L., et al., 1989, AJ 98, 1

Quintana H., Ramirez A., 1995, ApJS 96, 343

Readhead A.C.S., 1994, ApJ 426, 51

Ros E., Lobanov A.P., 2001, In: Behrend D., Rius A. (eds.) 15th Workshop Meeting on European VLBI for Geodesy and Astrometry., p. 208

Rybicki G.B., Lightman A.P., 1979, Radiative processes in astrophysics, New York, Wiley-Interscience

Sambruna R.M., Urry C.M., Ghisellini G., Maraschi L., 1995, ApJ 449, 567

Schneider P., 2008, Einführung in die extragalaktische Astronomie und Kosmologie, Springer Berlin

Schwab F.R., Cotton W.D., 1983, AJ 88, 688

Scott W.K., Fomalont E.B., Horiuchi S., et al., 2004, ApJS 155, 33

Seyfert C.K., 1943, ApJ 97, 28

Shakura N.I., Sunyaev R.A., 1973 24, 337

Shen Z.Q., Wan T.S., Moran J.M., et al., 1997, AJ 114, 1999

Shen Z.Q., Wan T.S., Moran J.M., et al., 1998, AJ 115, 1357

Shepherd M.C., 1997, In: Hunt G., Payne H. (eds.) Astronomical Data Analysis Software and Systems VI, Vol. 125. Astron. Soc. Pacific, Conf. Ser., p. 77

Shepherd M.C., Pearson T.J., Taylor G.B., 1994, In: BAAS, Vol. 26. BAAS, p.987

Stickel M., Meisenheimer K., Kuehr H., 1994 105, 211

Sulentic J.W., Marziani P., Dultzin-Hacyan D., 2000, ARA&A 38, 521

Tagliaferri G., Ghisellini G., Giommi P., et al., 2001 368, 38

Taylor G.B., Carilli C.L., Perley R.A., (eds.) 1999, Synthesis Imaging in Radio Astronomy II, Vol. 180 of *Astron. Soc. Pacific, Conf. Ser.*, Astron. Soc. Pacific, Conf. Ser.

Taylor G.B., Fassnacht C.D., Sjouwerman L.O., et al., 2005, ApJS 159, 27

Taylor G.B., Vermeulen R.C., Pearson T.J., et al., 1994, ApJS 95, 345

Taylor G.B., Vermeulen R.C., Readhead A.C.S., et al., 1996, ApJS 107, 37

Thompson A.R., Moran J.M., Swenson, Jr. G.W., 2001, Interferometry and Synthesis in Radio Astronomy, 2nd Edition, New York : Wiley

Tingay S., Macquart J.P., Lovell J., et al., 2009, ATNF Proposal 1995

Tingay S.J., Jauncey D.L., King E.A., et al., 2003, PASJ 55, 351

Tingay S.J., Reynolds J.E., Tzioumis A.K., et al., 2002, ApJS 141, 311

Trussoni E., Vagnetti F., Massaglia S., et al., 1999 348, 437

Urry C.M., Padovani P., 1995, PASP 107, 803

Venturi T., Morganti R., Tzioumis T., Reynolds J., 2000 363, 84

Véron-Cetty M.P., Véron P., 2006, A&A 455, 773

Wall J.V., Pettini M., Danziger I.J., et al., 1986, MNRAS 219, 23P

Weisskopf M.C., Brinkman B., Canizares C., et al., 2002, PASP 114, 1

Wells D.C., Greisen E.W., Harten R.H., 1981 44, 363

Williams R.E., Blacker B., Dickinson M., et al., 1996, AJ 112, 1335

Wills K.A., Morganti R., Tadhunter C.N., et al., 2004, MNRAS 347, 771

Danksagung

An dieser Stelle möchte ich mich bei allen bedanken, die dazu beigetragen haben, dass diese Arbeit in dieser Form zustande gekommen ist.
Als erstes möchte ich mich bei Prof. Dr. Matthias Kadler bedanken, der mir die Möglichkeit gegeben hat, dieses Projekt zu bearbeiten und mich dabei betreut hat. Seine Vorlesung zu extragalaktischen Jets hat mein Interesse für die Radioastronomie und für aktive Galaxienkerne und deren Jets geweckt. Mithilfe der Arbeit in seiner Arbeitsgruppe konnte ich mein Wissen zu diesem Thema vertiefen und an aktuellen Projekten mitarbeiten.
Zudem bedanke ich mich bei allen Mitglieder des TANAMI Projekt, insbesondere bei Dr. Roopesh Ojha, der zusammen mit Prof. Dr. Matthias Kadler das Projekt leitet, für die vielen hilfreichen Tipps und Hinweisen.
Für die Einarbeitung und Hilfe mit den entsprechenden Programmen und ihren Funktionsweisen möchte ich besonders bei Cornelia Müller und Robert Schulz bedanken. Außerdem bei Christoph Großberger für die Bereitstellung und Hilfe mit seinen ISIS-Skripten.
Bei Prof. Dr. Friedrich Röpke bedanke ich mich, dass er sich bereit erklärt hat, diese Arbeit als Zweitgutachter zu bewerten.
Für viele Diskussionen und die gute Arbeitsatmosphäre bedanke ich mich außerdem besonders bei meinem Zimmerkollegen Marcus Langejahn und bei Annika Kreikenbohm, Katharina Leiter und Till Steinbring sowie allen anderen Mitarbeitern des Lehrstuhls für Astronomie unter der Leitung von Prof. Dr. Karl Mannheim.

Außerdem bedanke ich mich bei meinen Eltern und meiner Freundin Melanie Fritz für die Unterstützung während meines Studiums.